

ABSTRACT

LEDFORD, JOHN CHRISTOPHER. Development of Processing Techniques for the Fabrication of Pure Copper Components Utilizing EB-PBF. (Under the direction of Dr. Timothy Horn and Dr. Russell King).

Additive manufacturing of pure copper has gained traction recently with the possibility of utilizing the numerous benefits including geometrical complexity. However, issues with high oxygen content and rough surfaces deter its application to the production of specialized components such as radio frequency devices. Stringent material properties are required for these devices to operate at peak performance under high power. In this work, we developed techniques to produce pure copper with a low oxygen content that would start to meet the requirements of these demanding applications. Finer powder size distributions were utilized to reduce the surface roughness of fabricated components. This resulted in roughly a 75% decrease in the as fabricated surface roughness with any post processing. A hydrogen heat treatment was implemented on the precursor copper powder to remove increased oxygen content which would allow for the fabrication of pure copper components. An oxygen content reduction of almost 90% was achieved in the final fabricated parts with only 50 ppm wt. of oxygen remaining. Initial studies of implementing a similar hydrogen heat treatment on a layer by layer basis during fabrication is also presented. Lastly, the use of electron emissions for in-situ monitoring during the EB-PBF fabrication process is investigated to aid in the production of high quality, low quantity components.

© Copyright 2021 by John Christopher Ledford

All Rights Reserved

Development of Processing Techniques for the Fabrication of Pure Copper Components
Utilizing EB-PBF

by
John Christopher Ledford

A dissertation submitted to the Graduate Faculty of
North Carolina State University
in partial fulfillment of the
requirements for the degree of
Doctor of Philosophy

Industrial Engineering

Raleigh, North Carolina
2021

APPROVED BY:

Dr. Timothy Horn
Committee Co-Chair

Dr. Russell King
Committee Co-Chair

Dr. Harvey West II

Dr. Paul Cohen

Dr. Claude Reynolds Jr.

Dr. Diana Gamzina
External Member

DEDICATION

I dedicate this work to my wife, Rachel, and my daughters, Averie and Zoey.

BIOGRAPHY

Born in Lincolnton, NC, Christopher attended Lincolnton High School and went on to attend North Carolina State University for his bachelors in Materials Science and Engineering. After graduation, he continued at North Carolina State University studying for a thesis masters in Materials Science and Engineering working on iron-based superconductors using powder metallurgy. After taking a course on additive manufacturing, he proceeded to start his studies in the Industrial Systems and Engineering department at North Carolina State University for his Ph.D. on metal additive manufacturing.

ACKNOWLEDGMENTS

This has been a long journey with many people to thank along the way.

I would like to start by thanking my advisors, Dr. Tim Horn and Dr. Russell King, for their guidance and help with not only my work and thesis but life in general. Dr. Harvey West and Dr. Chris Rock for their many intellectual conversations and those just to pass the time. Chet Wyrick for his immense help through the years and the opportunities to learn a few tricks of the trade.

To my CAMAL lab mates, the journey has been filled with late nights and more builds than I could possibly start to count. It has been a true pleasure to work you with guys and gals. A special thanks to Mouda who came with an eager mind and willing to work with this crazy guy.

To Roger, Karen, Toby, and Natalie; my friends who have stuck by through what seems to be a lifelong journey to the doctorate. Always there to lend a helping hand.

To my family and friends who stuck by me as I spent the many years confusing you on what exactly it was I actually worked on. A special thanks to Mom and Dad who helped me my whole life and always pushed me to go further.

To my wife, Rachel, who has helped me over these past few years in realizing this dream. Through our first child, Averie, to our next due in a few months, there is nothing we cannot do if we set my stubborn mind to it.

TABLE OF CONTENTS

LIST OF TABLES.....	vii
LIST OF FIGURES	viii
Chapter 1: Introduction	1
Chapter 2: Surface Roughness Reduction using Electron Beam Melting Additive	
Manufacturing of Pure Copper Powder	8
2.1 Introduction.....	8
2.2 Methodology	9
2.2.1 Powder Characteristics.....	9
2.2.2 Sample Fabrication	9
2.3 Results.....	11
2.3.1 Powder	11
2.3.2 Solid	13
2.4 Discussion	19
2.5 Conclusions.....	20
2.6 References.....	21
Chapter 3: Characteristics and Processing of Hydrogen-Treated Copper Powders for EB-PBF Additive Manufacturing	22
3.1 Introduction.....	23
3.2 Materials and Methods.....	27
3.2.1 Feedstock Preparation.....	28
3.2.2 Feedstock Characterization.....	29
3.2.3 In-Situ Heated Stage	30
3.2.4 Customized EB-PBF Platform.....	31
3.2.5 Simulation and Validation of Variable Spacing Single Melt Track Width Wafers.....	32
3.2.6 EB-PBF Processing of Hydrogen-Treated Copper Powder.....	34
3.2.7 High Speed Footage of Melt Pool.....	37
3.2.8 Solid Sample Fabrication	37
3.3 Results.....	38
3.3.1 Powder Characterization	38
3.3.2 Electron Beam Fabrication	47
3.4 Discussion	57
3.5 Conclusions.....	62
3.6 References	63
Chapter 4: Real Time Monitoring of Electron Emissions during Electron Beam Powder Bed Fusion for Arbitrary Geometries and Toolpaths	69
4.1 Introduction.....	70
4.2 Methodology	75
4.2.1 Instrumentation and Data Acquisition	75
4.2.2 Multiple Sensor Detector Hardware	76
4.2.3 Integration of the detector with the EB-PBF platform.....	78

4.2.4 Image Generation.....	81
4.2.5 EB-PBF Sample Fabrication.....	82
4.2.6 Comparison of TEY melt imaging to μ CT	84
4.2.7 Observing beam speed and TEY for Arbitrary Geometries.....	87
4.2.8 Mapping overhanging surfaces and complex geometries	89
4.2.9 Implementation of a Rudimentary Control Strategy Based on TEY	91
4.3 Results.....	92
4.3.1 TEY melt imaging to μ CT Comparison	93
4.3.2 Spatiotemporal Process Maps	102
4.3.3 Beam Speed Mapping	103
4.3.4 Thickness Function Mapping.....	106
4.3.5 Process Parameter Mapping.....	109
4.3.6 PLC Data mapping and TEY Correlation.....	111
4.3.7 Control Experiment Results.....	115
4.4 Discussion and Conclusions	116
4.4.1 Material Considerations	117
4.4.2 Interpretation of TEY Data	120
4.4.3 Significance and Interpretation of Spatiotemporal Process Maps	124
4.4.4 Proof of Concept for EB-PBF Process Control	127
4.4.5 Other Observed Limitations of the Methodology and Alternative Solutions	128
4.5 Summary and Conclusions	131
4.6 References.....	134
Chapter 5: Future Work: Layer by Layer Hydrogen Treatment of Copper Powder during EB-PBF Additive Manufacturing.....	145
5.1 Introduction.....	145
5.2 Methodology	146
5.3 Results and Discussion	147
5.4 Conclusions.....	150
5.5 References	151
Chapter 6: Conclusions	152
Appendix.....	153

LIST OF TABLES

Chapter 2

Table 1	Representative density, relative density, oxygen, and hydrogen content for coarse and mid-fraction copper powders.....	12
Table 2	Representative density, relative density, oxygen, and hydrogen content for coarse and mid-fraction solids.....	15
Table 3	Surface roughness parameters of as-fabricated XZ (side) surfaces of coarse and mid-fraction solids.....	18

Chapter 3

Table 1	Chemical content of copper powders	38
---------	--	----

LIST OF FIGURES

Chapter 2

Figure 1	Volumetric particle size distribution of coarse and mid-fraction copper powders ..	11
Figure 2	Representative scanning electron micrographs of the coarse (left) and mid-fraction (right) copper powders	12
Figure 3	Representative image of the build	13
Figure 4	Optical micrographs of solid XZ etched cross-sections fabricated using coarse (A) and mid-fraction (B) copper powders	14
Figure 5	Representative scanning electron micrographs of solid XZ cross-sections fabricated using coarse (A) and mid-fraction (B) copper powders	14
Figure 6	Representative optical images of as-fabricated XZ (side) surfaces of coarse (A) and mid-fraction (B) solids.....	16
Figure 7	Representative scanning electron micrographs of as-fabricated XZ (side) surfaces of coarse (A) and mid-fraction (B) solids	16
Figure 8	Representative height maps representing surface height of as-fabricated XZ (side) surfaces of coarse (A) and mid-fraction (B) solids	17
Figure 9	Bar plot of surface roughness parameters for coarse and mid-fraction XZ (side) surfaces	19

Chapter 3

Figure 1	Hydrogen brazing furnace at SLAC National Accelerator Laboratory Technology Innovation Directorate (TID) (left), and stacked-stainless steel fixture (right) for treating multiple trays of copper powder in 2-mm thick layers... ..	29
Figure 2	Photographs of the customized Arcam A2 electron beam melting system, showing the interior of the vacuum chamber, mechanical components and in-situ backscatter electron (BSE) detector (A), and the exterior of the vacuum chamber, showing the electron beam column and the location of instrumentation and viewports (B). The line of sight of the visible light camera, pyrometer, and IR camera are illustrated by the dashed lines in 2A, from viewports 1, 2, and 3, respectively.....	32

Figure 3	Illustration of the single melt track width geometry with 2.0 mm spacing. Powder was harvested from between the wafers in a serial fashion, as a function of the distance from the solid copper wall	33
Figure 4	Illustration of the in-situ H ₂ O vapor out-gassing experiment. The electron beam melting (EBM) vacuum chamber is outfitted with a residual gas analysis (RGA) and IR camera, and the surface temperature is monitored by a two-color pyrometer and thermocouple (A). The base fixture contains six 3 mm deep pockets (B), which are filled with hydrogen-treated and untreated powders with varying initial oxygen content. A single layer disc is melted on the top surface of each powder type. During melting, H ₂ O is released from the powder or melt pool, and detected by the RGA (C). Upon completion, the powder is manually removed from the solid disc of copper, which is analyzed for oxygen and hydrogen content by inert gas fusion (D)	35
Figure 5	Plot showing at. % oxygen versus at. % hydrogen for all of the hydrogen heat-treated copper powders used in this study	39
Figure 6	Plot showing the skeletal density of the untreated and hydrogen heat-treated copper powders of varying initial oxygen content, as measured by nitrogen pycnometry	40
Figure 7	Representative low and high magnification scanning electron micrographs of untreated and hydrogen-treated MO-Cu powder. (A) Low magnification and (C) high magnification of untreated hydrogen-treated MO-Cu powder; (B) Low magnification and (D) high magnification of hydrogen-treated MO-Cu powder	41
Figure 8	Representative high magnification ion channeling contrast micrographs of pretreated LO-Cu (A), MO-Cu (B), HO-Cu (C), and post hydrogen treatment LO-Cu (D), MO-Cu (E), and HO-Cu (F) focused ion beam (FIB) sectioned Cu powder particles showing the presence of grain boundary Cu ₂ O in the untreated condition (A–C), which reacts with hydrogen to form H ₂ O pores (E,F). LO-Cu powder lacks significant grain boundary oxides, and therefore does not exhibit H ₂ O vapor induced porosity. Note that scale bars vary in the images	43
Figure 9	HAADF STEM micrograph and energy dispersive spectroscopy (EDS) of hydrogen-treated MO-Cu powder grain boundary triple point showing submicron scale H ₂ O vapor induced porosity	44
Figure 10	Thermogravimetric analysis of untreated and hydrogen-treated LO-Cu, MO-Cu, and HO-Cu powder under flowing nitrogen.....	45
Figure 11	Scanning electron micrographs of a HO-Cu particle after hydrogen treatment, before (A) and after (B–D) in-situ SEM heating on a SiC chip to 400 °C at 100 °C/s under a vacuum.....	47

Figure 12	Contour plot of the temperature profile in the XZ plane during melting, with a 2000 μm hatch spacing, showing SEM images of particles located at the edge/wall (A), ~0.1 mm (B), and ~0.3–0.5 mm (C) from the wafer	50
Figure 13	Photograph showing the oxygen free electronic (OFE) copper fixture after EB-PBF of single layer discs on top of hydrogen-treated powder cakes (A). Optical microscope images of the surface of single layer disc produced with hydrogen-treated HO-Cu showing pitting and porosity (B), and surface of single layer disc produced with hydrogen-treated LO-Cu, showing a smooth surface texture (C). Tabulated oxygen and hydrogen contents of the precursor powders and the solid single layer discs for each treated powder condition (D).....	52
Figure 14	Residual gas analysis of HO-Cu, MO-Cu, and LO-Cu powder during the electron beam powder bed fusion (EB-PBF) of single layer discs.....	53
Figure 15	Representative frames of high-speed video footage showing the EB-PBF of a single layer disc on hydrogen-treated LO-Cu powder at timestamps -172.333 ms (A), -170.200 ms (B), -167.687 ms (C).....	54
Figure 16	Representative frames of high-speed video footage showing the EB-PBF of a single layer disc on hydrogen-treated HO-Cu powder at timestamps 195.433 ms (A), 197.700 ms (B), 198.733 ms (C)	55
Figure 17	Oxygen and hydrogen content of precursor powders and solid copper cylinders produced with the EB-PBF of untreated and hydrogen-treated MO-Cu powder, and (inset) in-situ residual gas analysis of both EB-PBF runs, showing the layerwise outgassing of H ₂ O	56
Figure 18	Optical micrographs showing polished and etched microstructures of copper samples fabricated with EB-PBF using hydrogen heat-treated MO-Cu powder (A) and untreated MO-Cu powder (B). The build direction for both samples are indicated by the arrow in B	57
Figure 19	Wt. ppm oxygen as a function of the particle size, assuming a 5 nm cuprous oxide film	58

Chapter 4

Figure 1	Illustration of the detector hardware mounted inside the EB-PBF vacuum chamber (A) and schematic of the hardware assembly circuit diagram showing the arrangement of the components (B). The current to voltage converter (converter circuits) are outlined in green. The differential circuits are outlined in blue, and the summing circuits are outlined in red	78
Figure 2	Plot of HV beam current feedback signal versus the user-defined beam current	79

Figure 3	Schematic of the system integration. The data acquisition loop (bottom) shows the hardware used to acquire TEE, X, and Y deflection feedback, grid feedback, and HV beam current feedback. The control loop (top) illustrates the conversion of TEY data into a feedback signal used to modify the demanded beam current....	81
Figure 4	Plot of user-defined beam speed and calculated beam speed. Error bars indicate the standard deviation of measured speeds	88
Figure 5	Illustration of the overhang geometry (A) and illustration of the CCTWT device (B). The illustration is sectioned in the XZ plane to highlight the internal downward-facing features. Note: images are not to scale.....	91
Figure 6	μ CT (A) scan and TEY signal image (B) of the top layer of a sample built with 12mA and SF 40. A plot of μ CT & TEY MAPE (%) comparison results for 48 equidistant profile lines (C), A plot showing the normalized line intensities for μ CT and TEY data, with MAPE results, shown in the X-direction for Y=7 & 8 mm lines,(D & E) respectively.....	95
Figure 7	A) TEY, μ CT and SSIM index maps for four build conditions from 8-16 mA & 30-40 SF and a closeup of an SSIM index map for B) 8 mA, SF30 (blue box) and C) 12 mA, SF40 (red box) where the arrows in each figure point to features of interest	97
Figure 8	SSIM data for 8 mA, 12 mA, and 16 mA samples for all layers melted up to the 10 mm build Z height (mm). Individual SSIM map images are from 12 mA, SF 40 (green) and 12 mA, SF30 (blue) conditions at 2, 4, 6, and 8 mm build or z heights, respectively	99
Figure 9	TEY, μ CT and Optical microscopy Y-Z plane cross-section images for selected samples. Build direction is vertical and parallel with the Z axis.....	101
Figure 10	Stacked 3D maps of 10 mm x 10 mm x 10 mm cubes with solid background intensity removed to demonstrate porosity A) μ CT scans: 12 mA, SF 40 B) TEY: 12 mA, SF 40 C) μ CT scans: 16 mA, SF 30 D) TEY: 16 mA, SF 30	102
Figure 11	TEY (top row), beam speed (middle row), and volumetric energy density (bottom row) maps for the pure copper samples fabricated with parameters listed above each column and sampled at the height of Z height of 5 mm	104

Figure 12 Beam speed map section in the center of the XZ plane for the overhang experiment showing the change in beam speed in the overhang region (A). A plot of the same data extracted from a line profile in the center of each sample oriental along the Z axis (B). TEY images at 1mm below (left), and 1 mm and 3 mm above the downward-facing surface for a thickness factor of 1.0 and speed factor of 10 mm (C) and 30 mm (D). Tiled optical microscope images of the cross-section at each corresponding height and condition, respectively.....	108
Figure 13 Process space maps for EB-PBF of pure copper, including this study (A). The average beam current and velocity for each layer from the 12 prismatic samples (B). The relative position of the beam within samples. The volumetric energy density space, which includes TEY data (D)	111
Figure 14 3D data maps for CCTWT device fabricated from pure copper A) TEY data B) beam speed C) electron gun filament current feedback D) column pressure E) bottom thermocouple temperature F) beam position as a function of build time ..	113
Figure 15 Shows beam position as a function of time for the first layer of a copper build. The melt order and hatch direction are evident in (A). At shorter time scales, the hatch melt order is further resolved (B) for one of the samples. Imaging with complex tool paths that involve beam multiplexing (spot melting), as is commonly done for part contours and arbitrary part geometries is possible (C) ...	114
Figure 16 Control experiment showing TEY and optical cross-section of experimental result (A) and average layer TEY intensity and control beam current vs. build height (B).....	116
Figure 17 3D x-ray μ CT (A) and TEY (B) reconstructions of a 10 mm x 10 mm x 10 mm copper cube. In this example, the x-ray μ CT could not penetrate the sample, but the TEY is able to resolve the internal features	119
Figure 18 Top surface layer high-speed images recorded at A) t=0, t=13 sec, t=21 sec, and TEY signal generated during high-speed imaging from 0-21 sec and B) Illustration of the EB interaction with powder bed and melt pool.....	123
Figure 19 Grid voltage feedback signal (left) and HV current feedback signal feedback signal (right) for multiple layers of samples produced in this study at 8 mA, 12 mA, and 16 mA beam currents.....	129
Figure 20 Photograph of the pure copper build, which experienced a beam shift induced by an external magnetic field (A), and TEY data map showing the loss of signal associated with the beam shift in the same nominal layer location (B)	130

Chapter 5

Figure 1	2 Θ as a function of time of the Cu ₂ O (111) peak at a holding temperature of 600°C in a reducing atmosphere	147
Figure 2	XRD of the precursor Cu ₂ O powder (bottom) and the resulting pure copper powder (top) after the hydrogen heat treatment	148
Figure 3	Stainless steel perforated ring used to introduce gas into the EB-PBF system.....	149

CHAPTER 1: Introduction

Additive manufacturing of copper and copper-based alloys offers unique opportunities for applications such as heat exchangers and radio frequency (RF) devices where more complex geometries give way to better performance and longer lifetimes. These applications require excellent electrical and thermal conductivities while maintaining its structural integrity at elevated temperatures.

Research into the additive manufacturing of copper and copper alloys has predominantly been focused to the powder bed fusion systems, electron beam [1]–[8] and laser [9]–[23], but has also seen use in direct energy deposition (DED), ultrasonic [24], [25], direct write [26], [27], and binder jetting [28], [29]. Electron beam melting (EBM) has been utilized in several instances in the literature to produce copper components to leverage the advantages of the EBM system over that of commercial laser powder bed fusion (L-PBF) systems [1]–[8]. These advantages include high absorptivity of the electron beam, high vacuum processing environment, elevated build temperatures, and high beam speeds. L-PBF of pure copper is a relatively tricky process due to the low absorptivity of the powder at wavelengths (~1064 nm) typically found in commercial L-PBF systems.

Oxygen free electrical (OFE) or C10100 copper is of particular interest due to its widespread use in VED. OFE copper has strict purity requirements to ensure high electrical conductivity including an oxygen content of no more than 5 parts per million [30]. Increased oxygen content can also lead to issues with brazing procedures, specifically hydrogen brazing, where the hydrogen reacts with the oxygen and creates pores or blistering known as hydrogen embrittlement [31]–[33]. This type of defect can lead to structural integrity issues.

A subset of those RF devices are called vacuum electronic devices (VED) which include such things as traveling-wave tubes and klystrons. These devices use an electron gun and geometrically complex structures in an ultrahigh vacuum environment to produce electromagnetic radiation. Applications for such devices include RADAR and defense, communications, plasma generation, and particle accelerators. These applications have stringent requirements in terms of geometrical accuracy, material purity, and surface finish. Typically, these devices are made from numerous individual machined components (~10-100's) which are then welded or brazed to create a complex structure. With every individual component and braze/weld step, comes the possibility of a failure which could leave the entire assembly as scrap or needing rework which can significantly increase costs. The appeal of additively manufacturing these devices is the possibility of reducing or eliminating the need for the production of multiple components and brazing/welding steps. It also brings the ability for more intricate and complex design structures which could lead to increased part performance and/or lifetime.

In this thesis, we start to look at overcoming some of the current drawbacks to additively manufacturing copper based RF devices such as surface roughness and material purity. Chapter two explores the use of pure copper powder with a finer powder size distribution to reduce the as fabricated surface roughness in the electron beam powder bed fusion process. Chapter three explores a hydrogen heat treatment process of the precursor copper powder which is intended to remove excess oxygen from the material. We also start to look at the ability to use electron emissions from the EB-PBF process as a possible part qualification method due to the low volume of parts actually produced. Chapter four explores the use of in-situ electron emissions during the melting process to characterize the melt surface of the samples. Total electron

emissions with respect to the beam position were correlated to metallography and micro computed tomography (μ CT) to look for defects which may be visible on a layer by layer basis. Chapter five explores the prospect of an in-situ hydrogen treatment of the precursor copper powder on a layer by layer basis which would allow the use for higher oxygen content powder while still fabricating low oxygen content parts. High temperature X-ray diffraction was performed in a hydrogen argon atmosphere to determine how quickly Cu_2O could be reduced at elevated temperatures similar to that of the EB-PBF process.

References

- [1] P. Frigola et al., “Fabricating Copper Components,” *Adv. Mater. Process.*, pp. 20–20, 2014.
- [2] R. Guschlbauer, S. Momeni, F. Osmanlic, and C. Körner, “Process development of 99.95% pure copper processed via selective electron beam melting and its mechanical and physical properties,” *Mater. Charact.*, Apr. 2018.
- [3] M. A. Lodes, R. Guschlbauer, and C. Körner, “Process development for the manufacturing of 99.94% pure copper via selective electron beam melting,” *Mater. Lett.*, vol. 143, pp. 298–301, Mar. 2015.
- [4] S. J. Raab, R. Guschlbauer, M. A. Lodes, and C. Körner, “Thermal and Electrical Conductivity of 99.9% Pure Copper Processed via Selective Electron Beam Melting,” *Adv. Eng. Mater.*, vol. 18, no. 9, pp. 1661–1666, Sep. 2016.
- [5] D. A. Ramirez et al., “Open-cellular copper structures fabricated by additive manufacturing using electron beam melting,” *Mater. Sci. Eng. A*, vol. 528, no. 16–17, pp. 5379–5386, Jun. 2011.
- [6] D. A. Ramirez et al., “Novel precipitate–microstructural architecture developed in the fabrication of solid copper components by additive manufacturing using electron beam melting,” *Acta Mater.*, vol. 59, no. 10, pp. 4088–4099, Jun. 2011.
- [7] X. Shu, G. Chen, J. Liu, B. Zhang, and J. Feng, “Microstructure evolution of copper/steel gradient deposition prepared using electron beam freeform fabrication,” *Mater. Lett.*, Nov. 2017.
- [8] C. A. Terrazas et al., “Multi-material metallic structure fabrication using electron beam melting,” *Int. J. Adv. Manuf. Technol.*, vol. 71, no. 1–4, pp. 33–45, Mar. 2014.

- [9] M. Colopi, L. Caprio, A. G. Demir, and B. Previtali, “Selective laser melting of pure Cu with a 1 kW single mode fiber laser,” *Procedia CIRP*, vol. 74, pp. 59–63, Jan. 2018.
- [10] L. Constantin et al., “Laser sintering of cold-pressed Cu powder without binder use,” *Materialia*, Aug. 2018.
- [11] C. Deng, J. Kang, T. Feng, Y. Feng, X. Wang, and P. Wu, “Study on the Selective Laser Melting of CuSn10 Powder,” *Materials*, vol. 11, no. 4, Apr. 2018.
- [12] T.-T. Ikeshoji, K. Nakamura, M. Yonehara, K. Imai, and H. Kyogoku, “Selective Laser Melting of Pure Copper,” *JOM*, pp. 1–5, Dec. 2017.
- [13] S. D. Jadhav, S. Dadbakhsh, L. Goossens, J.-P. Kruth, J. Van Humbeeck, and K. Vanmeensel, “Influence of selective laser melting process parameters on texture evolution in pure copper,” *J. Mater. Process. Technol.*, vol. 270, pp. 47–58, Aug. 2019.
- [14] L. Kaden et al., “Selective laser melting of copper using ultrashort laser pulses,” *Appl. Phys. A*, vol. 123, no. 9, Sep. 2017.
- [15] Z. Liu, W. Zhou, Y. Lu, H. Xu, Z. Qin, and X. Lu, “Laser 3D printing of W-Cu composite,” *Mater. Lett.*, vol. 225, pp. 85–88, Aug. 2018.
- [16] P. Lykov, E. V. Safonov, and A. Akhmedianov, “Selective Laser Melting of Copper,” *Mater. Sci. Forum*, vol. 843, pp. 284–288, Feb. 2016.
- [17] Z. Mao, D. Z. Zhang, J. Jiang, G. Fu, and P. Zhang, “Processing optimisation, mechanical properties and microstructural evolution during selective laser melting of Cu-15Sn high-tin bronze,” *Mater. Sci. Eng. A*, Feb. 2018.
- [18] A. Popovich, V. Sufiarov, I. Polozov, E. Borisov, D. Masaylo, and A. Orlov, “Microstructure and mechanical properties of additive manufactured copper alloy,” *Mater. Lett.*, vol. 179, pp. 38–41, Sep. 2016.

- [19] A. A. Saprykin, N. A. Saprykina, and A. A. Saprykin, “Analysis and prediction of copper surface roughness obtained by selective laser melting,” IOP Conf. Ser. Mater. Sci. Eng., vol. 441, p. 012044, Nov. 2018.
- [20] S. Scudino et al., “Additive manufacturing of Cu–10Sn bronze,” Mater. Lett., vol. 156, pp. 202–204, Oct. 2015.
- [21] C. F. Y. Tey Wai Yee; Chen, Songlin, “Selective Laser Melting Of Copper Based Alloy On Steel A Preliminary Study.”
- [22] A. P. Ventura, “Microstructural Evolution and Mechanical Property Development of Selective Laser Melted Copper Alloys,” 2017.
- [23] H. Z. Zhong, C. G. Li, X. Y. Zhang, and J. F. Gu, “The graded microstructures evolving with thermal cycles in pure copper processed by laser metal deposition,” Mater. Lett., vol. 230, pp. 215–218, Nov. 2018.
- [24] M. R. Sriraman, S. S. Babu, and M. Short, “Bonding characteristics during very high power ultrasonic additive manufacturing of copper,” Scr. Mater., vol. 62, no. 8, pp. 560–563, Apr. 2010.
- [25] M. R. Sriraman, M. Gonser, H. T. Fujii, S. S. Babu, and M. Bloss, “Thermal transients during processing of materials by very high power ultrasonic additive manufacturing,” J. Mater. Process. Technol., vol. 211, no. 10, pp. 1650–1657, Oct. 2011.
- [26] D. Lopez-Espiricueta, E. Fearon, S. Edwardson, and G. Dearden, “Direct Write Processing of Multi-micron Thickness Copper Nano-particle Paste on Flexible Substrates with 532 nm Laser Wavelength,” Phys. Procedia, vol. 83, pp. 194–203, Jan. 2016.

- [27] B. K. Park, D. Kim, S. Jeong, J. Moon, and J. S. Kim, “Direct writing of copper conductive patterns by ink-jet printing,” *Thin Solid Films*, vol. 515, no. 19, pp. 7706–7711, Jul. 2007.
- [28] Y. Bai and C. B. Williams, “An exploration of binder jetting of copper,” *Rapid Prototyp. J.*, vol. 21, no. 2, pp. 177–185, Mar. 2015.
- [29] A. Y. Kumar, “Effects of Hot Isostatic Pressing on Copper Parts Additively Manufactured via Binder Jetting,” Virginia Polytechnic Institute and State University, 2018.
- [30] J. R. Davis, *Copper and Copper Alloys*. ASM International, 2001.
- [31] T. G. Nieh and W. D. Nix, “The formation of water vapor bubbles in copper and their effect on intergranular creep fracture,” *Acta Metall.*, vol. 28, no. 5, pp. 557–566, May 1980.
- [32] H. Ito and K. Hayashi, “Detection of Gases in Closed Pores of Incompletely Densified Copper Sintering,” *Proc. 1993 Powder Metall. World Congr.*, 1993.
- [33] Y.-J. Lin and K.-S. Hwang, “Swelling of Copper Powders during Sintering of Heat Pipes in Hydrogen-Containing Atmospheres,” *Mater. Trans.*, vol. 51, no. 12, pp. 2251–2258, 2010.

CHAPTER 2: Surface Roughness Reduction using Electron Beam Melting Additive

Manufacturing of Pure Copper Powder

2.1 Introduction

Additive manufacturing is a layer by layer process which allows fabrication of elaborate structures that would otherwise be unachievable via traditional manufacturing processes. It opens the possibility for unique processing routes of conventional and new material systems to fully realize their potential in various applications. Additive manufacturing does however have its own set of drawbacks, one of particular interest is the surface roughness of as-fabricated parts [1]. Due to the layer by layer nature of the process, the layer thickness plays a crucial role in the surface roughness of as-fabricated parts in a powder bed system [1], [2]. Strano et al. [3] found that layer thickness can be directly correlated to the as-fabricated surface roughness of inclined surfaces in a laser powder bed system. Algardh et al. [4] observed that by reducing the layer thickness by 50% using the same powder size distribution (PSD), the surface roughness could be improved by 33% in Ti-6Al-4V fabrication using electron beam powder bed fusion (EB-PBF). Minimum layer thickness does however depend on the PSD being utilized for fabrication as the minimum layer thickness must be at least as large as the smallest diameter of the PSD. By reducing the PSD utilized for fabrication, smaller layer thicknesses can be used to help improve surface roughness.

In this chapter we study the effect of two powder size distributions on the surface roughness of as-fabricated samples of pure copper processed by EB-PBF. Powder samples were characterized for differences in chemistry, density, and morphology between the PSD's. Fabricated samples were characterized for differences in chemistry, density, microstructure, and surface roughness between the PSD's.

2.2 Methodology

2.2.1 Powder Characteristics

Two distributions of nitrogen atomized copper powder were used in this study. These distributions consisted of a coarse (106-53 um) and mid-fraction (53-15 um) powder size distribution. PSD's were characterized using laser diffraction with a Microtrac S3500 particle size analyzer. Morphology of the particles was observed using scanning electron micrographs from a JEOL JSM-6010A scanning electron microscope (SEM). Representative micrographs were taken from each PSD at 150x magnification at 20 kilovolts.

A powder thief was used to take samples of each powder distribution to ensure a representative sample of the batch was used for powder characterization. Samples were taken in an inert argon atmosphere glovebox to ensure no atmospheric contamination of the powder surface. All powder samples were kept in argon filled sample containers to prevent any atmospheric contamination during characterization. Oxygen and hydrogen content of the powder was measured using inert gas fusion analysis (LECO OHN836 - Form 203-821-455). Powder sample weight was roughly 1 gram per measurement. Powder density was characterized by nitrogen pycnometry using a micro-Ultrapyc 1200e with a non-elutriating measurement cell. This cell allows for the measurement of fine powders without disturbing the sample.

2.2.2 Sample Fabrication

Samples were fabricated using a modified EB-PBF Arcam S12 which utilizes a miniature build tank. Sample geometry consisted of cubes with side length and height of 15 mm. Each sample was located at the center of the oxygen free electrical copper build plate which is 90 mm in diameter. Samples were fabricated without the use of the controlled vacuum system which

typically introduces small amounts of a preferred gas species. This was done to prevent any further possibility of oxidation to the powder feedstock.

Layer thickness used for each powder size distribution was chosen depending on the smaller diameter of particles present in the distribution. For the coarse and mid-fraction distributions, a 50 μm and 20 μm layer thickness, respectively, were chosen using the PSD obtained from laser diffraction.

Processing steps associated with EB-PBF fabrication include heating the build plate, spreading a layer of powder, preheating the powder bed, and finally melting of the two dimensional slice of the three dimensional CAD model. Build plate heating is achieved by rastering the defocused electron beam at high current and speed across the top surface of the plate to reach an elevated temperature. Once the build plate reaches the desired temperature then a thin layer of powder is spread across the surface of the plate. Preheating of the powder layer is achieved by rastering the defocused electron beam across the layer to achieve a light sinter between the particles. The EB-PBF scan strategy utilized a hatch melting step. During the hatch step, the electron beam is rastered in a snake-like pattern to melt the defined part area where the weld pools are offset from each other by a given line offset to achieve optimal overlap. After the entire part geometry for that layer is melted then the plate is lowered by the layer thickness and the process is repeated until the desired three dimensional part geometry is achieved.

Once the samples were removed from the build chamber, any sintered powder left on the samples were removed using a soft bristled brush in order not to disturb the surface roughness of the solid sample. All four side surfaces of each sample were removed at roughly 1 mm thick using a slow speed diamond saw. The remaining solid samples were sectioned along the build direction using a slow speed diamond saw and polished from 320 grit SiC grinding paper to 0.3

μm alumina on micro cloth. Scanning electron micrographs of the polished samples were analyzed for porosity. Solid samples were etched for grain contrast using a solution of iron (III) nitrate, ethanol, and water on a neoprene polishing pad. Etched microstructures were analyzed using optical microscopy (Hirox Digital Microscope KH-7700). Hydrogen and oxygen content of the fabricated solids along with density were analyzed following the same procedure as the powder specimens.

Surface roughness measurements were taken using confocal laser scanning microscopy (Keyence VKx1100) with a 404 nm violet laser source to profile the topology of the sample surfaces. Height maps were taken at 10X magnification. Several surface roughness metrics were calculated using MultiFileAnalyzer software package from Keyence.

2.3 Results

2.3.1 Powder

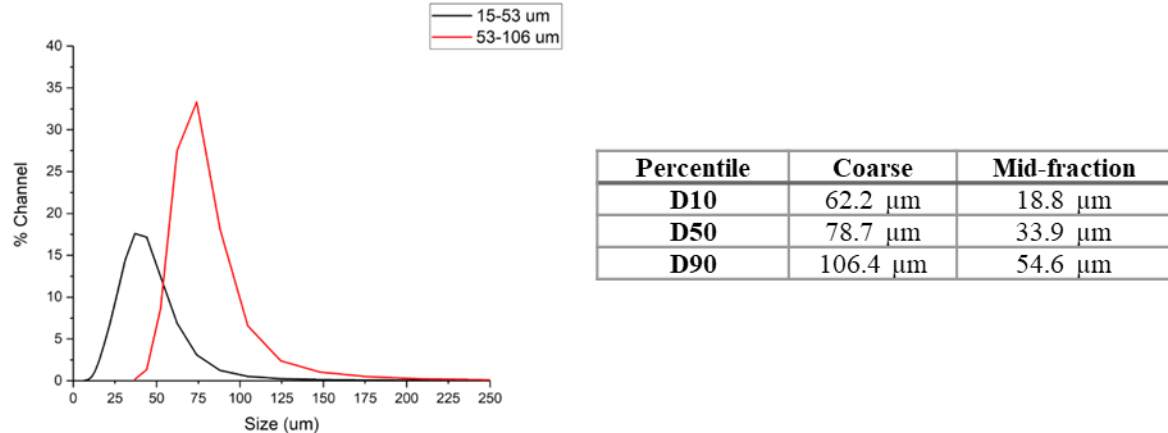


Figure 1: Volumetric particle size distribution of coarse and mid-fraction copper powders

Figure 1 shows the volumetric PSD for both coarse and mid-fraction copper powders as determined by laser diffraction analysis along with the 10th, 50th, and 90th percentiles. Figure 1

shows an overlap of the PSDs but the D10 to D90 percentiles shows that a majority of the powder sizes fall into two separate distributions.

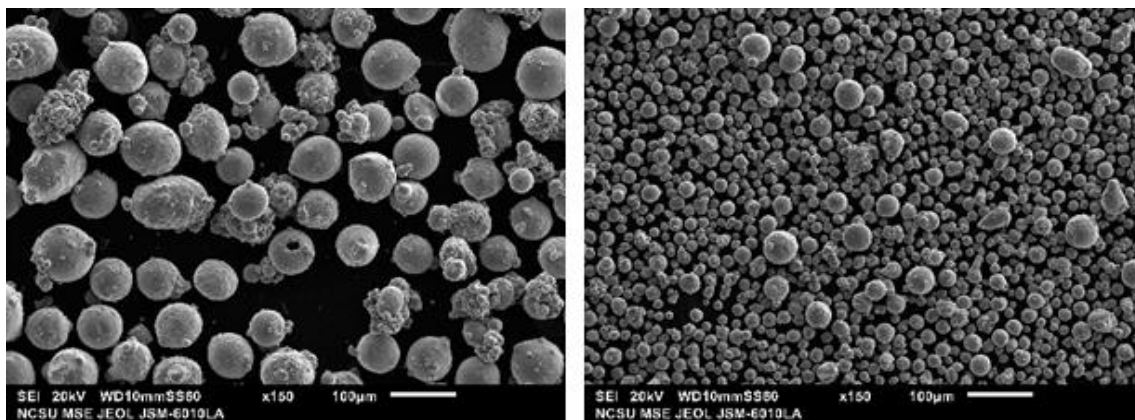


Figure 2: Representative scanning electron micrographs of the coarse (left) and mid-fraction (right) copper powders

Figure 2 shows scanning electron micrographs of both the coarse and mid-fraction copper powders. A noticeable size difference can be seen between the coarse and mid-fraction powders where the large majority of particles have diameters around 75 and 30 μm , respectively. A large majority of particles in the coarse fraction are observed to have satellite particles attached to the surfaces whereas this is less common in the mid-fraction powder.

Table 1: Representative density, relative density, oxygen and hydrogen content for coarse and mid-fraction copper powders

Sample	Density (g/cm^3)	Relative Density (%)	Oxygen Content (PPM wt.)	Hydrogen Content (PPM wt.)
Powder: Coarse	8.81	98.55	650	1
Powder: Mid-fraction	8.87	99.22	745	1

True and relative density determined by nitrogen pycnometry is shown in Table 1. As the PSD reduces, the density of the particles increases mostly likely due to the reduction in trapped gas porosity from the atomization process. The relative density of both powders as compared to OFE solid copper (8.94 g/cm^3) still shows porosity due to processing regardless of PSD. Table 1 also shows the oxygen content as determined by inert gas fusion analysis of the coarse and mid-fraction copper powders. High oxygen content for each of the PSD's can be attributed to surface oxides due to sieving operations carried out in air which increases the thickness of the surface oxide layer. Other contributions could come from oxygen impurities during the atomization process which are located along the grain boundaries as oxides. The mid-fraction PSD has a higher oxygen content than the coarse PSD due to a greater surface area of the smaller particles.

2.3.2 Solid

Figure 3 shows a representative photo of an as-fabricated block attached to an OFE copper build plate. All excess powder was removed from the block prior to sectioning and polishing.

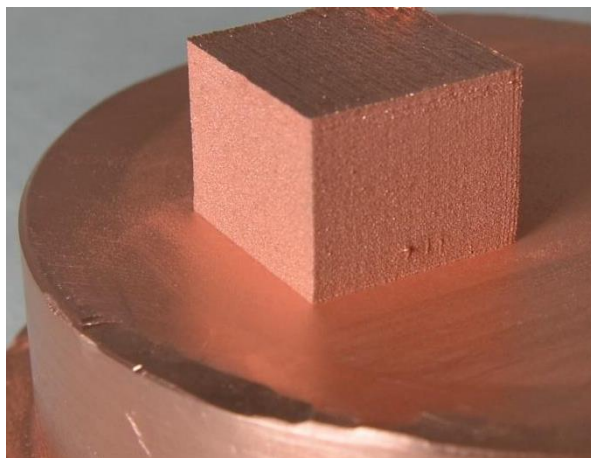


Figure 3: Representative image of the build

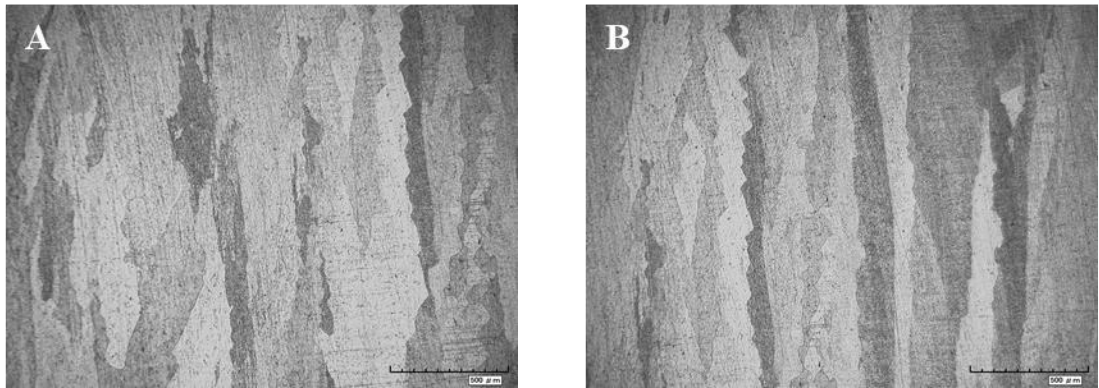


Figure 4: Optical micrographs of solid XZ etched cross-sections fabricated using coarse (A) and mid-fraction (B) copper powders

Figure 4A and 4B show etched optical micrographs of the XZ plane (build direction) from the center of the coarse and mid-fraction solids. The micrographs show a columnar microstructure orientated in the build direction. No significant difference is observed between the coarse and mid-fraction solids.

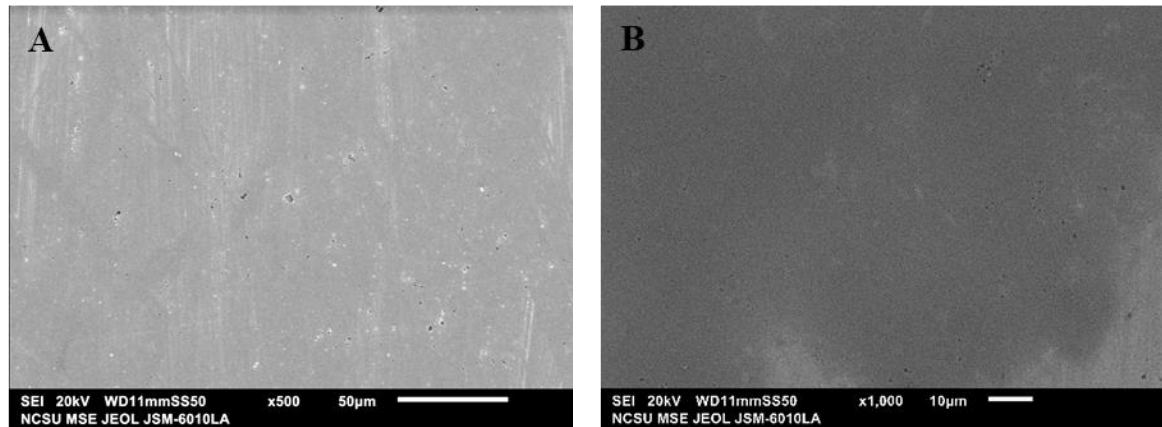


Figure 5: Representative scanning electron micrographs of solid XZ cross-sections fabricated using coarse (A) and mid-fraction (B) copper powders

Scanning electron micrographs show no large-scale porosity from processed induced or trapped gas during the atomization process. However, both the coarse and mid-fraction solids show microporosity on the order of a few microns.

Table 2: Representative density, relative density, oxygen and hydrogen content for coarse and mid-fraction solids

Sample	Density (g/cm ³)	Relative Density (%)	Oxygen Content (PPM wt.)	Hydrogen Content (PPM wt.)
Solid: Coarse	8.87	99.22	630	1
Solid: Mid-fraction	8.91	99.66	750	1

Densities of the coarse and mid-fraction solids show a slight increase over that of the powder densities which is most likely due to the reduction in trapped gas porosity during melting. This can also be inferred from the absence of large scale pores in both solids as seen in Figure 5. Relative densities for both solids exceed 99% of OFE solid copper (8.94 g/cm³) showing that the PSD has little effect on the ability to achieve highly dense solids. No significant change is seen in the oxygen and hydrogen content of the coarse or mid-fraction solids from the initial content of the powder as seen in Table 2. Little to no change is to be expected as the melting process is done under vacuum where further oxidation should not occur.

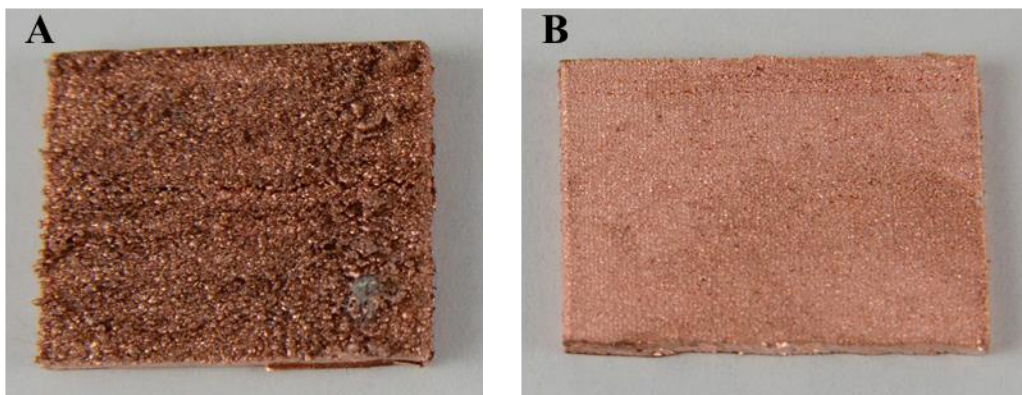


Figure 6: Representative optical images of as-fabricated XZ (side) surfaces of coarse (A) and mid-fraction (B) solids

Representative optical images of the as-fabricated XZ (side) surfaces of the coarse and mid-fraction solids are shown in Figure 6. A large number of particles sintered to the surface are visible on the coarse solid giving rise to an uneven and bumpy surface. Whereas the mid-fraction solid does not appear to have these sintered particles on the surface allowing for a smoother surface. Differences in color can be attributed to varying states of oxidation between the samples due to differences in elapsed time from fabrication to image acquisition.

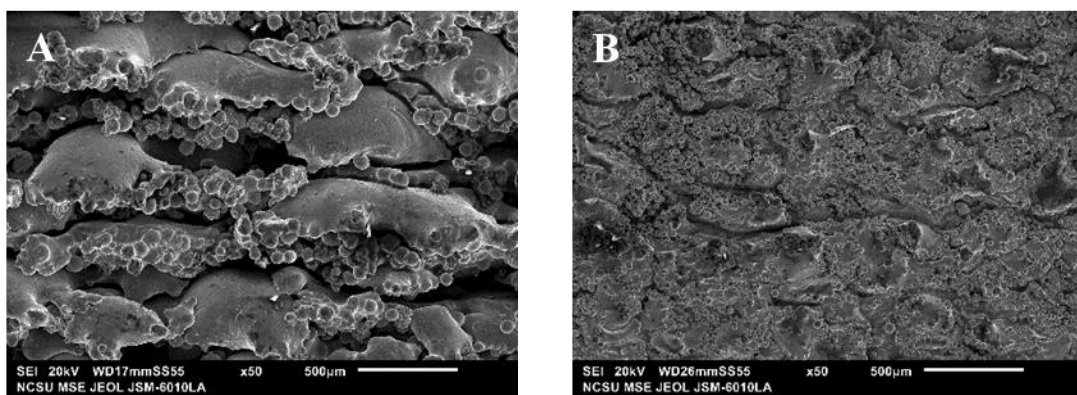


Figure 7: Representative scanning electron micrographs of as-fabricated XZ (side) surfaces of coarse (A) and mid-fraction (B) solids

Figure 7 shows scanning electron micrographs of the as-fabricated XZ (side) surfaces of the coarse and mid-fraction solids. An irregular layer-like structure can be observed in the coarse solid micrograph along with a large amount of sintered powder adhered to the surface. However, the mid-fraction solid does not seem to have any noticeable layering in comparison. Sintered powder is also observed to be adhered to the surface of the mid-fraction solid with the particles having a smaller size distribution than that of the coarse solid.

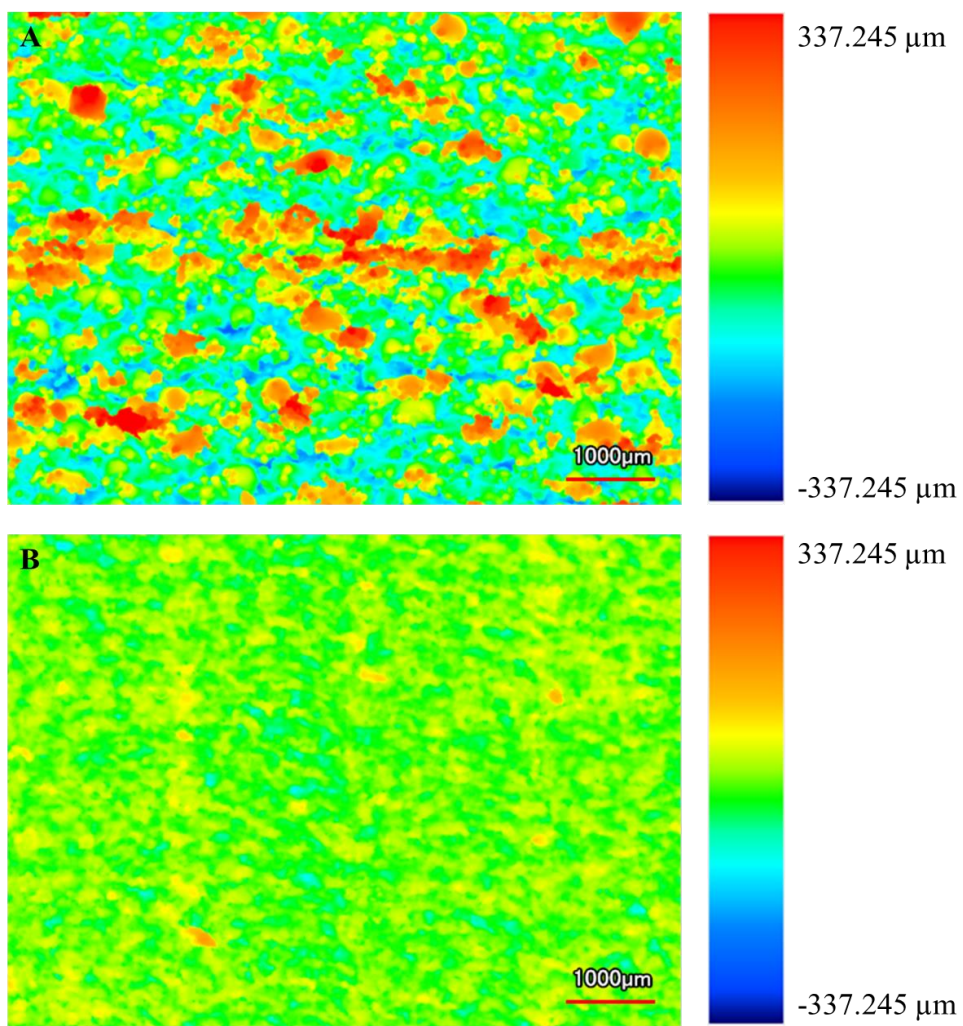


Figure 8: Representative height maps representing surface height of as-fabricated XZ (side) surfaces of coarse (A) and mid-fraction (B) solids

Confocal laser scanning microscopy was used to profile the height of the surface of each of the solids at a magnification 10x. Representative height maps collected using the laser profiling capability of the microscope of the coarse and mid-fraction solids are shown in Figure 8. Both height maps are scaled to use the same range as seen by the scale bar on the right of each image in order to allow for easy comparison in height values. As seen from Figure 8A, the coarse solid has large variations in height as indicated by values ranging across the entire scale of the height map. Whereas the mid-fraction solid has a much smaller range of height values centered on the middle of the scale bar as seen in low variation of color across the map.

Table 3: Surface roughness parameters of as-fabricated XZ (side) surfaces of coarse and mid-fraction solids

Surface Roughness Parameter	Powder Size Distribution	Value (μm)	Standard Deviation (μm)
Sa (Arithmetical Mean Height)	Coarse	82.25	11.63
	Mid-fraction	18.96	0.57
Sq (Root Mean Square Height)	Coarse	104.5	11.48
	Mid-fraction	24.33	0.84

Surface roughness parameters were calculated from the height maps shown in Figure 8 and are listed in Table 3 along with standard deviation for each parameter. Sa (arithmetical mean height) and Sq (arithmetical mean height) were chosen as they have been shown to be suitable metrics for surface roughness of electron beam melted The value for each roughness parameter was computed using an average of 9 overlapping squares each measuring 2.0 mm x 2.0 mm placed in a 3 x 3 grid on the height map. Both Sa and Sq show a substantial difference in the surface roughness between the coarse and mid-fraction solids. Even though the standard

deviation for the coarse solid surface roughness parameters is large, the reduction in surface roughness from the coarse to mid-fraction solid can be seen in the bar plot in Figure 9.

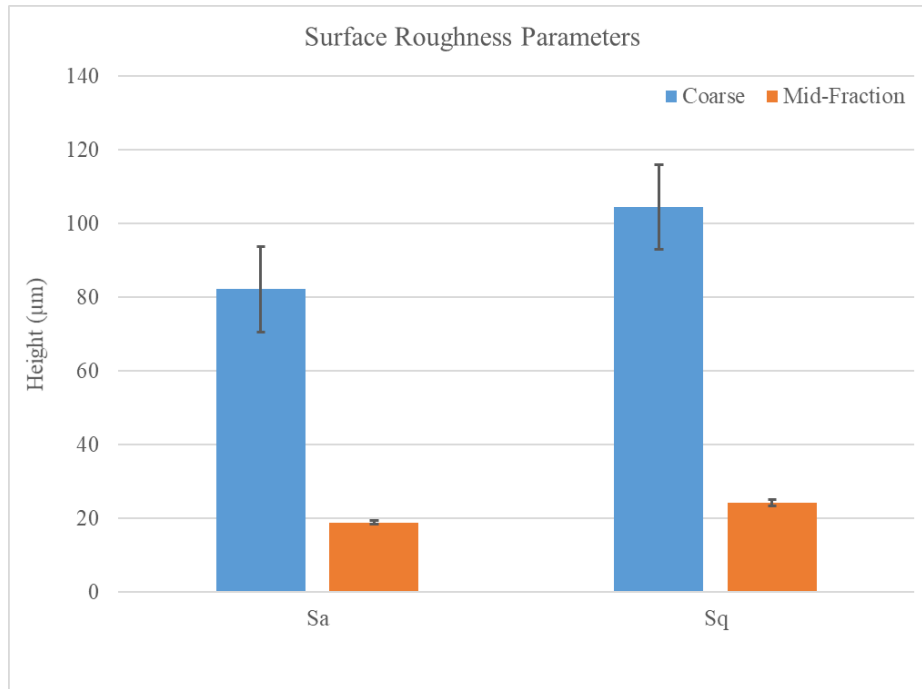


Figure 9: Bar plot of surface roughness parameters for coarse and mid-fraction XZ (side) surfaces

2.4 Discussion

The reduced PSD allowed for the use of a smaller layer thickness during fabrication. A 50 μm layer thickness for the coarse powder is the smallest practical thickness that can be used with this distribution due to the D10 value being 62.2 μm as seen in Figure 1. Any layer thickness smaller than 50 μm would result in most of the powder being too large and be swept away during raking. The mid-fraction powder having a D10 of 18.8 μm allowed for the use of a 20 μm layer thickness which significantly improved the surface roughness of the fabricated

samples. Typically issues fabricating samples with a finer PSD in EB-PBF arise due to the inability for the powder to dissipate the charge imparted by the electron beam during the preheating stage. This is due to the increased volume fraction of the surface oxide with respect to the particle volume [5]. The high electrical conductivity of pure copper helps to enable the use of finer distributions of powder during EB-PBF processing [6].

An additional benefit to using a smaller layer thickness is the reduction in energy needed for melting which gives way to smaller thermal gradients between the solid samples and powder bed. This is evident in Figure 7 by the reduction in amount of sintered powder adhered to the surface of the sample. This sintered powder can have a large effect on surface roughness depending on how heavily sintered the powder is to the surface of the sample and the powder removal method being used to clean the parts.

2.5 Conclusions

By utilizing a finer powder size distribution, this allowed for a reduction in the layer thickness which resulted in the significant reduction in surface roughness of pure copper processed via EB-PBF. This surface roughness reduction will aid in the fabrication of these high-power RF devices where a high surface roughness can cause electrical breakdown. By achieving this finer surface roughness directly from the fabrication process, the overall purity of the device material can be maintained and avoid possible contamination from post processing techniques.

2.6 References

- [1] A. Townsend, N. Senin, L. A. Blunt, R. K. Leach, and J. Taylor, “A Review of Surface Texture Metrology for Additive Manufacturing of Metal Parts,” *Precis. Eng.*, vol. In Press, pp. 34–47, 2016.
- [2] P. Wang, W. J. Sin, M. L. S. Nai, and J. Wei, “Effects of processing parameters on surface roughness of additive manufactured Ti-6Al-4V via electron beam melting,” *Materials*, vol. 10, no. 10, pp. 8–14, 2017.
- [3] G. Strano, L. Hao, R. M. Everson, and K. E. Evans, “Surface roughness analysis, modelling and prediction in selective laser melting,” *J. Mater. Process. Technol.*, vol. 213, no. 4, pp. 589–597, Apr. 2013.
- [4] J. K. Algardh *et al.*, “Thickness dependency of mechanical properties for thin-walled titanium parts manufactured by Electron Beam Melting (EBM)®,” *Addit. Manuf.*, vol. 12, pp. 45–50, Oct. 2016.
- [5] Z. C. Cordero, H. M. Meyer, P. Nandwana, and R. R. Dehoff, “Powder bed charging during electron-beam additive manufacturing,” *Acta Mater.*, vol. 124, pp. 437–445, Feb. 2017.
- [6] J. R. Davis, *Copper and Copper Alloys*. ASM International, 2001.

CHAPTER 3: Characteristics and Processing of Hydrogen-Treated Copper Powders for EB-PBF Additive Manufacturing

Christopher Ledford ¹, Christopher Rock ¹, Paul Carriere ², Pedro Frigola ², Diana Gamzina ³

and Timothy Horn ⁴

- 1) Center for Additive Manufacturing and Logistics, Edward P. Fitts Department of Industrial and Systems Engineering, North Carolina State University, Raleigh, NC 27695, USA;
- 2) RadiaBeam, Santa Monica, CA 90404, USA;
- 3) SLAC National Accelerator Laboratory, Technology Innovation Directorate, Menlo Park, CA 94025, USA
- 4) Center for Additive Manufacturing and Logistics, Department of Mechanical and Aerospace Engineering, Consortium on the Properties of Additive Manufactured Copper, North Carolina State University, Raleigh, NC 27695, USA

Abstract: The fabrication of high purity copper using additive manufacturing has proven difficult because of oxidation of the powder feedstock. Here, we present work on the hydrogen heat treatment of copper powders for electron beam powder bed fusion (EB-PBF), in order to enable the fabrication of high purity copper components for applications such as accelerator components and vacuum electronic devices. Copper powder with varying initial oxygen contents were hydrogen heat-treated and characterized for their chemistry, morphology, and microstructure. Higher initial oxygen content powders were found to not only reduce surface oxides, but also reduce oxides along the grain boundaries and form trapped H₂O vapor inside the particles. The trapped H₂O vapor was verified by thermogravimetric analysis (TGA) and residual gas analysis (RGA) while melting. The mechanism of the H₂O vapor escaping the particles was determined by in-situ SEM heated stage experiments, where the particles were observed to crack along the grain

boundaries. To determine the effect of the EB-PBF processing on the H₂O vapor, the thermal simulation and the validation of single melt track width wafers were conducted along with melting single layer discs for chemistry analysis. A high speed video of the EB-PBF melting was performed in order to determine the effect of the trapped H₂O vapor on the melt pool. Finally, solid samples were fabricated from hydrogen-treated copper powder, where the final oxygen content measured ~50 wt. ppm, with a minimal residue hydrogen content, indicating the complete removal of trapped H₂O vapor from the solid parts.

3.1. Introduction

Applications including particle accelerators and vacuum electronic devices (VEDs) require materials with the highest electrical and thermal conductivity, as well as ultra-high vacuum compatibility. The copper used in these applications approaches the theoretical maximum achievable quality in terms of the purity, density, and metallurgical properties, such as crystallographic texture and grain size. These applications also require intricate designs and extensive metallurgical processing routes, followed by the assembly and brazing or welding of multiple components into a final part. The consolidation of the component assemblies into complex monolithic parts, and the potential for novel designs achievable through additive manufacturing (AM), is desired in order to reduce the cost and improve the component performance and reliability [1–5]. The underlying challenges associated with the AM of high-purity copper, particularly for electron beam powder bed fusion (EB-PBF) and laser powder bed fusion (L-PBF), have been discussed in several recent studies [1,6–11]. The high thermal conductivity of copper rapidly removes heat from the melt pool, promoting high local and global thermal gradients; residual stress accumulation; and distortion, which is exacerbated by the significant difference in thermal conductivity between the consolidated material and the

surrounding powder bed [12–14]. The resulting rapid solidification of the melt pool, coupled with the low viscosity of molten copper, also tends to retain defects such as keyhole porosity [15]. Additionally, the low absorptivity of copper for the lasers used in many commercial L-PBF systems (~1060 nm wavelength) necessitates the use of high-power lasers increasing the recoil pressure, vaporization, spatter, and related defects [16]. However, even with these challenges, several promising results have been reported with densities ranging above 99.95% for non-electronic grade copper [1,7–9] for EB-PBF, and 96.6% for Nd:YAG fiber laser AM processing [17–23].

Despite the progress, achieving the high purity requirements for copper using AM has remained a significant challenge. For accelerator applications, copper typically needs to meet or exceed that of ASTM F68 for Class 1 oxygen free electronic (OFE) copper, which is 0.15176 ohms g/m² or 101.0% of the minimum International Annealed Copper Standard (IACS) at 20 °C [24]. The maximum oxygen content for OFE copper is 0.0005 wt% (5 wt. ppm). The negative influence of oxygen contamination on the electrical, thermal, and mechanical properties of copper is small, but not insignificant. The incoherent Cu₂O found along the grain boundaries has an effect similar to porosity, and less of an influence on electron scattering than the solute contamination that strains the copper lattice. For instance, electrolytic tough pitch (ETP) copper has an oxygen content of ~0.04% (400 ppm) and typically exceeds 100–101% IACS [24–26]. Much more significant is the adverse effect of embrittlement in the copper components caused by an excessive oxygen content during the downstream hydrogen brazing processes [27]. It should be noted that the copper AM literature has either resulted in specimens with a high oxygen content (similar to ETP Cu), or has not reported an oxygen content in the fabricated samples. Of chief concern is the powder feedstock purity. The powder feedstock commonly used in AM is subject to oxygen contamination during

handling, screening, loading, and transport after atomization. At ambient conditions, the oxygen solubility in pure copper is less than 2 wt. ppm [24,28], where the excess oxygen reacts to form cuprous oxide, Cu₂O, as a non-passivating surface film or along the grain boundaries. At higher temperatures (>300 °C), cupric oxide (CuO) and other variants may also form [29,30].

This poses a unique obstacle for the copper powder used in AM, which is typically produced by nitrogen gas atomization, and quickly oxidizes if exposed to ambient conditions at any point in the powder fabrication and handling process. Because of the very high surface area of these small diameter particles, the relative contribution of oxygen from the surface oxide film typically causes the feedstock to exceed 400–600 wt. ppm oxygen. For example, in their study on the EB-PBF fabrication of copper, Raab et al. [7], Lodes et al. [8], and Guschlauer et al. [9] utilize copper powder feedstocks with reported purities of 99.90 wt%, 99.94 wt%, and 99.95 wt%, respectively, while Frigola et al. [1] and Ramirez et al. [10] used powders with 99.99 wt% and 99.80 wt% purity, respectively. In our preliminary studies, a chemical analysis conducted directly after the powder atomization process, and after the screening, indicates that much of the oxygen pickup in the copper powder occurs during the handling, screening, and packaging processes, which are typically carried out in ambient atmosphere.

Preserving even these oxygen contents during the AM melting and solidification process is extremely challenging, and requires near perfect conditions, as imperfect inert or vacuum atmospheres, moisture absorption, complex thermal cycles, powder recycling, and storage exacerbate oxygen pickup. Frigola et al. [1] showed a significant oxidation of feedstock powders after several EB-PBF reuse cycles. Once the oxygen contamination is present in the powder feedstock as oxide films or grain boundary particles, the contamination is directly transferred to

the fabricated AM components [11]. This combination of factors hinders the fabrication of quality copper components by most powder bed AM processes.

Reduction processes may be employed in order to improve the copper feedstock purity for AM processing. Hydrogen, carbon monoxide, and ethanol are commonly employed reducing agents of Cu₂O and CuO in thin films [31–33]. El-Wardany et al. [6] treated copper powders for L-PBF in a heated forming gas atmosphere (4% H₂ + Ar bal.), theorizing that the hydrogen would reduce the surface Cu₂O films into Cu + H₂O, however, no quantitative data on the composition of the powders or solid samples produced were provided [6]. In addition, this study only considered the reduction of oxides from the surface of the Cu powders, and did not address the possibility that hydrogen also reduces the internal oxides. Previous work has shown that the diffusivity of hydrogen in copper is high at elevated temperatures (e.g., ~9.58 m/s² at 400 °C) [34], and that at temperatures above about 400 °C, hydrogen reduces the grain boundary oxides, forming H₂O gas. The larger H₂O molecules do not diffuse, and the resulting pressure forms high pressure steam pores along the grain boundaries [28,35,36]. This well-known embrittlement mechanism is considered detrimental for most traditional copper powder processing routes because of their significant impacts on downstream processing, such as swelling, porosity, and embrittlement, through plastic deformation, work hardening, the reduction of grain boundary area, and material failure at elevated temperatures [28,36–38], as Lin and Hwang demonstrated with the swelling and cracking of copper powders during the sintering of copper heat pipes [36].

On the other hand, PBF processes utilize thin layers of powder, which are spread over a substrate and selectively melted by a focused energy source. In the present work, we hypothesize that this localized processing can be leveraged to liberate the retained H₂O from the hydrogen heat-treated copper powder during melting on a layer-by-layer basis. This results in a significantly

higher copper purity, without the detrimental effects of embrittlement observed in traditional powder metal processes.

Here, the mechanisms for H₂O removal from copper powders is identified through a series of experiments, one building upon the next. First, copper powders of varying initial oxygen contents were treated in a hydrogen atmosphere at elevated temperatures. The temperature that H₂O escapes from these copper powders was determined using thermogravimetric analysis. The powder cracking during H₂O released at these temperatures was observed directly using a scanning electron microscope (SEM) equipped with a heated stage. We confirm the release of H₂O in a single layer melt in a custom EB-PBF setup using residual gas analysis (RGA), and the subsequent chemical analysis of the melted layers. The single melt pool wide thin walled wafers produced with multiple layers of varying hatch spacings confirm the H₂O release from the copper powder in the heated affected zone of the melt pool, and high-speed videos of these melt pools also show that a proportion of this H₂O escapes from the molten during melting. The efficacy of this approach is validated with the fabrication of fully dense parts, and multi-layer samples with a very low oxygen content, with RGA monitoring of H₂O outgassing on a layer by layer basis.

3.2. Materials and Methods

The experiments were performed in order to understand the influence of a hydrogen heat treatment on copper powder feedstocks of varying initial oxygen contents. We evaluated three levels of oxygen content, with and without hydrogen heat treatment. To generate these six conditions, the following methodology was used.

Two separate batches of nitrogen gas atomized copper powder were acquired. For the purposes of this discussion, the powders were categorized based on the initial measured oxygen content. The lowest oxygen content powder received was between 100–200 wt. ppm oxygen, and is referred

to as low oxygen copper (LO-Cu). The second powder batch with 400–700 wt. ppm oxygen is referred to as medium oxygen content powder (MO-Cu). A selected amount of the received MO-Cu powder was intentionally oxidized to above 1000 wt. ppm oxygen, and is referred as high oxygen content copper (HO-Cu).

3.2.1. Feedstock Preparation

Spherical MO-Cu powder was received with a nominal 15–53 μm particle size distribution (d10–d90), smaller than what is typical for other materials used in EB-PBF (e.g., Ti6Al4V). Nevertheless, it is consistent with previous studies in copper AM by our group [4], and compared to early work by our group and others, also results in a significantly reduced surface roughness [1]. In order to maintain a comparatively low oxygen content in the LO-Cu powder, special consideration was given to the packaging, handling, and screening steps post atomization. This powder was received in the as-atomized ($-250 \mu\text{m}$) condition, directly from the manufacturer, and screened to a nominal 15–53 μm particle size distribution within an argon glove box. To generate the HO-Cu powder, a methodology similar to that of Nieh and Nix [28,30] was utilized. A portion of MO-Cu was treated at 150 °C for 1 h in one atmosphere of air, and cooled at a rate of 5 °C per minute. The temperature was kept lower in the current study, compared with the 800 °C used by Nieh and Nix, to prevent the sintering of the small powder size distribution. Given that the diffusion of oxygen in copper is $2\text{e}^{-11} \text{ m}^2/\text{s}$ at 400 °C [39], the oxygen penetration depth exceeded the particle diameters used in this study during the 2-h treatment, which is confirmed by subsequent focused ion beam (FIB) sectioning of individual powder particles.

Portions of the powder from each of the three batches, LO-Cu, MO-Cu, and HO-Cu, were then exposed to hydrogen treatment at 400 °C for 4 h under one atmosphere of flowing pure hydrogen, and cooled at a rate of 5 °C per minute in a dry hydrogen atmosphere heating cover

retort furnace. A custom stainless-steel fixture comprised of stacked circular trays allowed the processing of 1 kg of powder per treatment cycle in 2 mm thick layers, as shown in Figure 1. To avoid oxygen contamination after hydrogen treatment, the powders were packed in vacuum-sealed foil bags after purging with dry nitrogen. The vacuum bags were then sealed in a second bag filled with dry nitrogen. All of the copper powders were subsequently stored, handled, and sampled in an argon or nitrogen atmosphere.

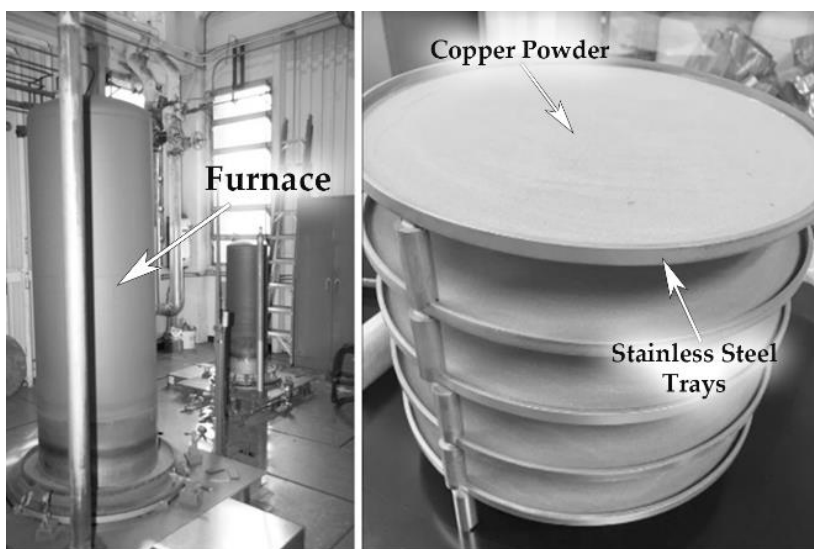


Figure 1. Hydrogen brazing furnace at SLAC National Accelerator Laboratory Technology Innovation Directorate (TID) (left), and stacked-stainless steel fixture (right) for treating multiple trays of copper powder in 2-mm thick layers.

3.2.2. Feedstock Characterization

Each of the three powder conditions were characterized before and after hydrogen treatment, for size distribution by laser diffraction (Microtrac S3500, Microtrac Inc., Montgomeryville, PA, USA), and density by nitrogen pycnometry (ASTM B923-16, Quantachrome MicroUltrapyc 1200e, Quantachrome Instruments, Boynton Beach, Florida, USA). The oxygen and hydrogen

content of all the powders were quantified by inert gas fusion analysis (LECO OHN836, LECO, St. Joseph, MI, USA). The reported values herein were acquired immediately prior to the experiments. The powder morphology was characterized by a JOEL 6010LA scanning electron microscope (JEOL USA, Inc., Peabody, MA, USA). An additional powder characterization was performed on individual powder particles using focused ion beam (FIB) milling for the cross-sectional analysis by secondary electron and gallium ion contrast on a FEI Quanta 3D Field Emission Gun (FEG) (Thermo Fisher Scientific, Hillsboro, Oregon, USA). Scanning transmission electron microscopy (STEM) analysis and energy dispersive spectroscopy (EDS) were performed on a FEI Talos (Thermo Fisher Scientific, Hillsboro, Oregon, USA), to assess the chemical composition, size of surface, and internal oxide species.

A thermogravimetric analysis (TGA) was performed using a TA SDT 650 Simultaneous Thermal Analyzer (TA Instruments, New Castle, DE, USA) under flowing nitrogen, while the samples were heated at 5 °C/s to 600 °C in an alumina sample holder in order to identify the temperature at which the H₂O can escape from the treated copper powders.

3.2.3. In-Situ Heated Stage

In-situ heated stage SEM degassing experiments were performed on a FEI Quanta 3D FEG so as to observe the mechanism of H₂O gas release from a single copper powder particle. Both hydrogen heat treated copper particles and untreated copper particles were separated from the adjacent powder feedstock with a single fiber brush using a light microscope at 50× magnification. Individual powder particles were then placed onto a SiC heated stage (Protochips Fusion) for controlled heating under standard SEM operating conditions. The stage was ramped to a maximum temperature of 400 °C at 100 °C/s, and image sequences were made at 30 fps with secondary electron detectors.

3.2.4. Customized EB-PBF Platform

All of the electron beam melting (EBM) experiments were conducted using a customized Arcam A2 EB-PBF system (Arcam Build Control Software V3.2, SP2, Arcam AB, Sweden). While the EB-PBF operation and process parameters have been described in detail elsewhere [40], it is important to highlight that in this work, the internal components of the commercial system have been removed and replaced with a custom 304 stainless steel build tank, platform, and powder feeder system. The customized chamber was designed with viewports that are oriented radially about the vertical axis of the electron beam column at a 55° angle to the surface of the experimental substrate/fixture, in order to view the entire build surface. The experiments were monitored with by an emissivity corrected single color pyrometer (Fluke Process Endurance Pyrometer, Fluke, Everett, WA, USA), a visible light camera (Nikon D7000, Nikon, Melville, NY, USA), a 200-amu residual gas analyzer (Stanford Research Systems, Sunnyvale, CA, USA), and an IR thermal imaging camera (FLIR A655sc, FLIR, Wilsonville, OR, USA). The viewport window materials varied as a function of the transmittance requirements for each instrument. Figure 2 shows a photograph of the customized setup.

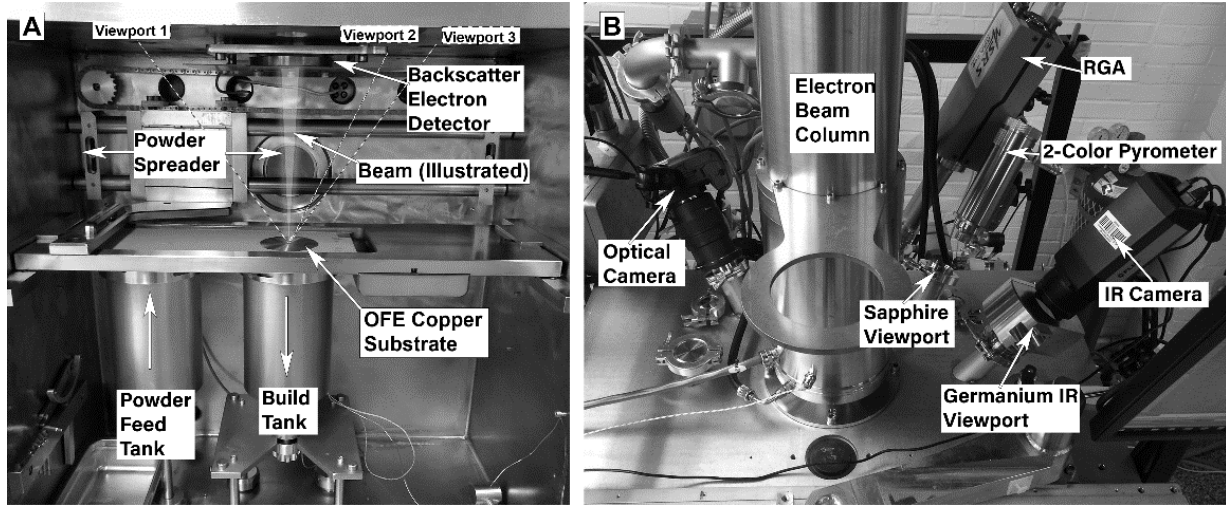


Figure 2. Photographs of the customized Arcam A2 electron beam melting system, showing the interior of the vacuum chamber, mechanical components and in-situ backscatter electron (BSE) detector (**A**), and the exterior of the vacuum chamber, showing the electron beam column and the location of instrumentation and viewports (**B**). The line of sight of the visible light camera, pyrometer, and IR camera are illustrated by the dashed lines in 2A, from viewports 1, 2, and 3, respectively.

3.2.5. Simulation and Validation of Variable Spacing Single Melt Track Width Wafers

We hypothesized that during melting, H₂O vapor escapes from both the liquid melt pool and from powder in the heat affected zone. For the powder adjacent to the melt pool, the internal pressure of the H₂O vapor overcomes the mechanical strength of the grain boundary, and the pore begins to expand in size. This leads to the fracturing of the particle along the grain boundaries and a release of H₂O vapor into the vacuum system. To explore this, single melt track width scenarios were simulated at various hatch spacings, utilizing the 3D transient heat transfer model developed by Lee et al. [41] at the Oak Ridge National Laboratory. Calculations were made using FEniCS software (2019.1.0, FEniCS), utilizing python scripts, and the thermal model output was analyzed

using ParaView visualization software (v5.7, Kitware Inc., Clifton Park, NY, USA). The simulation used variables including heat input, beam speed, thermal conductivity, and so on, to model the EB-PBF process and the temperature profile across a solid plate with the thermophysical properties of a comparable copper powder bed during different operating conditions. The simulation variables used in this study are listed in Appendix A.

Based on the model results, single melt track width wafers 13 mm long and 10 mm tall were fabricated using hydrogen-treated HO-Cu powder with 2.0 mm on center spacings, as shown in Figure 3. The build substrate was a machined OFE copper substrate that measured 90 mm in diameter and 30 mm in thickness. During the EB-PBF processing, the build temperature was maintained at 270 °C, measured by a thermocouple attached to the bottom of the plate, and the partial pressures of H₂O vapor and other gas species were monitored using the RGA. Each wafer was melted with a line energy of 0.8 J/mm (600 mm/s, 8 mA, 0 mA focus offset) and layer thickness of 40 µm, with the power analyze function (Arcam specific thermal controls) disabled. The beam scan direction was constant (left to right) for each wafer and each layer.

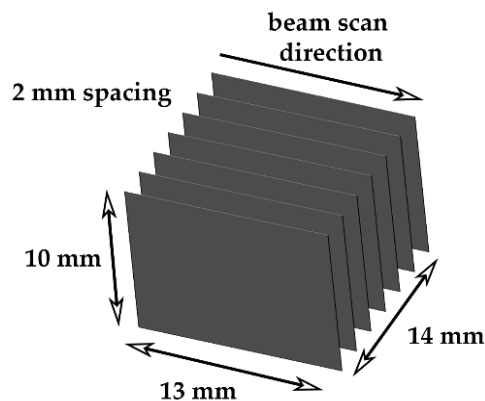


Figure 3. Illustration of the single melt track width geometry with 2.0 mm spacing.

Powder was harvested from between the wafers in a serial fashion, as a function of the distance from the solid copper wall.

Upon the build completion, each block of wafers was removed from the surrounding sintered powder and build surface using a razor blade. The sintered powder cake between the solid wafers was serially sectioned with a razor blade as a function of the distance from the melt pool, and placed on carbon tape for the SEM analysis. Additionally, the top surface of the intact sintered cake was analyzed on a JOEL 6010LA, in order to observe sintered powder characteristics at specific distances from the melt track.

3.2.6. EB-PBF Processing of Hydrogen-Treated Copper Powder

To directly observe and quantify the H₂O release during EB-PBF, single layer discs were melted using the various hydrogen-treated and untreated powders. Figure 4 illustrates the experiment. The fixture upon which the experiments were carried out was an annealed OFE copper cylinder, 100 mm in diameter and 50 mm thick. Six equally spaced cylindrical pockets, measuring 25 mm in diameter by 3 mm deep were milled into the surface at a radial distance of 30 mm from the plate center, such that each pocket is effectively isolated from the others, as seen in Figure 4. After the machining, the copper substrate was cleaned using a standard ultra-high vacuum (UHV) protocol for machined copper.

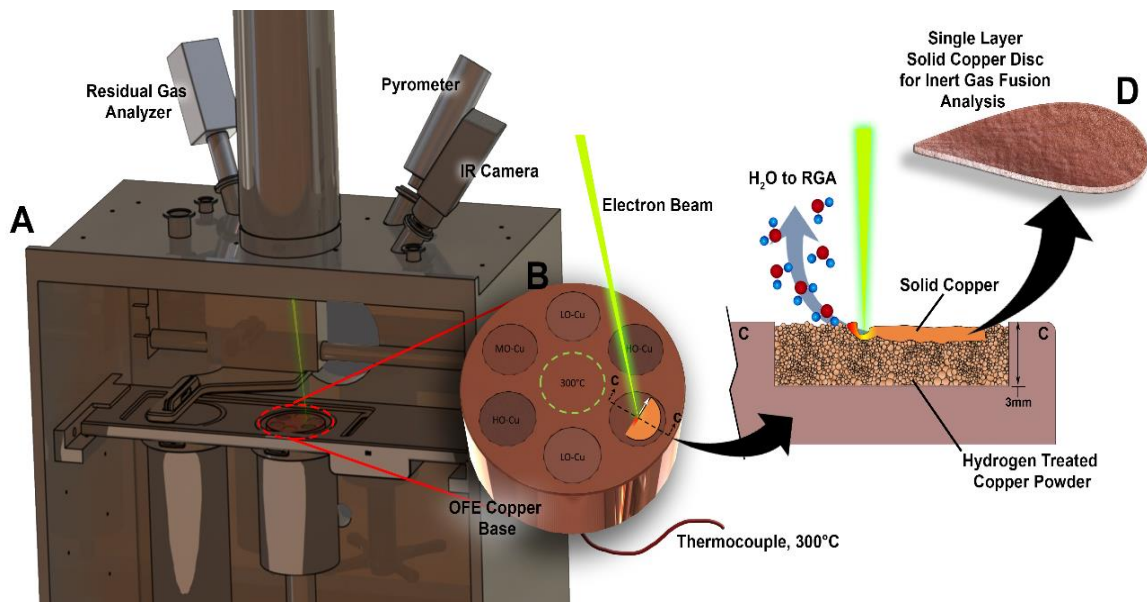


Figure 4. Illustration of the in-situ H_2O vapor out-gassing experiment. The electron beam melting (EBM) vacuum chamber is outfitted with a residual gas analysis (RGA) and IR camera, and the surface temperature is monitored by a two-color pyrometer and thermocouple (**A**). The base fixture contains six 3 mm deep pockets (**B**), which are filled with hydrogen-treated and untreated powders with varying initial oxygen content. A single layer disc is melted on the top surface of each powder type. During melting, H_2O is released from the powder or melt pool, and detected by the RGA (**C**). Upon completion, the powder is manually removed from the solid disc of copper, which is analyzed for oxygen and hydrogen content by inert gas fusion (**D**).

Each of the pockets in the substrate were filled and leveled to the top surface of the plate with ~5 grams of LO-Cu, MO-Cu, or HO-Cu powder before or after hydrogen treatment, each having a replicate. The oxygen and hydrogen content of the powder, as noted previously, was measured by inert gas fusion prior to this experiment. A type K thermocouple was affixed to the bottom of

the substrate, and the substrate was placed on top of the build piston, which allows for the thermal isolation from the system.

The vacuum chamber was evacuated to a pressure of $3.75 \times e^{-5}$ Torr, and the copper substrate was heated by repeatedly scanning the defocused electron beam in a circular area, 25 mm in diameter at the center of the substrate, with a beam current of ~2–4 mA. The substrate temperature was measured by the thermocouple at the bottom, and a two-color pyrometer through a sapphire window positioned in one of the upper viewports.

The substrate heating was manually modulated until both of the temperature readings agreed within 5% of the target value (300 °C), and then this temperature was maintained for a 2 h outgassing cycle. A 200 amu residual gas analyzer (SRS-RGA200) was used to measure the partial pressure of the gas species of interest for this study (O, H, N, NO, NO₂, and H₂O). During the outgassing cycle, the background H₂O partial pressure was observed to decrease and stabilize at ~8 $\times e^{-7}$ Torr. This outgassing period at 300 °C also allowed sufficient time for the initial stages of sintering to take place within the powder. This was observed with the IR camera by a uniform emissivity shift across all six powder pockets.

The focused electron beam was then raster scanned over an area measuring 20 mm in diameter on the surface of each one of the powder pockets. A line energy of 0.8 J/mm (600 mm/s, 8 mA, 0 mA focus offset, 100 μm hatch offset) was sufficient to melt and consolidate a single layer of copper supported underneath by the sintered powder. The melting process was recorded by the thermal imaging camera through a germanium port at 25 Hz, and by in-situ monitoring of the back scattered electron signal. A thermal video of the melting process is available in the supplemental data. During the melting, the outgassing of the key gas species was monitored by the RGA at 1 Hz. This process was repeated on each powder pocket with approximately 10 min to pass between

each raster melt in order to allow for the RGA partial pressures and substrate temperature to stabilize. The solids samples were then cooled under a vacuum to room temperature.

The material in each pocket was removed from the substrate and the sintered powder was mechanically removed from the solid wafer with a wire brush in an inert gas glove box. The oxygen and hydrogen content of both the sintered powder and solid wafer from each pocket were measured by inert gas fusion (LECO Form 203-821-455, LECO OHN836, LECO, St. Joseph, MI, USA). The experiment was repeated several times, varying the position of each powder type and the order in which powders were melted.

3.2.7. High Speed Footage of Melt Pool

In order to directly observe the H₂O vapor escaping from the melt pool, a Photron SA-X2 high-speed camera was utilized to capture the footage at 30,000 frames per second, at a focal length of 30 cm. The footage was captured for both a hydrogen-treated LO-Cu and HO-Cu melt pool using the same procedure for the EB-PBF processing as described in Section 2.6.

3.2.8. Solid Sample Fabrication

To validate the process for fabricating the components of high purity copper with hydrogen heat-treated powders, solid cylindrical specimens measuring 15 mm in diameter were fabricated for the microstructural and chemical analysis, using both untreated and hydrogen-treated MO-Cu powder. The untreated powder had an oxygen content (~600 wt. ppm) similar to what was used in the studies by Frigola et al. [1], Lodes et al. [8], and Guschlbauer et al. [9]. The processing parameters used were 600 mm/s, 8 mA, 18 mA focus offset, and 120 μm hatch offset with a 40 μm layer thickness. This falls within the processing space (~166 J/mm³) used by both Frigola et al. [1] and Guschlbauer et al. [9]. The build temperature was maintained at 300 ± 10 °C for the

duration of the fabrication. The gas species in the chamber were monitored during the fabrication process using the RGA, as described earlier.

3.3. Results

3.3.1. Powder Characterization

Table 1. Chemical content of copper powders.

Powder ID	Condition	Average O ₂ (wt. ppm)	Standard Deviation (wt. ppm)	Average H ₂ (wt. ppm)	Standard Deviation (wt. ppm)
LO-Cu (15–53 um)	Untreated	226.51	11.36	0.87	0.56
	Hydrogen	54.76	8.34	1.56	0.97
	Treated				
MO-Cu (15–53 um)	Untreated	462.17	18.87	1.81	0.66
	Hydrogen	282.33	3.79	31.83	2.02
	Treated				
HO-Cu (15–53 um)	Untreated	1507.33	12.70	1.95	0.99
	Hydrogen	586.97	35.28	76.44	5.77
	Treated				

The oxygen and hydrogen content were carefully tracked after the atomization, screening, and hydrogen treatment. Table 1 shows the oxygen and hydrogen content for the untreated and hydrogen treated LO-Cu, MO-Cu, and HO-Cu screened powders. The LO-Cu powder was procured as-atomized and was sieved in-house under argon in order to maintain a low oxygen content of ~225 wt. ppm and ~1 wt. ppm hydrogen. After the hydrogen treatment of the LO-Cu powder, the oxygen content was reduced to ~50 wt. ppm, with minimal change in the hydrogen content. The untreated MO-Cu powder contained ~450 wt. ppm oxygen and ~2 wt. ppm hydrogen, and after hydrogen treatment, the oxygen content was reduced to ~280 wt. ppm, but the hydrogen

content increased to ~30 wt. ppm, indicating that the hydrogen was retained within the powder after treatment, likely as trapped H₂O, which is consistent with the reported literature by Nieh and Nix [28,30]. As a third condition, the HO-Cu was intentionally oxidized in order to exaggerate the effects of oxygen, and produced an extreme condition with oxygen measured at ~1500 wt. ppm and ~2 wt. ppm hydrogen. After the hydrogen treatment of the HO-Cu powder, the oxygen content was reduced to ~580 wt. ppm, but the hydrogen content increased to ~75 wt. ppm, again most likely trapping H₂O inside the particles. No significant sintering is observed after the powders undergo the hydrogen treatment. Figure 5 shows a plot of the atomic percent of oxygen versus the atomic percent of hydrogen for all of the hydrogen heat-treated copper powders used in this study. The 2:1 stoichiometric relationship is a key indicator that hydrogen is retained in the powder in the form of H₂O vapor. It is also notable that the linear relationship is offset by ~0.06% at. % oxygen, which can be accounted for volumetrically on the surface of the powder particles.

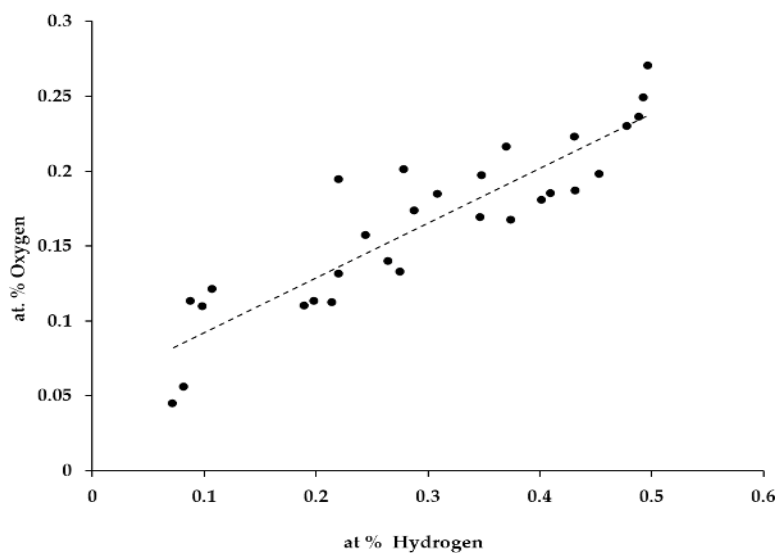


Figure 5. Plot showing at. % oxygen versus at. % hydrogen for all of the hydrogen heat-treated copper powders used in this study.

Further evidence for the formation of H₂O vapor induced cavities in the powder is supported by the nitrogen pycnometry results for each powder condition (shown in Figure 6). No significant change in density is seen after the hydrogen treatment of the LO-Cu particles from the untreated condition. Without internal, grain boundary Cu₂O, the hydrogen does not react to form H₂O vapor. However, both the MO-Cu and HO-Cu particles show a decrease in density after hydrogen treatment, which is likely caused by the formation of H₂O in the particles due to the significant difference in densities between H₂O (1 g/cm³) and copper (8.96 g/cm³). The decrease in density among the as received powders can be attributed to the increasing contribution of Cu₂O with the increasing oxygen content, which has a density of only ~6 g/cc.

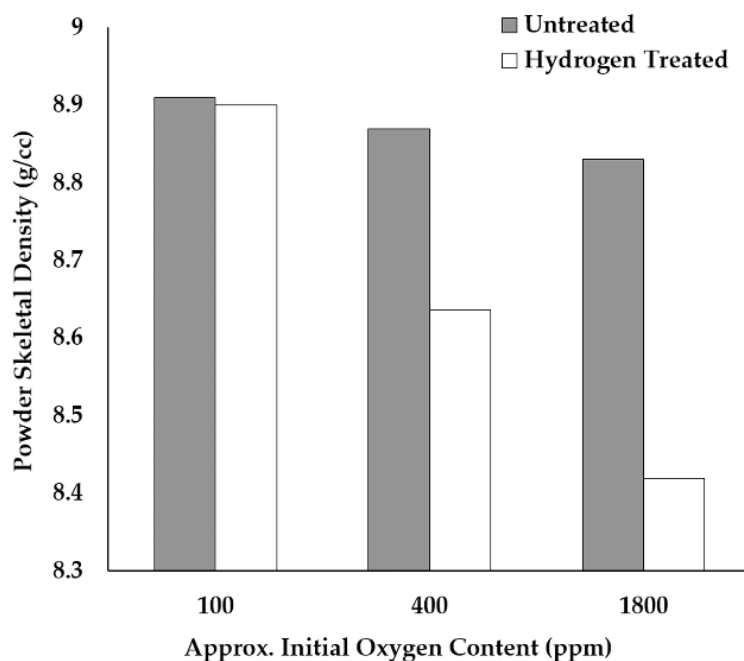


Figure 6. Plot showing the skeletal density of the untreated and hydrogen heat-treated copper powders of varying initial oxygen content, as measured by nitrogen pycnometry.

Because of its relatively high oxygen content, the MO-Cu powder was selected to observe the effect of hydrogen heat treatment on the surface oxides. Figure 7 shows the representative low and

high magnification scanning electron micrographs of (Figure 7A and Figure 7C) and the hydrogen-treated (Figure 7B and Figure 7D) MO-Cu powder. Figure 7C shows the surface of the untreated MO-Cu powder, where bright spots were identified as oxygen-rich copper particles. Figure 7D shows the surface at the same magnification after the hydrogen treatment of the MO-Cu powder, where the surface oxides have been largely removed. These results were typical for untreated and hydrogen-treated MO-Cu and HO-Cu particles.

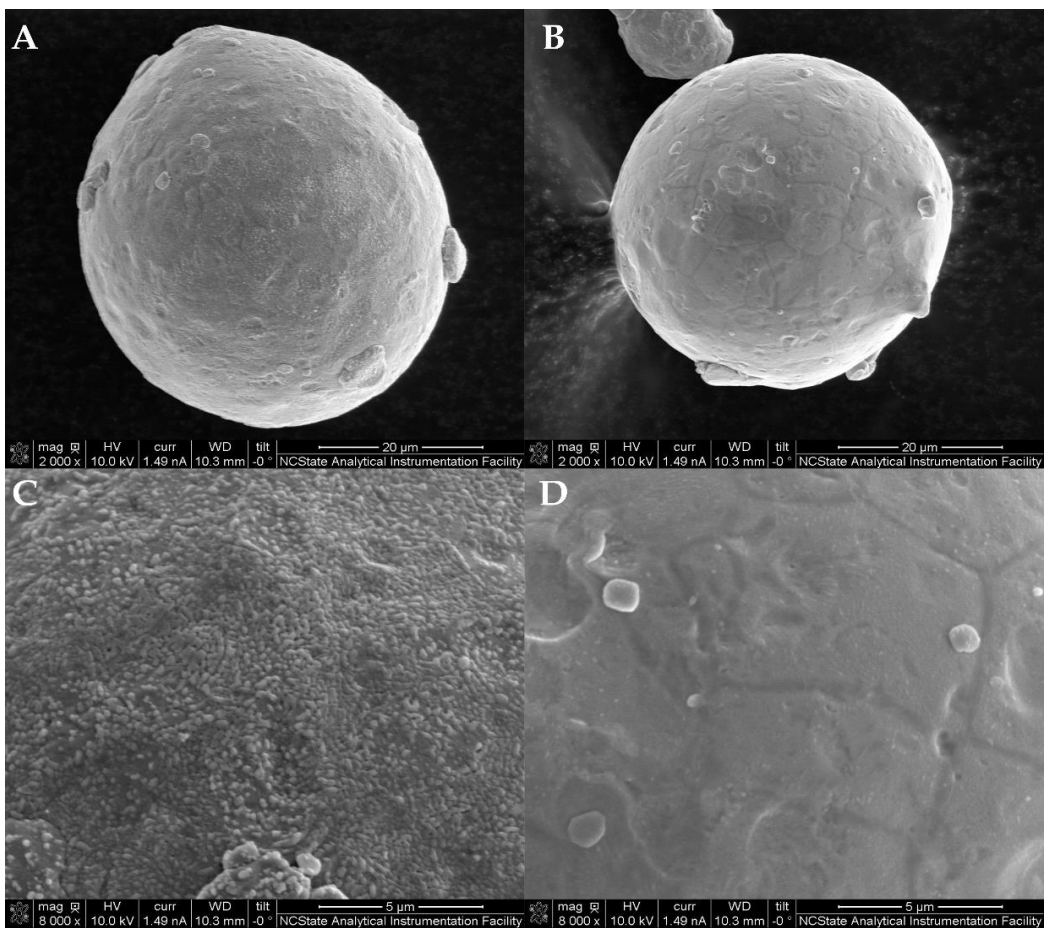


Figure 7. Representative low and high magnification scanning electron micrographs of untreated and hydrogen-treated MO-Cu powder. **(A)** Low magnification and **(C)** high magnification of untreated hydrogen-treated MO-Cu powder; **(B)** Low magnification and **(D)** high magnification of hydrogen-treated MO-Cu powder.

The representative particles were serial sectioned using a FIB to reveal the internal structure of the untreated and hydrogen-treated powder of each type using ion channel imaging, as shown in Figure 8. Figure 8A is an ion image of a sectioned untreated LO-Cu particle showing no obvious porosity or oxide-rich particles. Figure 8B and Figure 8C are cross-sectioned MO-Cu and HO-Cu particles, respectively, which have fine equiaxed microstructures and submicron oxygen-rich particles along the grain boundaries. The distribution of oxide particles along the grain boundaries vary by size, where larger oxides tend to be located at triple points, and smaller oxides along the grain boundaries. Figure 8D shows a hydrogen-treated LO-Cu particle with minimal change after hydrogen treatment because of its initially low oxygen content. The LO-Cu particles, produced with a special handling consideration, consistently showed few to no internal oxides (within the resolution of the instrument). A grain boundary is shown in Figure 8A and Figure 8D. However, the lack of contrast between the two grains can be attributed to the similarity of the grain orientations. Figure 8E shows a hydrogen-treated MO-Cu particle with both a micron and submicron scale porosity throughout the grain boundaries. The high oxygen content of the HO-Cu particle leads to the formation of a significant interconnected porosity at the grain boundaries after hydrogen heat treatment. Several large pores are evident after hydrogen treatment in Figure 8E and Figure 8F for MO-Cu and HO-Cu, respectively; however, in both cases, small dark features are evident along the grain boundaries. It was not immediately clear from this SEM analysis whether these were residual, unreacted oxides or small water vapor induced pores. Videos of the serial sectioning process using FIB are provided in the supplemental data for each of the cases in Figure 8. The HAADF STEM imaging and EDS (Figure 9) of a grain boundary triple point of hydrogen heat-treated MO-Cu confirms the presence of the H₂O vapor induced porosity, consistent with the observations of Nieh and Nix [28,30].

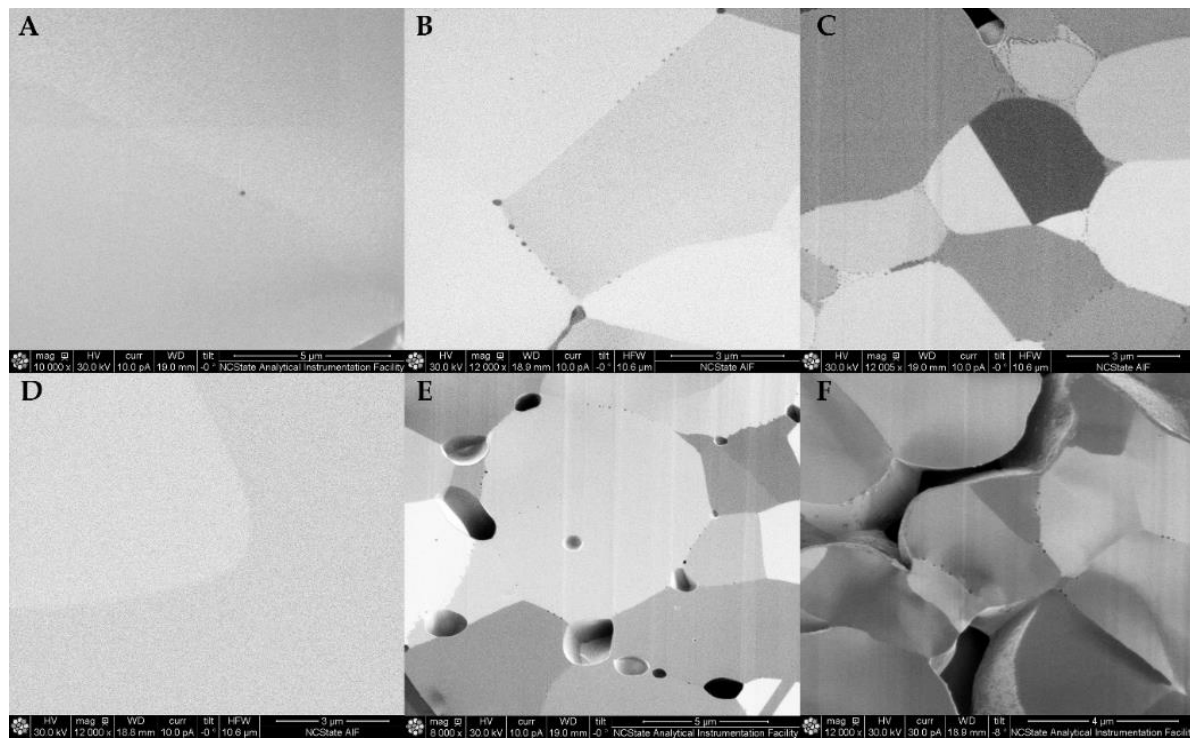


Figure 8. Representative high magnification ion channeling contrast micrographs of pretreated LO-Cu (**A**), MO-Cu (**B**), HO-Cu (**C**), and post hydrogen treatment LO-Cu (**D**), MO-Cu (**E**), and HO-Cu (**F**) focused ion beam (FIB) sectioned Cu powder particles showing the presence of grain boundary Cu₂O in the untreated condition (**A–C**), which reacts with hydrogen to form H₂O pores (**E,F**). LO-Cu powder lacks significant grain boundary oxides, and therefore does not exhibit H₂O vapor induced porosity. Note that scale bars vary in the images.

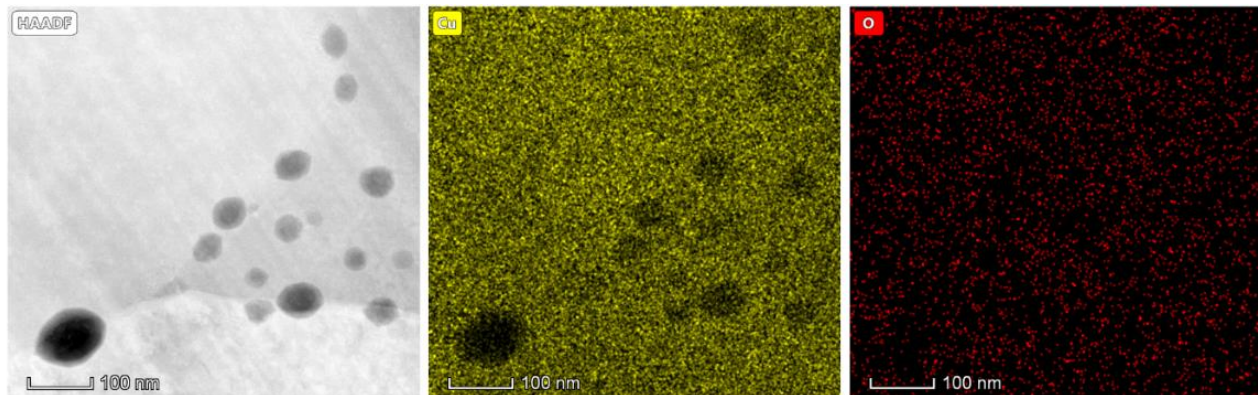


Figure 9. HAADF STEM micrograph and energy dispersive spectroscopy (EDS) of hydrogen-treated MO-Cu powder grain boundary triple point showing submicron scale H₂O vapor induced porosity.

Figure 10 shows the results of the thermogravimetric analysis (TGA) of untreated and hydrogen-treated powders for the three initial oxygen contents. A TGA was carried out to ascertain the temperature at which the internal pressure of the H₂O vapor pores exceeds the grain boundary strength of the copper powder particles. All of the untreated powders demonstrate no significant change in weight loss after heating to 600 °C at 5 °C/s. However, both hydrogen-treated MO-Cu and HO-Cu powders experience weight loss beginning at 375 °C, which then stabilizes at approximately 525 °C. Hydrogen-treated LO-Cu powder also shows minimal mass change while heating when compared to the hydrogen treated MO-Cu and HO-Cu particles. The weight loss can be correlated to the initial oxygen content of the powder before hydrogen treatment, indicating an increased presence of H₂O in the hydrogen-treated particles at higher oxygen contents.

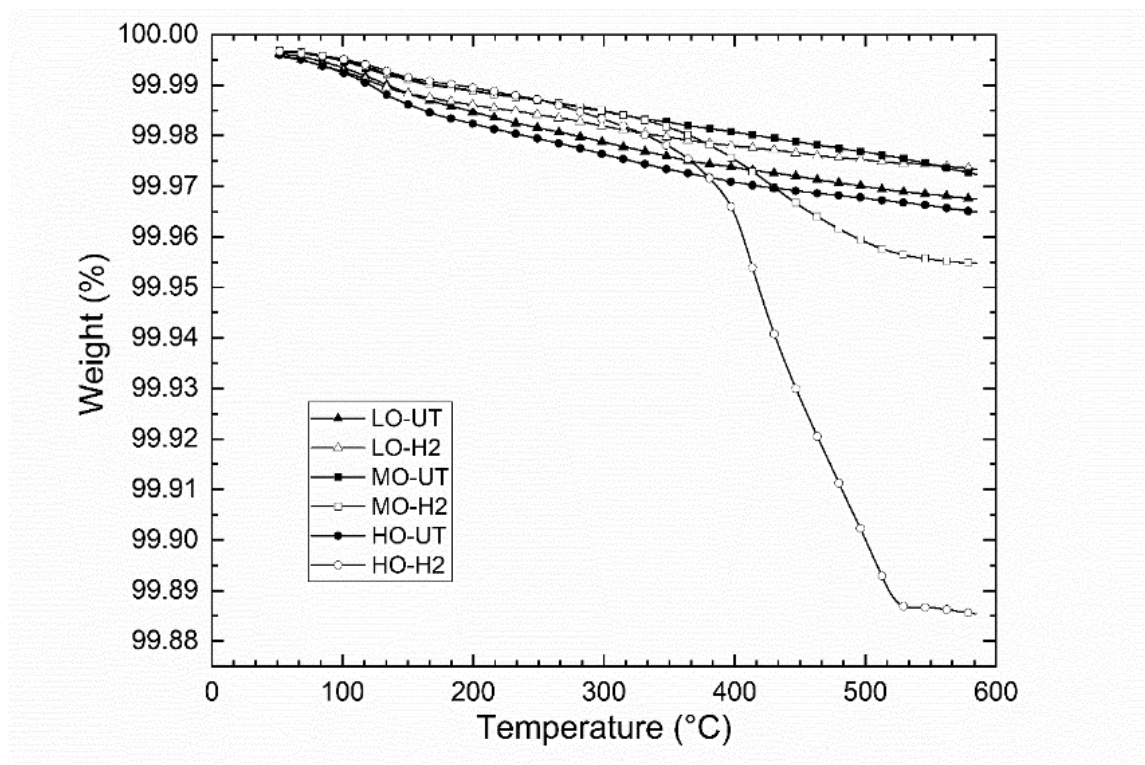


Figure 10. Thermogravimetric analysis of untreated and hydrogen-treated LO-Cu, MO-Cu, and HO-Cu powder under flowing nitrogen.

To directly observe the mechanism for the H₂O release during the heating of the treated powders, treated and untreated particles were heated to 400 °C, and then to melting at 1200 °C, using an in-situ SEM heating stage (Protochips Fusion). It is important to note that the reported temperature is that of the surface of the heating elements, not necessarily the equilibrium temperature of the particles. The temperature of the stage is calibrated with a pyrometer and correlated to the input current. Here, it is assumed that the mass of the particle is small compared with the input power, and that the equilibrium temperature is reached quickly. This assumption is corroborated by the data acquired from multiple sources in this study (TGA, in-situ EB-PBF, etc.). A temperature of 400 °C was chosen for imaging, based on the onset temperature of weight loss observed by TGA. Figure 11A shows a typical hydrogen-treated HO-Cu particle at room

temperature. Additional treated and untreated particles are included as supplemental video files. This particle was placed on the SiC chip in the SEM, and heated in-situ to 400 °C at 100 °C/s. Figure 11B is an SEM image of the particle surface at 400 °C immediately after fracture lines are observed, as H₂O vapor escapes from the particle, illustrated by the arrows. Subsequently, as shown in the supplemental videos, the fracture lines close and heal through diffusion mechanisms.

Figure 11C shows images of another particle surface at 400 °C immediately after the onset of the grain boundary fracture. In this case, the particle was quenched from this condition, and subsequently cross sectioned with a FIB, which reveals interconnected porosity along the grain boundaries inside the particle (Figure 11D). Here, the release of H₂O vapor at 400 °C causes the interconnected porosity along the grain boundaries underneath the particle surface, with an additional porosity towards the center of the particle.

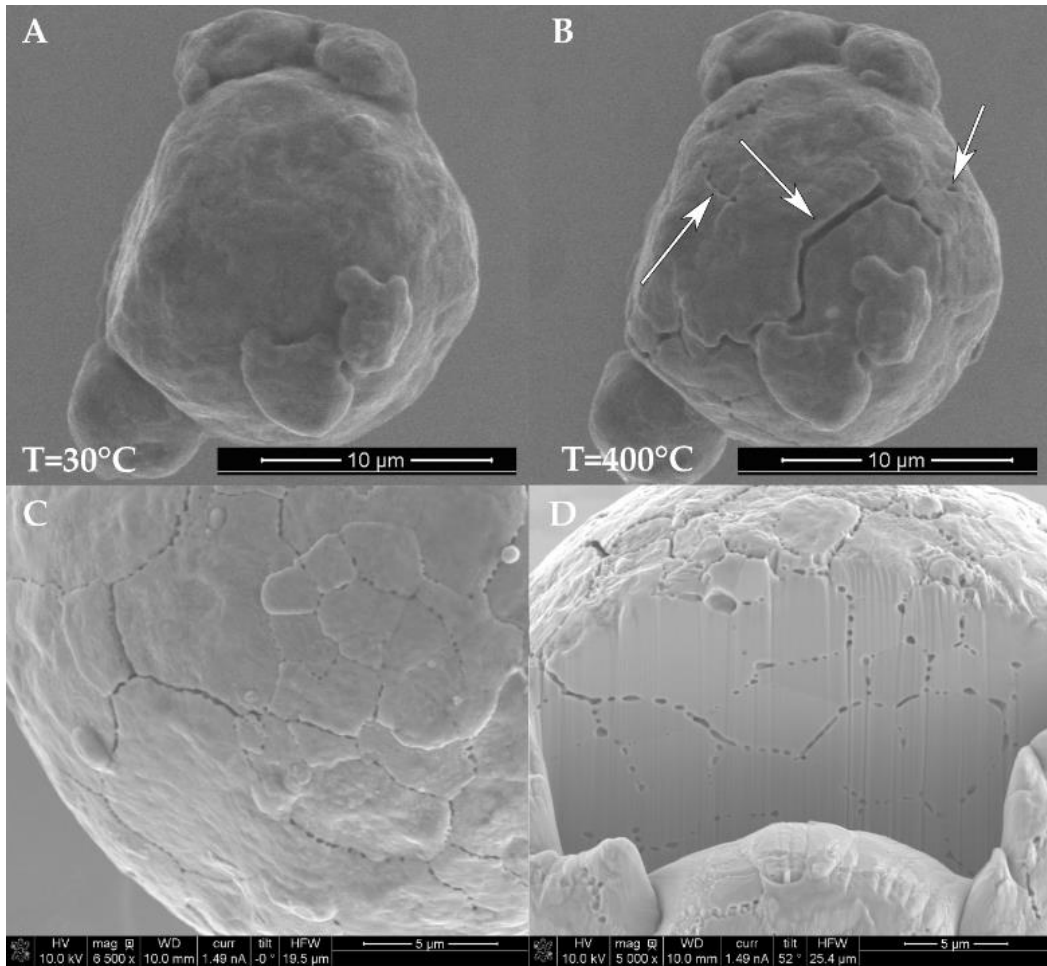


Figure 11. Scanning electron micrographs of a HO-Cu particle after hydrogen treatment, before (**A**) and after (**B–D**) in-situ SEM heating on a SiC chip to 400 °C at 100 °C/s under a vacuum.

3.3.2. Electron Beam Fabrication

EBM involves the selective melting of an elevated temperature powder bed for part fabrication. In this study, the 270°C powder bed temperature for part fabrication in copper is below the critical temperature for H₂O release in hydrogen-treated powder. The reported powder bed temperatures for the EB-PBF of copper range from 380°C (Lodes et al. [8]) to 530°C (Guschlbauer et al. [9]), with oxygen contents comparable to the MO-Cu used in this study (although with a

larger powder size distribution). It was observed early in the development of this study that the removal of surface oxides with hydrogen heat treatment resulted in difficulty in spreading the powder at elevated powder-bed temperatures (>350 °C). Without the presence of surface oxides, the activation energy for sintering is greatly reduced. In some cases, sintering was observed during spreading, resulting in homogenous and uneven layering. A lower powder bed temperature alleviates this problem to some extent, and, from a practical standpoint, facilitates the removal of powder from closed cavities. Unlike other common materials utilized in EB-PBF (e.g., Ti6Al4V, TiAl, and 718), copper powder is less susceptible to charge-induced scattering, because of its high conductivity, which also enables EB-PBF processing at lower temperatures, with minimal sintering.

The single melt track width experiments, described in Section 2.5, were carried out to determine whether the powder adjacent to the melt-pool front reaches a sufficiently high temperature for a sufficiently long duration, in order to induce the powder cracking H₂O vapor release mechanism observed in the heated stage experiments. The thermal input conditions were modeled using the 3D transient heat transfer model developed by Lee et al. [41] at the Oak Ridge National Laboratory, to guide the experimental design. A 2D contour plot of the temperature profile during melting with a 2000 μm hatch spacing is shown in Figure 12. The heat affected zone in the powder bed surrounding the melt pool extends several hundred microns below and to the sides of the melt pool, ranging from 500 °C at 150 μm from the center of the melt pool, to 350 °C at a distance of 250 μm.

The powder samples were harvested from between each of the EB-PBF wafers from the edge/wall wafers and in ~0.1 mm increments so as to determine the influence of the heat affected zone of the melt pool on the surrounding powder bed particles. Figures 12A–C are the SEM images

of the sintered powder adhered to the fabricated part (Figure 12A), ~0.1 mm distance (Figure 12B) and ~0.3 mm distance (Figure 12C) from the part where the surface characteristics of the particles correlate to their respective associated temperature. The sintered powder at the edge of the melt pool was estimated to reach temperatures of 700 °C, where the subsurface H₂O is expected to be expelled from the grain boundaries, and the particle surface is smoothed due to diffusion at these relatively high temperatures. Powder images at 0.1 mm from the edge of the wall experienced temperatures of approximately 400–500 °C, according to the thermal model, and had features similar to the in-situ SEM heating (Figure 11), where obvious grain boundary cracking occurred, but no surface smoothing was visible. The collected powder imaged at 0.3–0.5 mm from the melt pool showed no obvious surface changes because of the relatively low temperature (<350 °C) estimated by the thermal model, and still contained the characteristic H₂O vapor pores. These data support the hypothesis that H₂O is released in the heat affected zone ahead of the melt pool in EB-PBF.

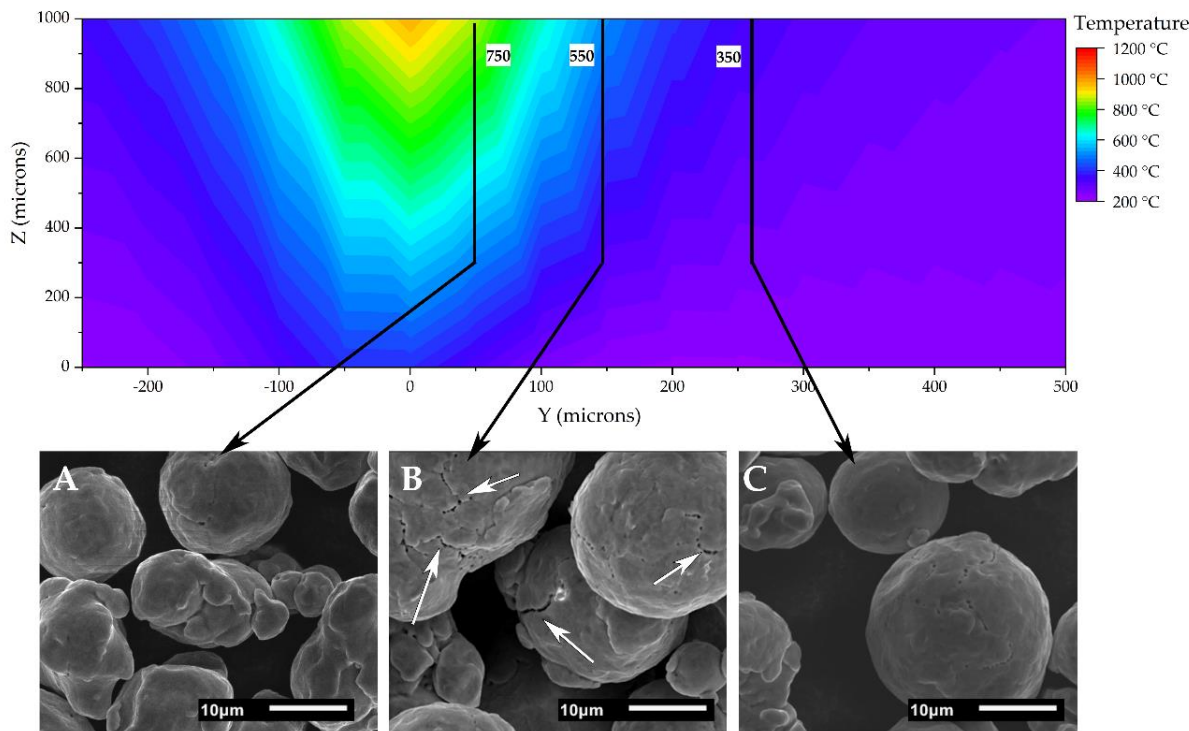


Figure 12. Contour plot of the temperature profile in the XZ plane during melting, with a 2000 μm hatch spacing, showing SEM images of particles located at the edge/wall (**A**), $\sim 0.1 \text{ mm}$ (**B**), and $\sim 0.3\text{--}0.5 \text{ mm}$ (**C**) from the wafer.

To determine the extent at which H_2O is released from hydrogen-treated copper powders during melting as a function of the initial oxygen content, single layer discs were fabricated from each of the treated and untreated powder conditions. Figure 13A shows an image of the melted wafers on the OFE copper fixture after removal from the EB-PBF system. Figure 13C shows an optical image of the surface of the hydrogen-treated LO-Cu melted disc, which exhibits a uniform surface texture with evenly spaced melt pools. However, a non-uniform surface texture is observed on the hydrogen-treated HO-Cu melted disc, where exposed powder can be seen in circular pores on the surface (Figure 13B). The oxygen and hydrogen content of the starting powder, and the resulting solid discs are tabulated in Figure 13D for the treated powders. The untreated powders

showed no change in oxygen content. A minimal change in the oxygen content was detected in the treated LO-Cu solid discs from the starting powder. However, the MO-Cu and HO-Cu solid discs show an approximately 50% reduction in the oxygen content from the starting powder. In both cases, a reduction in the hydrogen content is also observed as being approximately proportional to the amount of reduction in the oxygen content.

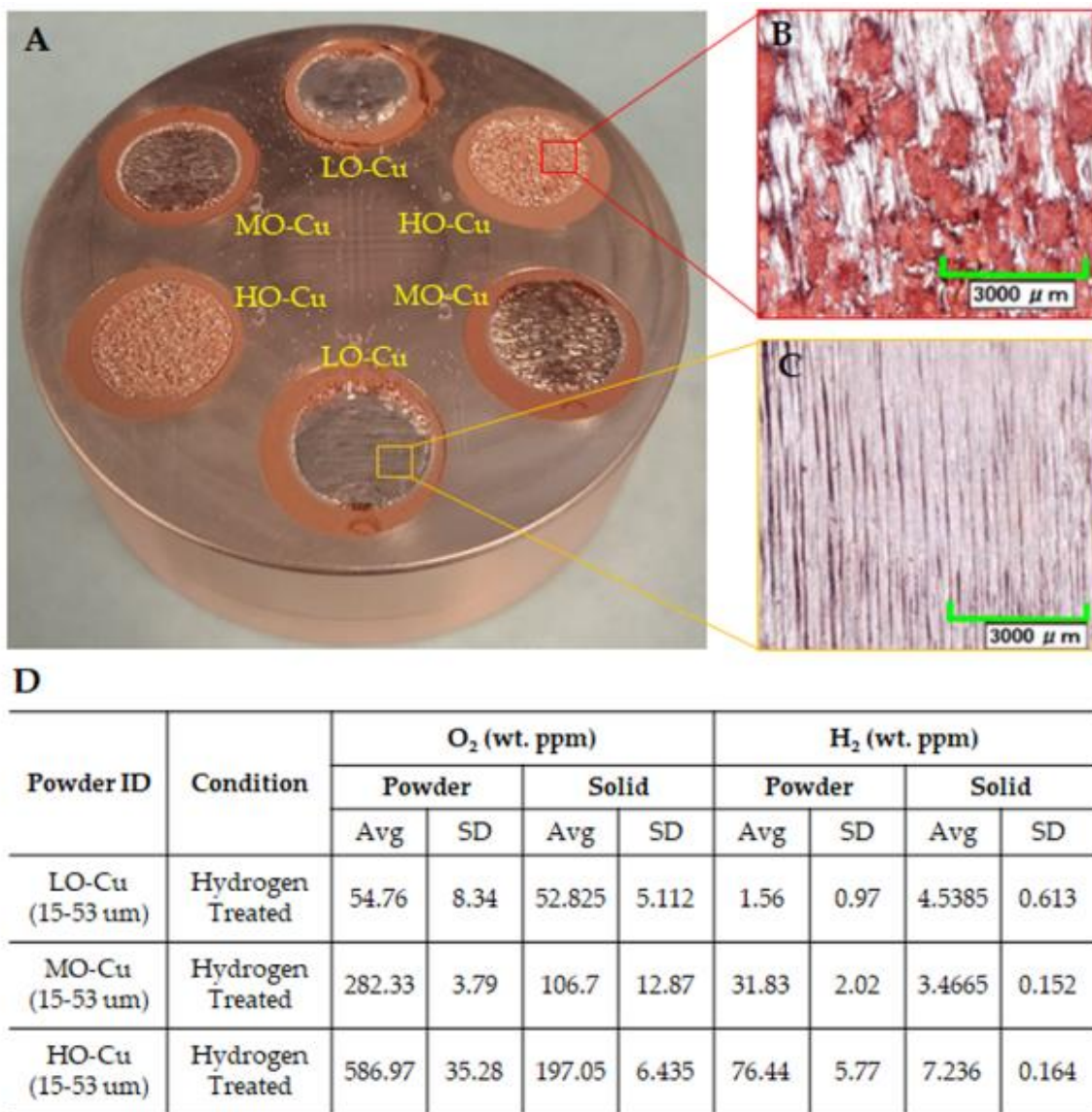


Figure 13. Photograph showing the oxygen free electronic (OFE) copper fixture after EB-PBF of single layer discs on top of hydrogen-treated powder cakes (**A**). Optical microscope images of the surface of single layer disc produced with hydrogen-treated HO-Cu showing pitting and porosity (**B**), and surface of single layer disc produced with hydrogen-treated LO-Cu, showing a smooth surface texture (**C**). Tabulated oxygen and hydrogen contents of the precursor powders and the solid single layer discs for each treated powder condition (**D**).

The residual gas analysis was measured as a function of time during the EB-PBF of HO-Cu, MO-Cu, and LO-Cu single layer discs, and is shown in Figure 14. Each disc was melted as a single step and the H₂O partial pressure was allowed to stabilize before moving to the next step. The HO-Cu and MO-Cu powders show an increase in partial pressure of the H₂O vapor during the melting of the disc with the intensity of the peak being indicative of the relative amount of hydrogen in the powder, as seen in Table 1. The peaks gradually diminish as the H₂O vapor is removed from the system via the vacuum pumps. A minimal peak is witnessed during melting for the LO-Cu powder because of the absence of appreciable H₂O vapor trapped in the particles.

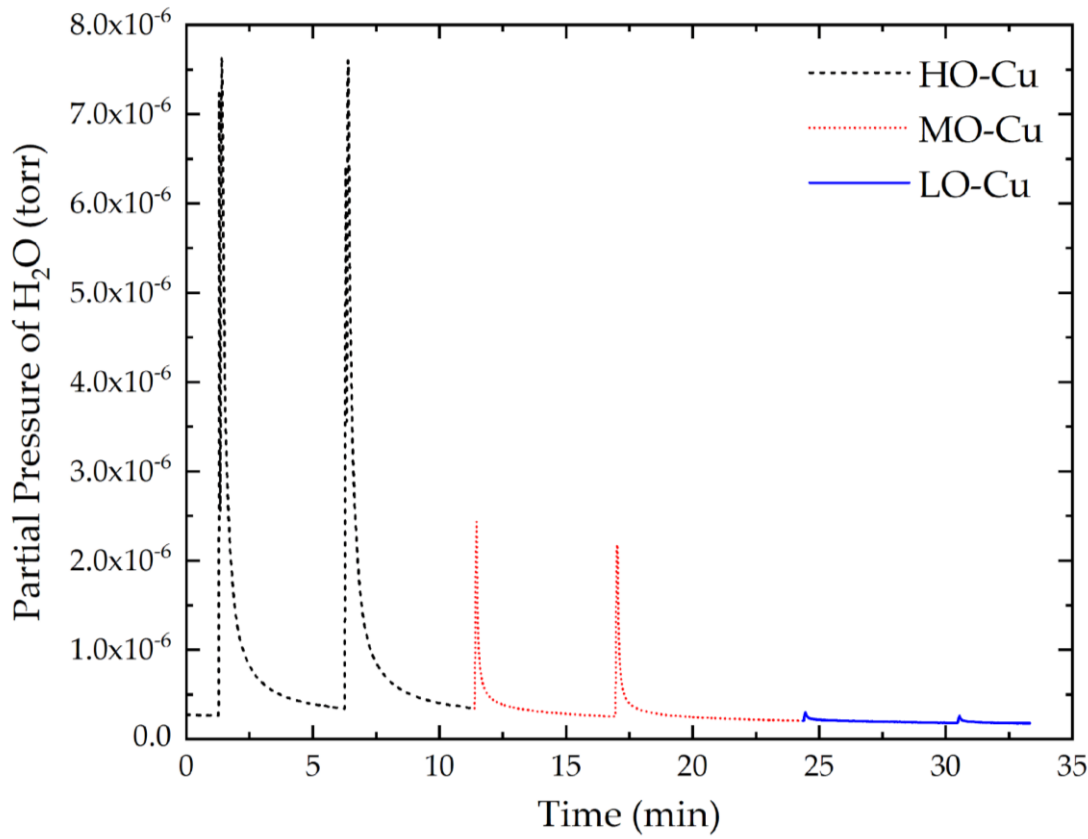


Figure 14. Residual gas analysis of HO-Cu, MO-Cu, and LO-Cu powder during the electron beam powder bed fusion (EB-PBF) of single layer discs.

The presence of porosity on the surface of the discs produced from hydrogen-treated HO-Cu and MO-Cu powder is indicative of excessive spatter, and suggests that a portion of the H₂O vapor escapes from the liquid copper, in addition to the cracking mechanism observed in both the EB-PBF wafer tests and the heated stage experiments. To examine this possibility, high speed imaging (30 kfps) was conducted during the melting process. Full videos are included as part of the supplemental data in this report. Selected frames of high-speed footage of the EB-PBF of hydrogen-treated LO-Cu powder (Figure 15) show a relatively stable melt pool with minimal spatter. However, Figure 16 shows selected frames from the high-speed footage of hydrogen treated HO-Cu particles during melting, and in this case, significant spatter is observed, caused by the escape of H₂O vapor and the expansion in the molten copper. Large bubbles, on the order of 1–2 mm in diameter, are observed expanding and collapsing from liquid copper several mm behind the EB spot. Figure 16B shows a bubble forming in the molten pool, which then collapses and ejects molten metal from the pool shown, in Figure 16C (indicated by arrows).

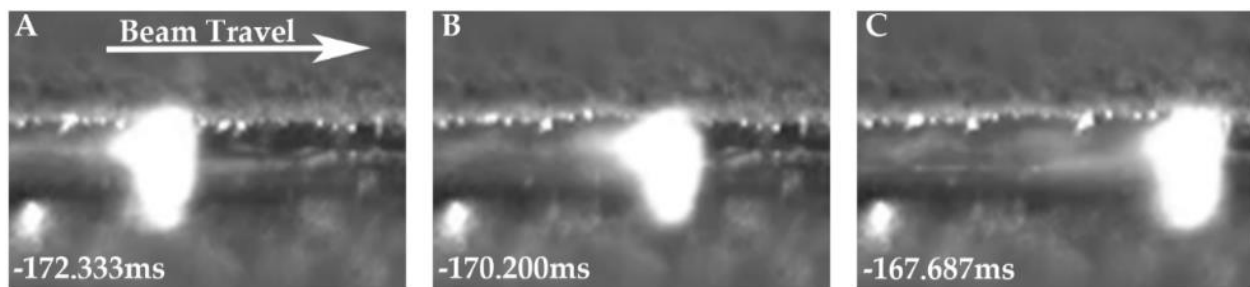


Figure 15. Representative frames of high-speed video footage showing the EB-PBF of a single layer disc on hydrogen-treated LO-Cu powder at timestamps -172.333 ms (**A**), -170.200 ms (**B**), -167.687 ms (**C**).

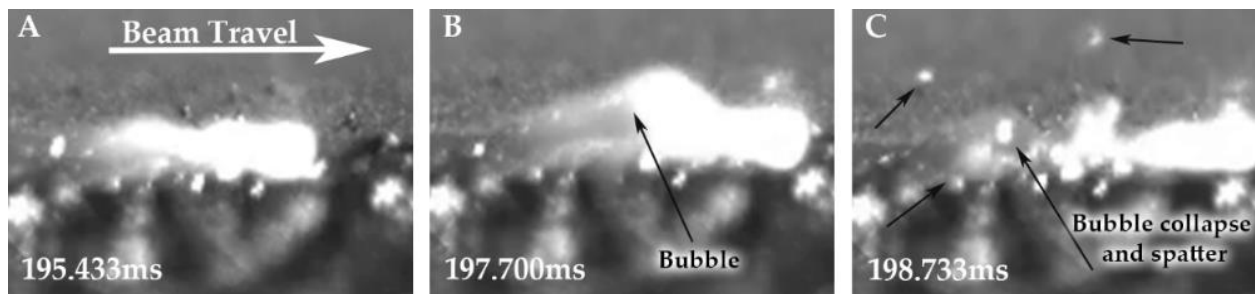


Figure 16. Representative frames of high-speed video footage showing the EB-PBF of a single layer disc on hydrogen-treated HO-Cu powder at timestamps 195.433 ms (A), 197.700 ms (B), 198.733 ms (C).

Despite the presence of porosity in the single layer melt scenario caused by the escape of H₂O vapor from the liquid zone, it was speculated that the layerwise remelting of a material typical in additive manufacturing would serve to reduce or eliminate this porosity in the fabrication of components. In order to determine the effect of successive melts on the removal of H₂O, as well as the solid sample density, cylinders were fabricated using hydrogen-treated MO-Cu powder.

In the EB-PBF validation runs, the precursor untreated powders had an oxygen content of ~450 ppm and a hydrogen content of ~2 ppm, and the solid copper components fabricated with untreated powder show no change in the oxygen content. Hydrogen heat treatment of the MO-Cu powder reduces the oxygen content to ~280 ppm because of the volumetric elimination of surface oxides, and additionally, the hydrogen content of the powder is increased to ~33 ppm. Solid samples fabricated with EB-PBF using hydrogen-treated MO-Cu powder results in an oxygen content of ~50 ppm, and a negligible hydrogen content. The in-situ RGA during both trials shows the partial pressure of the layerwise outgassing of H₂O vapor, which while present on all AM powders, is two orders of magnitude higher for the treated powders compared with the

untreated powders. These data are reported in Figure 17. Figure 18 shows the representative microstructures of the solid samples produced with both treated and untreated powders. In both cases, a columnar grain structure is observed, aligned with the build direction, and a high density is achieved.

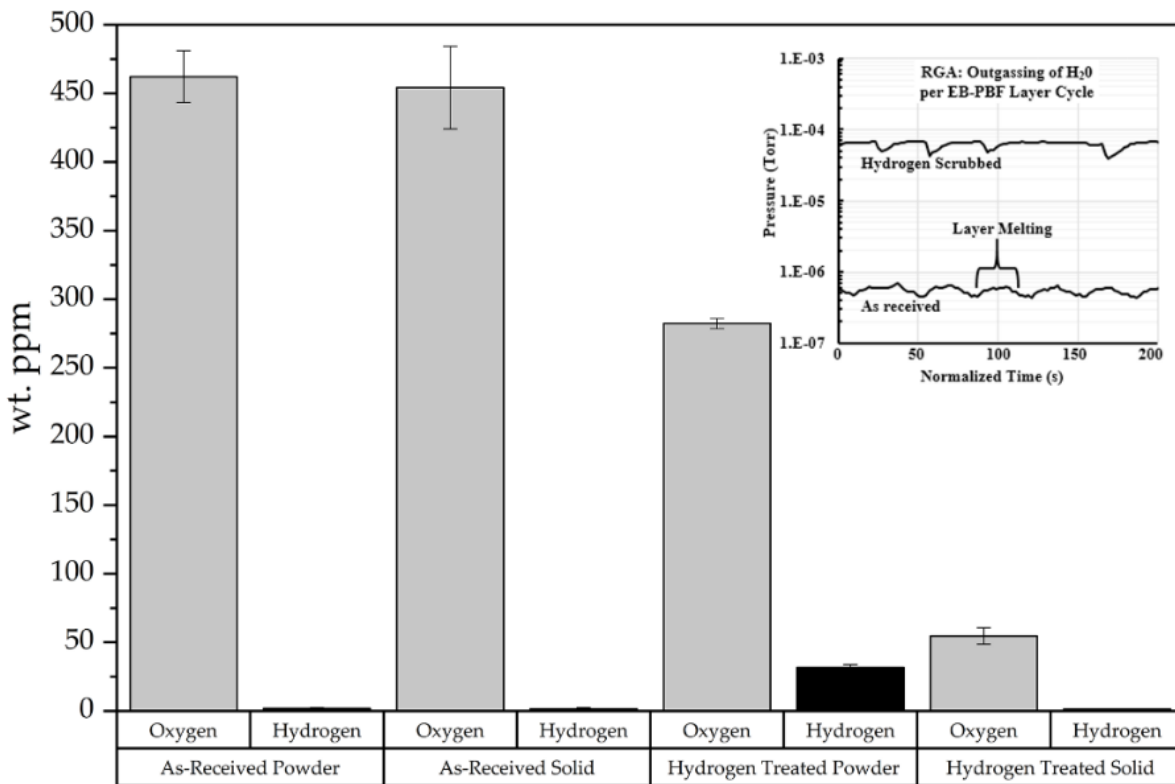


Figure 17. Oxygen and hydrogen content of precursor powders and solid copper cylinders produced with the EB-PBF of untreated and hydrogen-treated MO-Cu powder, and (inset) in-situ residual gas analysis of both EB-PBF runs, showing the layerwise outgassing of H₂O.

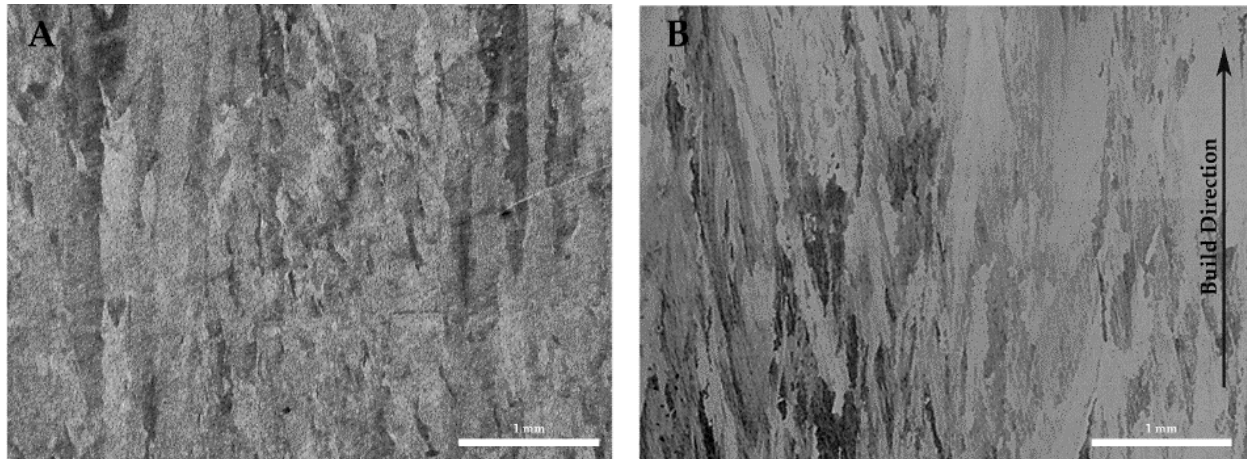


Figure 18. Optical micrographs showing polished and etched microstructures of copper samples fabricated with EB-PBF using hydrogen heat-treated MO-Cu powder (**A**) and untreated MO-Cu powder (**B**). The build direction for both samples are indicated by the arrow in **B**.

3.4. Discussion

The oxygen content of each of the three starting powder conditions results from surface oxide films and oxides along the grain boundaries. The copper oxide will continue to grow when exposed to oxygen, as it does not passivate [42]. The surface oxide thickness as a function of time at room temperature was empirically derived by White and Germer [43]. A typical oxide thickness would fall between 3–5 nm, but could be much thicker. The overall contribution of this oxide layer becomes a significant portion of the chemistry for a powder with a high specific surface area [44]. Figure 19 shows the calculated wt. ppm of oxygen as a function of the particle diameter for cuprous oxide surface films of various thicknesses. In the case of a 5 nm coating, and a typical Gaussian powder size distribution centered at a 35 μm diameter, the oxygen content is estimated to be roughly 75 wt. ppm oxygen, assuming all oxygen neglecting the 2 wt. ppm in solid solution at room temperature [39]. The experimental data gathered in this study suggest that the oxide

thickness on the LO-Cu particles used in this study is ~15–20 nm, consistent with our STEM observations. Volumetrically, this accounts for the measured 200 wt. ppm oxygen, which was mainly surface oxides in the LO-Cu material for particles in the range 15–53 μm .

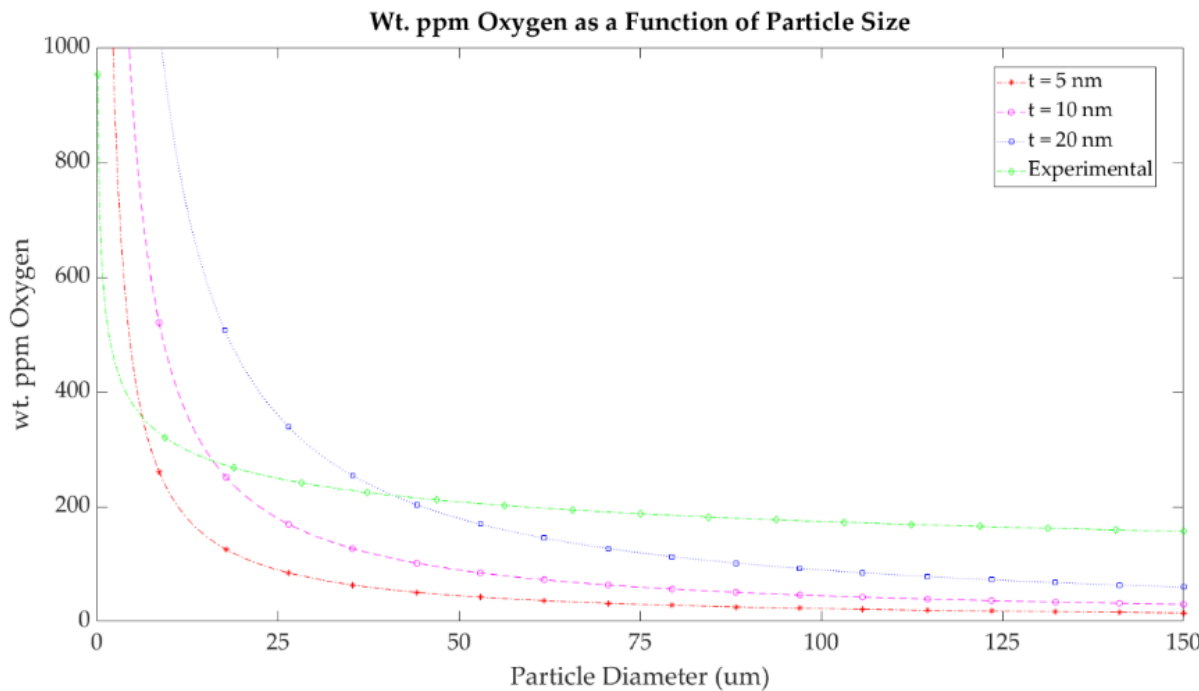


Figure 19. Wt. ppm oxygen as a function of the particle size, assuming a 5 nm cuprous oxide film.

The MO-Cu and HO-Cu particles greatly exceed this oxygen content and show a large number of submicron oxides along the grain boundaries, as seen in Figure 7B and Figure 7C. Naturally, the HO-Cu particles show the largest number of submicron oxides along the grain boundaries, with several larger oxides at triple points of the microstructure because of its exposure to air at elevated temperatures.

To remove the oxide particles, a hydrogen atmosphere heat treatment is employed to reduce the copper oxide to copper and H_2O . This was first observed in the MO-Cu powder in Figure 7C

and Figure 7D, where the surface oxides were removed by hydrogen treatment. As hydrogen diffuses rapidly in copper ($900 \mu\text{m}^2/\text{s}$ at 400°C [34]), it allows for the reduction of oxides present inside the particles in a relatively short amount of time. The hydrogen treatment temperature and time was chosen to allow for sufficient hydrogen diffusion through the particles, while not reaching sintering temperatures for the fine powder size distribution. Although not directly reported herein, it is worth noting that, not since the completion of this study, we have subsequently demonstrated the hydrogen reduction of copper powder in several furnace types (including batch and continuous) in both pure hydrogen and in forming gas (5% h, 95% Ar), and we have observed consistent results in all scenarios for the equivalent treatment times. After hydrogen treatment, the MO-Cu and HO-Cu powders exhibit a micron scale porosity at the triple points of the grain boundaries, and a smaller submicron porosity along the grain boundaries. These pores have previously been shown in the literature to be trapped H_2O vapor [28,30,35].

According to Ito and Hayashi [35], the formation of H_2O vapor in closed pores is as a result of the reduction of copper oxide during hydrogen heat treatment. The H_2O vapor pressure inside a closed pore is higher than that of the surface stress of the pore, which inhibits the pore from collapsing. However, the H_2O vapor pressure is not great enough to overcome the mechanical strength of the grain boundaries of the particle at room temperature.

At around 350°C , the strength of the copper is significantly reduced, and the increasing internal pressure of the H_2O vapor overcomes the mechanical strength of the grain boundary and the pore begins to expand in size. This leads to the fracturing of the particle, seen as an extensive network of interconnected pores along the grain boundaries, and a release of H_2O vapor into the vacuum system, as seen in the SEM images in Figure 11C and Figure 11D, and the RGA data from Figure 14. Notably, our work is presented for a given size distribution of gas atomized powder.

While it is apparent that the reduction of internal Cu₂O and the formation of steam pores is, for all intents and purposes, independent of particle size (owing to the rapid diffusion of hydrogen in copper at 400 °C), the practical upper and lower limits on particle size, for which the observed phenomena hold true, is not clear from this research. It is likely that the combined influences of grain boundary strength, grain size, radius of curvature, and oxygen content will contribute to the steam embrittlement/fracture mechanism in different ways.

The observations shown here suggest that H₂O is released by two mechanisms during EB-PBF. A chemical analysis of the sintered powder bed shows a similar oxygen and hydrogen content as the starting powder, as seen in Table 1, and suggests that the H₂O vapor is not released during the preheating step, which is measured in the range of 250–270 °C. While not explored in this study, it is anticipated that higher preheat temperatures, similar to those used by Frigola [1] and Guschlbauer [9], would be sufficiently high to elicit the effect observed by the TGA and heated stage SEM experiments. In the present case, the simulation results and experiments of a single electron beam melt line in a copper powder bed show that as the electron beam scans across the sample during the melting step, the highly localized heat in front and to the sides of the beam causes the particles in the heat affected zone to fracture because of the H₂O vapor expansion at 400 °C. The scanning electron microscopy of the particles surrounding the single wafer tracks show fracture surfaces similar to that of Figure 11C.

The chemical analyses of the single layer melt solid discs of MO-Cu and HO-Cu show that some amount of H₂O vapor is trapped during the solidification of the melt pool, as seen in Figure 14. We theorize that as the particles become molten, the volume of the H₂O vapor rapidly expands because of the significant pressure drop due to the vacuum environment, and become bubbles of H₂O vapor in the melt pool. According to Boyle's law, a pressure of 5.7 MPa confined to a sphere

with a diameter of 1 um will expand to a sphere with a diameter of 1 mm at a pressure of $5 \times e^{-9}$ MPa. This is approximately a 10^9 increase in the volume of the trapped H₂O vapor from within a closed pore. The H₂O vapor bubbles are able to escape the melt pool, which is evident in the decrease in oxygen and hydrogen content of the single melt layer discs. However, because of the rapid solidification of the melt pool (10^{-4} to 10^{-6} °C/s) and the high viscosity of molten copper, and the large amount of spatter associated with bubble collapse, a portion of these H₂O vapor bubbles may become trapped in the solid single layer discs as pores. An observation of the multiple layer build validation runs suggest that these pores are largely eliminated by the subsequent remelting of the previous layers, which allows repeated opportunities for the H₂O vapor to escape to the surface. This is in stark contrast to the traditional copper processing routes (powder metal, sintering, annealing etc.) for which oxygen containing copper powder exposed to a high temperature hydrogen atmosphere results in deleterious embrittlement, cracking, swelling, and porosity. This is clearly shown in the density and microstructures of Figure 18. Also evident is an apparent difference in grain size. This was not investigated in this study, but it is reasonable that the differences in oxygen content and the turbulent liquid pool/spatter brought about by the escape of water vapor during solidification could lead to the disruption of grain growth observed. Further analyses would be required in order to verify this hypothesis.

While the present study has focused on the EB-PBF processing of copper, it is entirely plausible that a comparable methodology could be repeated for the LPBF processes. However, the poor absorptivity, lower ambient temperatures, and lack of a vacuum atmosphere may contribute to a significantly different outcome. In the work by El-Wardany et al. [6], a relatively high oxygen copper powder was heat treated in a forming gas environment in order to remove the surface oxides and subsequently be coated with a polydimethylsiloxane (PDMS) polymer. No further data on the

chemistry, properties, or microstructure of this material were reported, other than the observation of the formation of unexpectedly large pores in single track welds that were not present in the untreated powders. These results, and the results of the current study suggest that further research is warranted, which also accounts for the potentially important effects of chamber atmosphere and the partial pressures of the relevant gas species during the AM processing of copper.

3.5. Conclusions

By utilizing a hydrogen furnace treatment to reduce the oxygen content of atomized copper powder feedstock for use in EBM processing, we have shown the ability to produce pure copper parts with a lower oxygen content than that of the initial feedstock. Depending on the initial oxygen content, the mechanism for reduction shifts from the removal of surface oxides of a low starting oxygen content, to a combination of surface oxide removal and internal H₂O vapor formation as the starting oxygen content increases. The release of internally trapped H₂O vapor is shown to occur in the heat affected zone to the front and side of the melt pool, in addition to release from the melt pool. Successive remelting allows sufficient time for H₂O removal from hydrogen-treated powder, to produce solids resulting in an oxygen content of 50 wt. ppm.

3.6 References

1. Frigola, P.; Harrysson, O.L.A.; Horn, T.J.; West, H.; Aman, R.; Rigsbee, J.M.; Ramirez, D.A.; Murr, L.; Medina, F.; Wicker, R.B.; et al. Fabricating Copper Components. *Adv. Mater. Process.* **2014**, *172*, 20–24.
2. Gamzina, D.; Kozina, M.; Mehta, A.; Nanni, E.; Tantawi, S.; Welander, P.; Horn, T.; Ledford, C. Copper Reconsidered: Material Innovations to Transform Vacuum Electronics. In Proceedings of the 2019 International Vacuum Electronics Conference (IVEC), Busan, Korea, 29 April–1 May 2019; pp. 1–2.
3. Gamzina, D.; Luhmann, N.C.; Ledford, C.; Horn, T.; Karakaut, I.; Lin, L.; Frigola, P. Additive vacuum electronics: Electron beam melting of copper. In Proceedings of the 2017 Eighteenth International Vacuum Electronics Conference (IVEC), London, UK, 24–26 April 2017; pp. 1–2.
4. Horn, T.; Karakaut, I.; Ledford, C.; Gonzalez, M.; Gamzina, D.; Luhmann, N.C.; Lin, L. Additively manufactured WR-10 copper waveguide. In Proceedings of the 2018 IEEE International Vacuum Electronics Conference (IVEC), Monterey, CA, USA, 24–26 April 2018; pp. 409–410.
5. Ives, R.L. Additive Manufacturing of Klystrons. In Proceedings of the 2018 Nineteenth International Vacuum Electronics Conference (IVEC), Monterey, CA, USA, 24 April 2018.
6. El-Wardany, T.I.; She, Y.; Jagdale, V.N.; Garofano, J.K.; Liou, J.J.; Schmidt, W.R. Challenges in Three-Dimensional Printing of High-Conductivity Copper. *ASME J. Electron. Packag.* **2018**, *140*, 020907.

7. Raab, S.J.; Guschlbauer, R.; Lodes, M.A.; Körner, C. Thermal and Electrical Conductivity of 99.9% Pure Copper Processed via Selective Electron Beam Melting. *Adv. Eng. Mater.* **2016**, *18*, 1661–1666.
8. Lodes, M.A.; Guschlbauer, R.; Körner, C. Process development for the manufacturing of 99.94% pure copper via selective electron beam melting. *Mater. Lett.* **2015**, *143*, 298–301.
9. Guschlbauer, R.; Momeni, S.; Osmanlic, F.; Körner, C. Process development of 99.95% pure copper processed via selective electron beam melting and its mechanical and physical properties. *Mater. Charact.* **2018**, *143*, 163–170.
10. Ramirez, D.A.; Murr, L.E.; Li, S.J.; Tian, Y.X.; Martinez, E.; Martinez, J.L.; Machado, B.I.; Gaytan, S.M.; Medina, F.; Wicker, R.B. Open-cellular copper structures fabricated by additive manufacturing using electron beam melting. *Mater. Sci. Eng. A* **2011**, *528*, 16–17.
11. Ramirez, D.A.; Murr, L.E.; Martinez, E.; Hernandez, D.H.; Martinez, J.L.; Machado, B.I.; Medina, F.; Frigola, P.; Wicker, R.B. Novel precipitate–microstructural architecture developed in the fabrication of solid copper components by additive manufacturing using electron beam melting. *Acta Mater.* **2011**, *59*, 4088–4099.
12. Bala, K.; Pradhan, P.R.; Saxena, N.S.; Saksena, M.P. Effective thermal conductivity of copper powders. *J. Phys.*
13. Smith, C.J.; Tammas-williams, S.; Hernandez-nava, E.; Todd, I. Tailoring the thermal conductivity of the powder bed in Electron Beam Melting (EBM) Additive Manufacturing. *Sci. Rep. Nat. Publ. Group Lond.* **2017**, *7*, 1–8.

14. Wei, L.C.; Ehrlich, L.E.; Powell-Palm, M.J.; Montgomery, C.; Beuth, J.; Malen, J.A. Thermal conductivity of metal powders for powder bed additive manufacturing. *Addit. Manuf.* **2018**, *21*, 201–208.
15. Martin, A.A.; Calta, N.P.; Hammons, J.A.; Khairallah, S.A.; Nielsen, M.H.; Shuttlesworth, R.M.; Sinclair, N.; Matthews, M.J.; Je_ries, J.R.; Willey, T.M. Ultrafast dynamics of laser-metal interactions in additive manufacturing alloys captured by in situ X-ray imaging. *Mater. Today Adv.* **2019**, *1*, 100002.
16. Mahamood, R.M. (Ed.) Laser Basics and Laser Material Interactions. In *Laser Metal. Deposition Process. of Metals, Alloys, and Composite Materials*; Springer International Publishing: Cham, Switzerland, 2018; pp. 11–35.
17. Colopi, M.; Caprio, L.; Demir, A.G.; Previtali, B. Selective laser melting of pure Cu with a 1kW single mode fiber laser. *Procedia CIRP* **2018**, *74*, 59–63.
18. Constantin, L.; Fan, L.; Mortaigne, B.; Keramatnejad, K.; Zou, Q.; Azina, C.; Lu, Y.F.; Silvain, J.-F. Laser sintering of cold-pressed Cu powder without binder use. *Materialia* **2018**, *3*, 178–181.
19. Ikeshoji, T.-T.; Nakamura, K.; Yonehara, M.; Imai, K.; Kyogoku, H. Selective Laser Melting of Pure Copper. *JOM* **2018**, *70*, 396–400.
20. Kaden, L.; Matthäus, G.; Ullsperger, T.; Engelhardt, H.; Rettenmayr, M.; Tünnermann, A.; Nolte, S. Selective laser melting of copper using ultrashort laser pulses. *Appl. Phys. A* **2017**, *123*, 596.
21. Lykov, P.; Safonov, E.V.; Akhmedianov, A. Selective Laser Melting of Copper. *Mater. Sci. Forum* **2016**, *843*, 284–288.

22. Trevisan, F.; Calignano, F.; Lorusso, M.; Lombardi, M.; Manfredi, D.; Fino, P. Selective Laser Melting of Chemical Pure Copper. In Proceedings of the Euro PM 2017 Congress & Exhibition, Milan, Italy, 1–5 October 2017.
23. Zhong, H.Z.; Li, C.G.; Zhang, X.Y.; Gu, J.F. The graded microstructures evolving with thermal cycles in pure copper processed by laser metal deposition. *Mater. Lett.* **2018**, 230, 215–218.
24. Davis, J.R. *Copper and Copper Alloys*; ASM International: Cleveland, OH, USA, 2001.
25. Andrews, P.V.; West, M.B.; Robeson, C.R. The effect of grain boundaries on the electrical resistivity of polycrystalline copper and aluminium. *Philos. Mag. J. Theor. Exp. Appl. Phys.* **1969**, 19, 887–898.
26. Heuer, R.P. The Effect of Iron And Oxygen on the Electrical Conductivity of Copper. *J. Am. Chem. Soc.* **1927**, 49, 2711–2720.
27. Belkin, E.; Nagata, P.K. Hydrogen Embrittlement of Tough Pitch Copper by Brazing. *Weld. Res. Suppl.* **1975**, 54–62.
28. Ward, T.G.; Nix,W.D. The formation of water vapor bubbles in copper and their effect on intergranular creep fracture. *Acta Metall.* **1980**, 28, 557–566.
29. Hallstedt, B.; Risold, D.; Gauckler, L.J. Thermodynamic assessment of the copper-oxygen system. *J. Phase Equilibria* **1994**, 15, 483–499.
30. Nieh, T.G.; Nix, W.D. Embrittlement of copper due to segregation of oxygen to grain boundaries. *Metall. Trans. A* **1981**, 12, 893–901.
31. Goldstein, E.A.; Mitchell, R.E. Chemical kinetics of copper oxide reduction with carbon monoxide. *Proc. Combust. Inst.* **2011**, 33, 2803–2810.

32. Poulston, S.; Parlett, P.M.; Stone, P.; Bowker, M. Surface Oxidation and Reduction of CuO and Cu₂O Studied Using XPS and XAES. *Surf. Interface Anal.* **1996**, *24*, 811–820.
33. Ren, D.; Deng, Y.; Handoko, A.D.; Chen, C.S.; Malkhandi, S.; Ye, B.S. Selective Electrochemical Reduction of Carbon Dioxide to Ethylene and Ethanol on Copper(I) Oxide Catalysts. *ACS Catal.* **2015**, *5*, 2814–2821.
34. Magnusson, H.; Frisk, K. Diffusion, Permeation and Solubility of Hydrogen in Copper. *J. Phase Equilibria Diffus.* **1993**, *38*, 65–69.
35. Ito, H.; Hayashi, K. Detection of Gases in Closed Pores of Incompletely Densified Copper Sintering. In Proceedings of the 1993 Powder Metall., Kyoto, Japan, 12–15 July 1993.
36. Lin, Y.-J.; Hwang, K.-S. Swelling of Copper Powders during Sintering of Heat Pipes in Hydrogen-Containing Atmospheres. *Mater. Trans.* **2010**, *51*, 2251–2258.
37. Collet, R.; le Gallet, S.; Charlot, F.; Lay, S.; Chaix, J.M.; Bernard, F. Oxide reduction effects in SPS processing of Cu atomized powder containing oxide inclusions. *Mater. Chem. Phys.* **2016**, *173*, 498–507.
38. Louthan, M.R.; Caskey, G.R.; Donovan, J.A.; Rawl, D.E. Hydrogen embrittlement of metals. *Mater. Sci. Eng.* **1972**, *10*, 357–368.
39. Magnusson, H.; Frisk, K. Self-Diffusion and Impurity Diffusion of Hydrogen, Oxygen, Sulphur and Phosphorus in Copper; Swerea KIMAB AB: Stockholm, Sweden, December 2013; p. 33.
40. Murr, L.E.; Gaytan, S.M.; Ramirez, D.A.; Martinez, E.; Hernandez, J.; Amato, K.N.; Shindo, P.W.; Medina, F.R.; Wicker, R.B. Metal Fabrication by Additive Manufacturing

Using Laser and Electron Beam Melting Technologies. *J. Mater. Sci. Technol.* **2012**, *28*, 1–14.

41. Lee, Y.S.; Kirka, M.M.; Raghavan, N.; Deho_, R.R. Simulation of Spot Melting Scan Strategy to Predict Columnar to Equiaxed Transition in Metal Additive Manufacturing. In Proceedings of the International Solid Freeform Fabrication Symposium, Austin, TX, USA, 7–9 August 2017; p. 13.
42. Lee, S.-K.; Hsu, H.-C.; Tuan,W.-H. Oxidation Behavior of Copper at a Temperature below 300C and the Methodology for Passivation. *Mater. Res.* **2016**, *19*, 51–56.
43. White, A.H.; Germer, L.H. The Rate of Oxidation of Copper at Room Temperature. *Trans. Electrochem. Soc.* **1942**, *81*, 305–319.
44. Zhou, Y.; Liu, J.; Liang, D.; Shi,W.; Yang,W.; Zhou, J. E_ect of particle size and oxygen content on ignition and combustion of aluminum particles. *Chin. J. Aeronaut.* **2017**, *30*, 1835–1843.

CHAPTER 4: Real Time Monitoring of Electron Emissions during Electron Beam Powder Bed Fusion for Arbitrary Geometries and Toolpaths

Christopher Ledford¹, Mouda Tung¹, Chris Rock¹, and Timothy Horn^{1,2}

1) Center for Additive Manufacturing and Logistics, North Carolina State University, 126

Daniels Hall, Raleigh, NC 27695-7906, USA

2) Department of Mechanical and Aerospace Engineering, North Carolina State University,

Campus Box 7910, Raleigh, NC 27695-7910, USA

Abstract:

Real-time monitoring of electron emissions during the operable processing steps of electron beam powder bed fusion (EB-PBF), which typically include preheating, melting, and post-heating, provides a wealth of in-process data across multiple length scales. In this paper, we present a methodology for collecting both real-time beam positional data and electron emissions as a function of time for arbitrary component geometries and complex toolpaths. To demonstrate this, we collected these data during the melting steps of EB-PBF of pure copper and quantitatively compared electron images generated with this approach to both x-ray micro computed tomography (μ CT) data and optical micrographs of the same specimens. These results show a strong mathematical correlation between the location of loss of signal events observed in electron images and observed defects in μ CT. At the same time, the collection of beam positional information facilitates the calculation of beam velocities, and hence local energy inputs. We also demonstrate a methodology to visualize process data from a wide variety of sources and map these over the 3D geometries as a function of time and position and to link these spatiotemporal data to structure observed in the electron imaging and energy input maps.

Ultimately, we have leveraged this new electron imaging approach to defect detection into a rudimentary control strategy to eliminate porosity in a copper sample.

4.1 Introduction

Manufacturing processes that utilize an electron beam as a directed energy source often benefit from enhanced process monitoring and control opportunities. Like scanning electron microscopy, electron interactions lead to a spread of energy over a region larger than the beam diameter [1], and this can provide a wealth of near-instantaneous spatiotemporal process data through the collection of secondary electrons, backscattered electrons, x-rays, photons, and the like. These data, in turn, are processed to measure localized geometric, topographic, and compositional variations over a wide range of process temperatures, conditions, and length scales.

For decades, monitoring of electron beam artifacts has been utilized in electron beam welding operations for in-situ weld seam monitoring, crack/defect detection, positioning, measurement, and beam diagnostics (focus, profile, etc.), and is often standard equipment on many commercial systems [2-7]. For clarity, while not always denoted consistently in the literature, these sensors typically detect any artifacts that induce a current including, backscattered electrons (BSE), secondary electrons (SE), charged plasma, thermionic emission, etc. and, collectively we refer to these as total electron emissions (TEE). More recently, TEE monitoring has been applied to EB welding-based, directed energy, additive manufacturing (AM) processes [7], but the adoption of this technique as a process monitoring tool for electron beam powder bed fusion (EB-PBF) has lagged significantly. Recent publications have demonstrated that the same principles involved in image generation for scanning electron microscopy are directly applicable to EB-PBF processes. Pobel et al. [7] and Arnold et al.

[10,11] generated images from low current post-layer line scans acquired after the deposition, heating, and melting of each layer using a custom-built EB-PBF platform with a 6kW Pro-beam welding gun with an integrated BSE detector. These studies were carried out using Ti6Al4V with typical operating temperatures and the basic process parameter space commonly associated with that material (~730-750°C, as measured by a thermocouple below the build substrate). They demonstrated the capability to acquire BSE data between layers during the process, generate images, and qualitatively compared the local intensity of these images to defects in the produced samples observed by x-ray micro-computed tomography (μ CT) and optical microscopy. This approach enabled rapid screening and assessment of a given processing space. Later, Wong et al. published a serialized set of experiments evaluating the spatial resolution of a customized electron sensor, data acquisition, and image generation approach installed on a commercial Arcam EB-PBF system [13-17]. In these studies, the standard heat shield was modified and isolated from the vacuum chamber serving as an electron sensor. Images were generated of a prefabricated EB-PBF test geometry or machined benchmarking component placed in the vacuum chamber. This methodology was carried out at both room [13,14] and high (up to 650 °C) [16] temperature. Wang et al. subsequently described a similar sensor and hardware [18]. In a more recent publication, Arnold et al. collected BSE signals during the melting step. They demonstrated an example of data collected from a single layer, with various process parameters using this approach. The authors observed features such as porosity and swelling on the top/final surface of prismatic Ti6Al4V samples and qualitatively compared the same surfaces measured by both laser scanning microscopy and confocal laser scanning microscopy [12]. Given the drive for improved in-situ process monitoring and control capabilities for EB-PBF, monitoring of TEE during the melting step is a particularly attractive approach. While not

previously quantified for AM, the data presented herein suggest a strong correlation of TEE to process defects, but more importantly that such data can be acquired and interpreted in near real-time as a function of beam position. However, efforts have been hindered by difficulties associated with system integration, automation, beam position tracking, beam power monitoring, data acquisition, data processing, and interpretation rather than gaps in the understanding of the physical phenomena at play.

Still, such steps are critical to leveraging the full potential of TEE monitoring in real-world applications. In commercial Arcam EB-PBF systems, the process parameters are controlled by an internal thermal model. Sets of unitless parameters (e.g., speed function, thickness function, turning points function, etc.) are continually adjusting the primary settings (mostly beam scan velocity and beam current) in an attempt to account for variations in part geometry, beam path, build height, overhangs, downward-facing surfaces, and other stochastic thermal boundary conditions. The speed function, which is described in detail by Narra et al. [27] maintains a constant melt pool size by changing beam speed in proportion to beam current. Larger values of the speed function are related to faster speeds (smaller melt pools), and lower values of the speed function are related to slower beam speeds (larger melt pools). The turning points function is a set of parameters that collectively decrease the localized energy input at the edges of the part by increasing the beam speed (accelerating the beam when it reaches the end of a track and turns around). The thickness function is described in detail by Smith et al. [33], and this set of parameters increases the beam speed over downward-facing geometries to account for the change in local thermal conductivity between the solid part and the powder bed. While such parameters are often proprietary, and their effects are not always readily apparent to the user, the objective of this approach is two-fold. First, to maintain a constant surface temperature/constant

heat flux through the powder bed, and second to maintain a constant melt pool size and solidification conditions. The degree to which these objectives are met, and the resulting variability in microstructure and part quality, is the subject of debate and considerable research efforts.

Nevertheless, the inclusion of a post layer scanning step would require a separate process step, which, for the commercial Arcam control system, changes the calculation of the thermal model and fundamentally alters the thermal history experienced by the material, regardless of the timescales involved. The post layer scan time depends on several factors, including the imaging area, beam speed, data-logging rate, and hatch distance. In the reported post-layer imaging approaches by Arnold et al., a customized control system is utilized, and neither the thermal control strategy nor thermal processing conditions were documented. However, given that the geometries reported were typically small, prismatic, and aligned with the beam scan direction, it is unlikely that these influences would manifest in Ti6Al4V. While the studies reported by Wong et al. utilize a commercial Arcam control system, no actual layer-wise processing, or manufacturing of AM parts or samples with the in-situ layerwise monitoring capability was reported.

In all cases, the methodologies presented in the current literature for both melt monitoring and post melt TEE monitoring have relied on rectilinear scan strategies in order to facilitate beam tracking and to calculate a predicted beam position based on the start or end of scan lines (from a deflection coil signal) and the user-defined beam speed. Although not fundamental to the collection of signals or image generation, this limitation is a barrier to the practical applicability of the approach. AM geometries are typically complex; build volumes often consist of dozens of individual components with arbitrary orientations and cross-sections. An EB-PBF

layer consists of multiple process heating and melting steps, melt path orientations, trajectories, and beam multiplexing. Recent work at Oak Ridge National Laboratory has expanded this processing space by leveraging beam multiplexing for complex tool pathing (e.g., spot melting, space-filling, etc.) to manipulate local grain structure and defect formation [19-23]. Process monitoring and control methodologies should, therefore, accommodate variability in crucial process steps leverage AM to its full potential for components exhibiting both extrinsic geometric and intrinsic material complexity.

Building upon the recent work, this research examines the potential of an alternative acquisition methodology and hardware implemented on a commercial Arcam A2 EB-PBF control system. We hypothesize that collecting beam positional data during melting (or any other process step) directly from the system programmable logic controller (PLC), which commands the deflection optics, facilitates several new possibilities for monitoring and control. Through a series of experiments, we both demonstrate and evaluate the advantages and disadvantages of these approaches. First, the positional monitoring approach described herein enables real-time tracking of the TEE signal position regardless of part geometry, beam trajectory or speed. We first demonstrate this for the fabrication of a set of prismatic samples similar to what has been presented by Arnold et al. [12]. However, our approach incorporates varying melt parameters utilizing the Arcam automatic control functions. We then establish the methodology for multiple layers and compare the results to 3D x-ray micro-computed tomography (μ CT) and optical micrographs of the same samples. The TEE signal was normalized against the real-time measured output of the system high voltage beam current feedback to calculate the total electron yield (TEY) to account for variation in the incident beam current from layer to layer. In the current literature, only the user-defined nominal beam current has been utilized.

The procedure reported here inherently encapsulates process-specific data related to variations in beam velocity associated with the system automatic control functions and part geometry by tracking the beam position. These data were, in turn, mapped to calculate localized variations in volumetric energy density and compared to the TEY maps at the same locations. A second set of prismatic specimens were then fabricated to demonstrate the same approach for arched or overhanging bridge structures. In such cases, the Arcam ‘thickness function’ drives an increase in beam velocity to account for the drastic change in thermal conductivity between the solid part and the powder bed. In addition to beam velocity mapping, the described approach has allowed us to map any available spatiotemporal process data over 3D part geometries, and to compare them to the same maps of the TEY data. In order to further explore this approach, a representative, real-world geometry was fabricated utilizing these tools. Finally, we demonstrate the implementation of a rudimentary layer-wise control strategy to minimize porosity in a sample from the same processing space by monitoring the TEY data and adjusting the beam power.

4.2 Methodology:

4.2.1 Instrumentation and Data Acquisition:

Real-time melt monitoring of TEE signals through multiple layers, arbitrary part geometries, and beam trajectories requires three basic inputs from the EB-PBF system; A sensor to collect TEE signals, real-time or *a priori* knowledge of the beam path as a function of time, and real-time monitoring of the input beam current. In the sections below, we describe the methodology that we used to assemble these constituents on a modified Arcam A2 using the standard commercial EB-PBF control system, without interruption to the standard control process. All experiments were carried out using an Arcam A2 electron beam powder bed fusion

system (Control software V3.2 SP2). While the monitoring system has been tested successfully on standard Arcam hardware platforms, the selected Arcam A2 used in this study utilized a custom build platform and powder deposition mechanism for small-batch processing and material/parameter development which are described in detail elsewhere [24, 25].

4.2.2 Multiple Sensor Detector Hardware

The electron monitoring hardware is illustrated in Figure 1: Illustration of the detector hardware mounted inside the EB-PBF vacuum chamber (A) and schematic of the hardware assembly circuit diagram showing the arrangement of the components (B). , which consisted of two detector plates (a left plate and a right plate), a noise plate, and an adaptor mounting plate to affix the assembly within the vacuum chamber. All plates were electrically isolated from the chamber and each other using alumina ceramic bolts and washers as illustrated in Figure 1. The split-plate copper detector assembly measured 220 mm x 220 mm x 3 mm, with a 100 mm hole in the center for the beam to pass through for powder bed processing and part fabrication. The detector plates were attached to the noise plate with four ceramic M6 bolts and separated by ceramic washers. The noise plate, in turn, was a 12.7 mm thick annular copper ring, a 124.5 mm outer diameter, and a 78.7 mm inner diameter and mounted to the adapter base plate with four ceramic M6 bolts, again, separated by ceramic washers. The TEE sensor assembly is situated inside the vacuum chamber below the electron beam column. This provides line of sight access for additional sensors (pyrometer, infrared radiation (IR) camera, optical camera, etc.) mounted to the top of the vacuum chamber to corroborate the TEE data and described in detail by Ledford et al. [25]. In the preliminary portions of this work, we tested a TEE sensor based on the modified heat shield methodology presented by Wong et al. [13], albeit with two isolated plates

instead of just one, with equivalent results. Figure 1 also shows a schematic of the detector circuit. When emitted electrons, regardless of their origin, strike the detector plate(s), a current is induced from ground to the detector plate. By passing this current across a $1\text{ k}\Omega$ shunt resistor and an operational amplifier (LM358P), a voltage potential is generated.

The three circuits required for topographic and compositional data signal generation are also illustrated. The noise plate and detector plates were connected to three current-to-voltage converters outside the vacuum system by means of an ISO KF-40 BNC vacuum feed through (IdealVac P108811), which was installed in an existing port on the Arcam system vacuum chamber. Kapton insulated wires were utilized on the vacuum side of the circuit to avoid degassing.

The voltage converted signals from the right and left detector plates pass through a differential amplifier, LM358P) to produce the topographic mode signal. To generate the compositional mode signal, the voltage converted signal from both plates pass through a summing amplifier followed by a differential amplifier. Then, this voltage potential is measured using a National Instruments (NI) C series 9223 voltage input module for both signal types, which is capable of simultaneous channel sampling as well as channel-to-channel isolation at 100 kHz/channel.

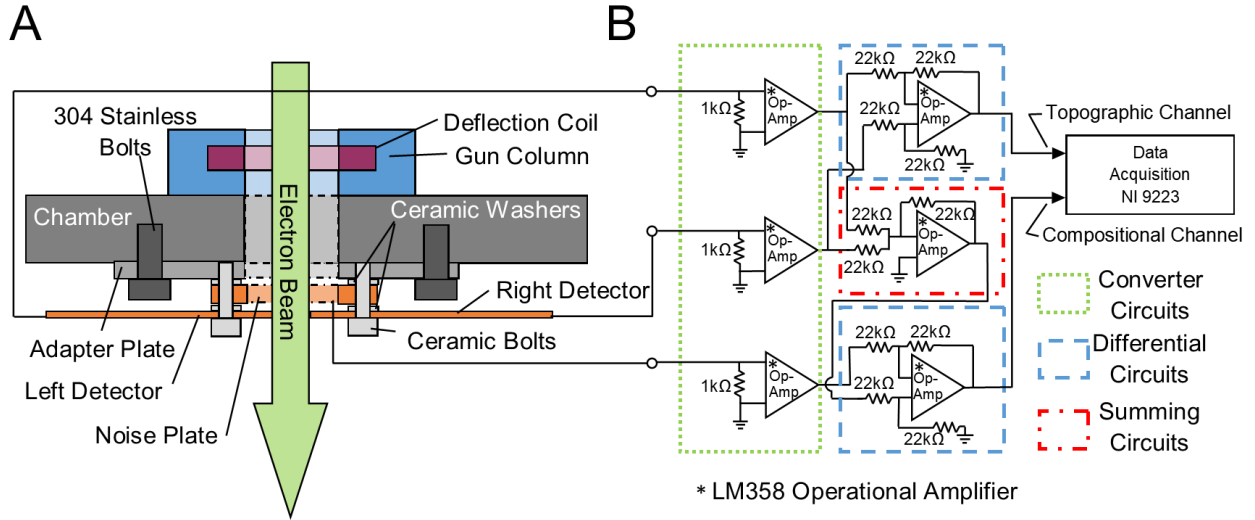


Figure 1: Illustration of the detector hardware mounted inside the EB-PBF vacuum chamber (A) and schematic of the hardware assembly circuit diagram showing the arrangement of the components (B). The current to voltage converter (converter circuits) are outlined in green. The differential circuits are outlined in blue, and the summing circuits are outlined in red.

4.2.3 Integration of the detector with the EB-PBF platform

Figure 2 illustrates the hardware components and software configuration described in this methodology. The Arcam EB-PBF system used in this study employs dedicated control cards for driving the electron beam control and for providing feedback to the machine PLC as seen in Figure 2. The PLC is located in the electrical panel on the lefthand side of the control cabinet (when facing the machine). The beam position was acquired by sampling the 0-10V feedback signals from both X and Y deflection control cards at the PLC input block. A value of 0V indicated no deflection (meaning the beam stays in the center), a positive or negative voltage along a given axis had a positive or negative linear relationship to the location of the beam on the build platform. The location of the PLC inputs was traced from the output of the X and Y deflection cards, respectively.

Total electron emissions are proportional to the incident beam current, which itself varies both within and between layers throughout the build process. Therefore, image-based comparisons throughout multiple layers need to account for this variation. This was accomplished by normalizing the TEE signal against the incident beam current to obtain the total electron yield (TEY). This required continuous monitoring of the incident beam current, which was inferred by monitoring the high voltage (HV) power supply beam current feedback signal. Figure 2 shows preliminary tests of single line melt tracks on steel plates with varying user defined beam currents that revealed a linear relationship with the HV beam current feedback signal.

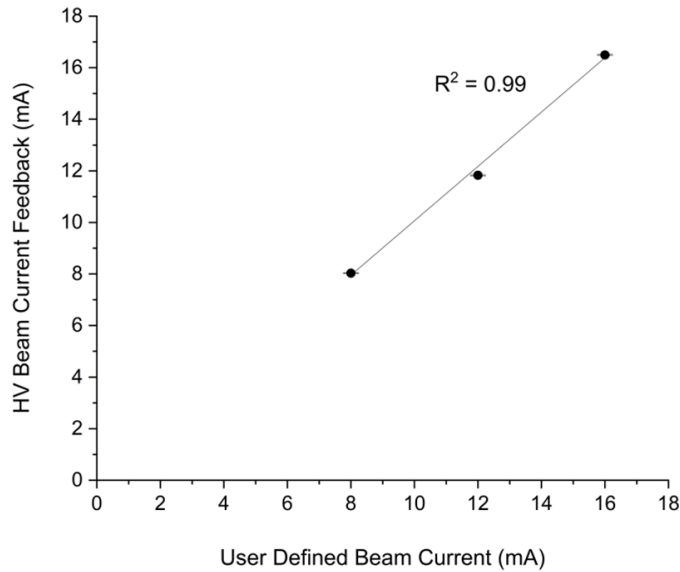


Figure 2: Plot of HV beam current feedback signal versus the user-defined beam current.

The HV beam current feedback signal was accessed and sampled via a breakout box between the existing D25 serial connector and the HV power supply, as shown in Figure 3. Acquisition of TEE, beam position, and current were automated using a NI LabVIEW 2019 software interface. It is worth noting that the acquisition system records beam current,

positional, and TEE data across all EB-PBF process steps, but in this study, we focused solely on the melt step. To trigger partitioning of the melt step acquisition, the control electrode (grid) feedback signal was sampled at 100 Hz from the PLC input using a NI 6009 Data Acquisition (DAQ) module. High-speed data acquisition was triggered by the change in the slope of the grid voltage feedback signal between process steps and terminated when the grid voltage reached a predefined threshold correlated to a nominal beam current of 0mA. This occasionally resulted in a few retained lines of preheating scan data, which were filtered by thresholding against the beam speed (beam speed calculations are described in detail in a later section). The TEE, X deflection, Y deflection, and HV beam current feedback data streamed from the NI9223 DAQ device. They were written to a NI technical data management streaming (TDMS) data file format for data processing. The process control loop in Figure 3 is described in section 2.2.5.

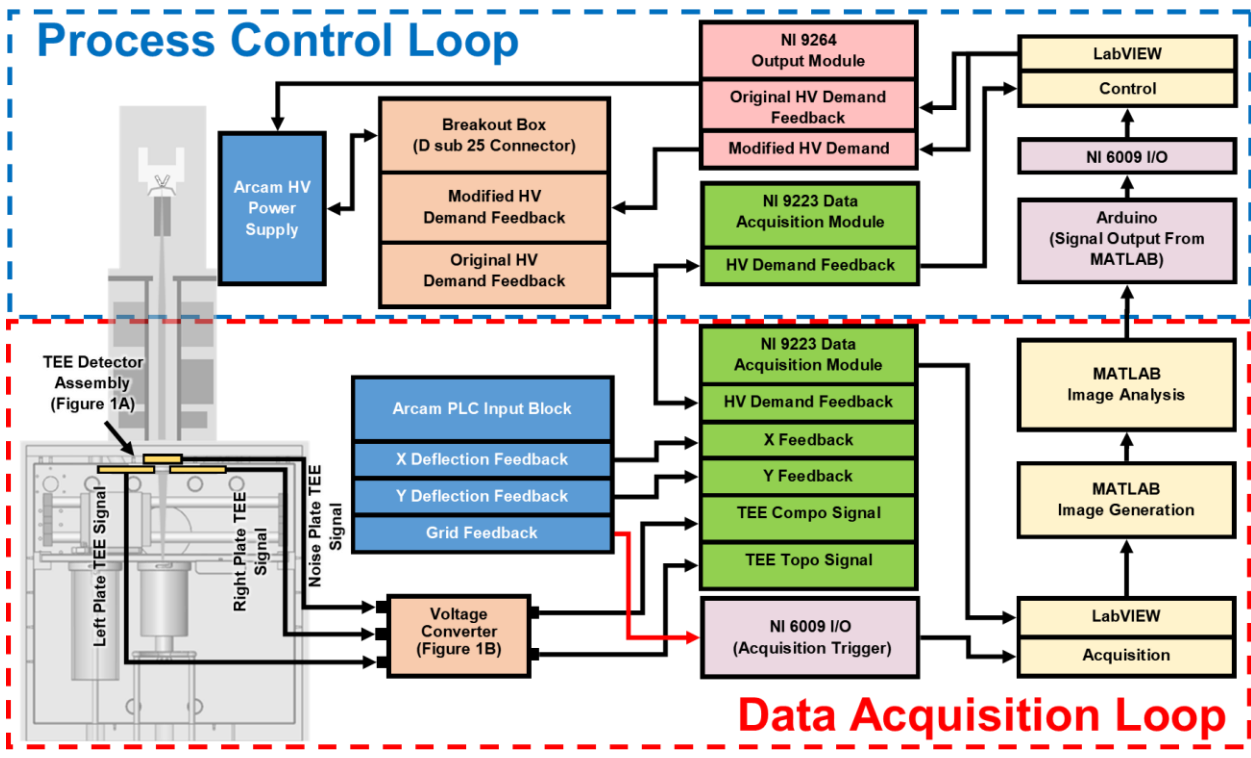


Figure 3: Schematic of the system integration. The data acquisition loop (bottom) shows the hardware used to acquire TEE, X, and Y deflection feedback, grid feedback, and HV beam current feedback. The control loop (top) illustrates the conversion of TEY data into a feedback signal used to modify the demanded beam current.

4.2.4 Image Generation

For each layer, the TDMS data files were imported into MATLAB (2019a). The X deflection and Y deflection feedback voltage arrays were converted to position, the beam current feedback array was converted to beam current, and the TEE array was normalized by dividing by the acquired beam current array to generate the TEY (total electron yield) array. To convert the array to images, the X, Y, and TEY arrays used a 2D binning strategy where the data were partitioned into uniform-sized bins arranged in 2D array based on the X and Y positions to relate the TEY data collected with beam raster position during melting. This method of data

quantization improves the signal-to-noise ratio and reduces the overall data size. It is similar to the analog-digital processing of a charge-coupled device (CCD) and commonly used in electron image reconstruction. The optimal number of bins was determined from the bit depth of the DAQ device (16 bit).

4.2.5 EB-PBF Sample Fabrication

As described in the introduction, several test geometries were fabricated for experiments designed to evaluate the advantages and disadvantages of the electron monitoring methodology. With each subsequent experiment, the geometric complexity is increased. First, prismatic samples, 10mm x 10mm x 10mm were fabricated for comparison to the methodology presented by Arnold et al. [12]. Building upon this, the second set of prismatic specimens were then fabricated to demonstrate the same approach overhanging bridge structures. This was done to observe the changes in beam speed and defects associated with changes in thermal conductivity between the part and the powder bed in the overhanging region. These prismatic samples measured 18 mm x 18 mm x 18 mm with a 6 mm x 9 mm x 18 mm downward-facing bridge section. As a case study, the electron monitoring, and beam positional tracking tools were then used to monitor the EB-PBF fabrication of a real-world geometry, a coupled cavity traveling wave tube. This geometry was selected because it contains complex internal features, unsupported down-facing surfaces, and enclosed volumes. Finally, the electron monitoring tools are used to implement a rudimentary control strategy and demonstrated for a prismatic specimen measuring 15 mm x 15 mm x 11.8 mm. For all experiments, samples were fabricated from the same batch of nitrogen gas atomized pure copper powder with a volumetric size distribution of 48-114 μm (d10-d90) as measured by laser diffraction (Microtrac S3500). Powder morphology

was spherical as observed by secondary and backscatter electron microscopy (JEOL 2000FX), and powder density was 8.92 g/cc measured by a nitrogen pycnometer (ASTM B923-16, Quantachrome MicroUltrapyc 1200e). The oxygen content of the powder was 190 ppm and was measured by inert gas fusion analysis (LECO OHN836). A chemical screening of the powders using inductively coupled plasma (ICP) revealed only negligible, trace quantities of other elements. Throughout this manuscript, we have used the standard coordinate system described by ASTM ISO/ASTM52921-13(2019), (Standard Terminology for Additive Manufacturing—Coordinate Systems and Test Methodologies). The TEE signal, beam position, and HV current feedback signals were sampled at 100 kHz/channel. The resulting images have a square pixel size of 100 μ m.

The following conditions applied to all EB-PBF experiments unless otherwise stated. For all experiments, samples were fabricated upon an oxygen-free electronic grade copper build substrate measuring 90 mm in diameter and 50 mm thick. The build platform was lowered by 50 μ m between each layer. Prior to spreading the first layer of powder, the build substrate was heated with the beam to 300°C and held for one hour. Throughout the process, bed temperature was monitored both with a thermocouple (type K) on the bottom substrate and with a 2-color pyrometer through a sapphire viewport built into the vacuum chamber. Melting was carried out using the standard raster, or snake pattern. With this pattern, the beam traverses the powderbed within the bounds of the geometry in a given direction, then moves a small distance perpendicular to this (the line offset) and reverses direction parallel to the first track. The line offset used was 130 μ m, and the direction of the hatch pattern was rotated 90 degrees with each successive layer. Powder bed preheating maintained the bed at a stable temperature of 300°C±30°C. In all experiments, beam focus offset from the calibrated position was 18 mA, and the

programmed beam speed was 1000 mm/s. After sample fabrication, the entire build volume was allowed to cool, under vacuum, until the temperature of the thermocouple fell below 32°C, at which point the vacuum chamber was ventilated to dry argon, and the parts removed.

4.2.6 Comparison of TEY melt imaging to μ CT

For the first experiment, twelve copper samples measuring 10 mm x 10 mm x 10 mm were fabricated. The beam current and the Arcam automatic control parameter ‘speed function’ described in detail by Narra et al. [27] were varied. The user-defined beam currents were 8, 12, and 16 mA and, the unitless speed function values were 10, 20, 30, and 40. Each sample was melted individually. During AM processing, TEY layer images were acquired and binned throughout the fabrication of samples with the previously described methodology resulting in 200 layers/images per sample. After fabrication and cooling, samples were removed from the substrate by a band saw, with a material loss of ~1.8 mm due to saw blade thickness at the bottom of the sample. The top surfaces of the samples were imaged using a Hirox optical microscope at 70x magnification with digital tiling to evaluate visible porosity or surface topography. We used μ CT data to non-destructively evaluate the internal porosity of the samples using a Zeiss Xradia Versa 3D X-ray CT system with 160 kV accelerating voltage at 10 W max power, producing a voxel resolution of 14 μ m. These data were used as the reference images for subsequent analysis and correlation of the TEY images generated during the melting step of EB-PBF.

Subsequently, the samples were sectioned with respect to the YZ plane using a low-speed diamond saw, hot mounted, progressively ground from 600 to 1200 grit and polished to 0.1 μ m alumina slurry. The optical microscope was again used at 70x magnification to generate tiled

images for porosity mapping. For comparison, the μ CT data and TEY images were also sliced in the YZ plane at the same measured location. Two methods were used to compare TEY images to μ CT images, the mean absolute percentage error (MAPE), and the structural similarity index (SSIM). The MAPE process calculates the relative error associated with values deviating from the overall mean (Equation 1). The SSIM leverages a methodology for predicting the perceived differences between two images with similar structure details where one image is referenced to the other (Equation 2). The equations for each are shown below, where details of the techniques can be found elsewhere [28,29]. Both techniques were applied in this study to compare structure and signal intensities of data from very different sources

$$\text{MAPE} = \frac{100\%}{n} \sum_{i=1}^n \left| \frac{\text{NI}_i^{\mu\text{CT}} - \text{NI}_i^{\text{TEY}}}{\text{NI}_i^{\mu\text{CT}}} \right| \quad \text{Equation 1}$$

Where:

$\text{NI}_i^{\mu\text{CT}}$ = Normalized Intensity of μ CT

NI_i^{TEY} = Normalized Intensity of TEY

$$\text{SSIM}(x, y) = \frac{(2\mu_x\mu_y + c_1)(2\sigma_{xy} + c_2)}{(\mu_x^2 + \mu_y^2 + c_1)(\mu_x^2 + \mu_y^2 + c_2)} \quad \text{Equation 2}$$

Where:

μ_x = average of x

μ_y = average of y

σ_x^2 = variance of x

σ_y^2 = variance of y

σ_{xy} = Correlation coefficient of x and y

TEY images were pre-processed in order to facilitate the comparison, and, for the purposes of this analysis, the μ CT were treated as the reference data. TEY images were first converted to 16-bit grayscale to match the image type of the μ CT data using ImageJ. The μ CT data had 14 μm resolution along the Z direction (build direction). They were therefore resampled at 50 μm intervals in the Z direction to match the layer thickness of the TEY data so that the 2D (X-Y) images from each dataset could be compared. The average intensity of the TEY image was adjusted to match the μ CT image using the MATLAB histogram equalization function, (imhistmatch). Image registration between the TEY and μ CT was performed using the feature-based image registration tools in the MATLAB computer vision toolbox. The structural similarity index (SSIM) evaluates variations in luminance, contrast, and structure of an image with respect to a reference image [28]. In this study, we used the μ CT data as the reference image. The SSIM outputs a matrix that represents the local SSIM value at each pixel, where smaller values (less correlated) appear darker, and higher values (more correlated) appear lighter. The reported mean SSIM value is the arithmetic mean of the SSIM matrix. The above procedure was then repeated for every layer in each sample.

In the MAPE approach, line profiles of TEY and μ CT intensity along the X direction were measured every 0.2 mm along the Y direction in a layer. Each datum along the profile line was normalized against the average intensity of the entire corresponding image from which it was taken. MAPE was used to compare the TEY to the μ CT data along the profile line. The overall average and standard deviation of MAPE values are also calculated for the entire image [29]. For further comparison to optical micrographs, image stacks of both the μ CT (14 μm voxel size) and the TEY data were resliced in parallel to the YZ plane using Image J (3D view plug-

in). 3D visualization of the sample porosity was reconstructed using Dragonfly software (V 4.1 from Object Research Systems).

4.2.7 Observing beam speed and TEY for Arbitrary Geometries

An inherent feature that results from the tracking of the beam positions during the TEE melt monitoring is that the beam speed at any point during the process can be easily calculated from the time-stamped X and Y positions using the distance equation in Equation 3:

$$s = \frac{\sqrt{(x_2 - x_1)^2 + (y_2 - y_1)^2}}{t} \quad \text{Equation 3}$$

Where s is the calculated beam speed, x_2 and y_2 are beam positions after moving from its previous position (x_1, y_1) for any position during rastering and, t is equal to the interval between samples (seconds).

To verify in-situ beam speed calculations, 10 mm x 10 mm x 10 mm copper sample blocks were fabricated on the EB-PBF machine with the automatic control functions disabled to prevent the system from overriding the user-defined speed. This ensured that the user-defined beam speed and current were used and, this was consistent with the methodologies reported by Guschlbauer et al., Lodes et al., and Raab et al., for pure copper [30-32]. The velocity and current settings were varied between 800 mm/s - 2100 mm/s and 8 mA-16 mA, respectively. Beam speeds were also observed with high-speed imaging (Photron SA-X2 High-Speed Camera) at 30,000 fps by repeated measurements of the distance the beam traveled between 50 frames. Figure 3 shows the average calculated speed from imaging compared to the user-defined beam speed. This technique was then applied to the 12 copper samples used in the MAPE and SSIM

analyses, which were fabricated with the Arcam automatic control functions enabled. Beam speed calculations were then used to observe the changes in speed implemented by the Arcam speed function and turning points functions.

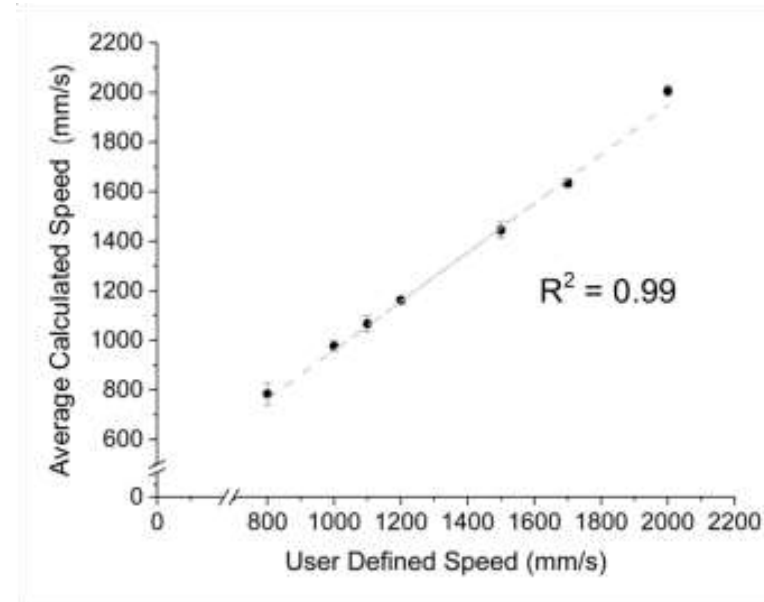


Figure 4: Plot of user-defined beam speed and calculated beam speed. Error bars indicate the standard deviation of measured speeds.

The velocity monitoring tool also allowed us to produce process 3D maps across multiple layers and areas of interest to compare with suspected porosity and other related defects from associated TEY data. By incorporating the monitored beam current data, we were able to plot a pseudo-volumetric energy density map of the EB-PBF processing space as a function of position and time compared and overlay these data upon the 4-dimensional (4D) TEY (density space). The volumetric energy density, E (J/mm^3), is often represented by the simple expression in Equation 4 where U is the accelerating voltage (V), I is the incident beam current (A), v is the beam velocity (mm/s), h_o is the hatch offset (mm), and t is the layer thickness (mm), and is a common means by which to visualize the processing space for a given alloy or set of conditions [32,33].

$$E = \frac{UI}{vht} \quad \text{Equation 4}$$

4.2.8 Mapping overhanging surfaces and complex geometries

In this portion of the experiments, we applied the TEE imaging and beam speed mapping capabilities to a geometry with complex thermal boundary conditions, focusing on overhangs. The thickness function is a control parameter within the Arcam EB-PBF system that increases beam velocity on downward-facing, or overhanging regions to account for the changes in thermal conductivity associated with these areas. At the first layer of an overhanging feature, the beam velocity is increased, and, with subsequent layers, the beam speed decreases inversely with increasing vertical distance from the overhang in order to lower beam heat input. Nine copper samples with cross-sections measuring 18 mm x 18 mm x 18 mm were produced with a 6 mm x 9 mm x 18 mm downward-facing bridge section, as shown in Figure 5. The basic melt parameters using a standard raster melt strategy were described previously. The typical Arcam automatic control functions were activated, which included parameters such as power analyze (surface temperature), speed function, turning points function, and thickness function. Nested within the thickness function are several other parameters that describe the rate and the profile of the change in velocity as a function of the distance from the overhang region are max thickness (T_{max}), the speed factor (S_f), the thickness factor (T_f), and the exponent factor (E_f), as demonstrated by Smith et al. in Equation 5 [33].

$$\frac{v}{v_o} = 1 + \frac{S_f}{\exp(E_f(T_{max} - T_f)) + 1} \quad \text{Equation 5}$$

In our experiment, the thickness function parameters of “speed factor” (S_f) and “thickness factor” (T_f) were varied from 0.5 - 1.5 and 10-30, respectively. Throughout the fabrication

process, the TEE data and beam positional data were acquired and processed using the methodology described previously. TEY and beam velocity maps were compared to μ CT and optical micrographs of the samples.

In order to demonstrate both the efficacy and potential utility of the TEE melt monitoring approach, the methodology was then extended to an arbitrary component geometry with complex features that have previously proven challenging to produce with EB-PBF. The component selected for demonstration, shown in Figure 5B, is a pure copper, S-Band coupled cavity traveling wave tube (CCTWT). The key features of interest are large spans of unsupported downward-facing surfaces and varying, non-prismatic, cross-sectional geometry. That is, this geometry and the beam tool paths associated with it, are significantly more complex than the prismatic samples previously reported for electron imaging in the literature. Additionally, selected spatiotemporal data associated with this monitoring approach were mapped over these 3D reconstructions and compared to TEY. One feature of the Arcam control system that is not typical in many AM platforms is that the machine control functions (PLC data) and commands are written to a text file. Altogether, several hundred time-dependent process variable data streams were recorded throughout a single run and mapped against TEY.

We arbitrarily selected several of these data streams parsed from the process log file using MATLAB. By aligning the timestamps with the time-dependent positional data streams (deflection coil feedback in X and Y), we were able to map these values in 3D space for both visualization and for correlation to defects observed in the TEY data in the same 3D space. In the visualizations, the log file values were interpolated to account for the wide variation in sampling rate compared to the positional data.

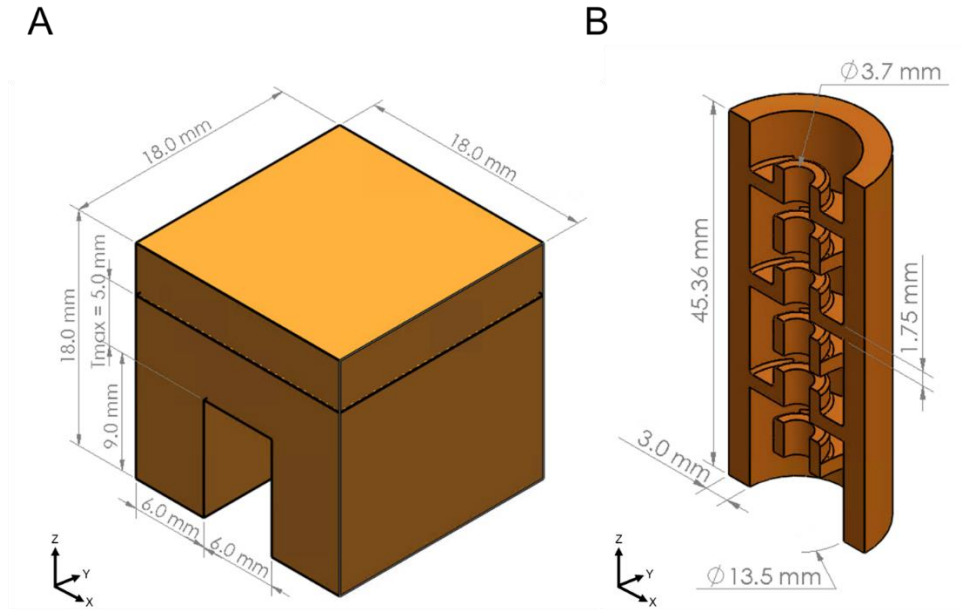


Figure 5: Illustration of the overhang geometry (A) and illustration of the CCTWT device (B).

The illustration is sectioned in the XZ plane to highlight the internal downward-facing features.

Note: images are not to scale.

4.2.9 Implementation of a Rudimentary Control Strategy Based on TEY

In a final experiment, we examined the implementation of a rudimentary control strategy based on monitoring of the TEE on a layer by layer basis as follows and illustrated in Figure 3. First, the high voltage power supply controller's demanded beam current (0-10V signal) was monitored using a NI9223 voltage input at 1kHz. Next, this signal was intercepted using a breakout box to access the individual contacts in the D-sub 25 connector at the HV unit control. As previously described, in-melt layer images were generated at the conclusion of each melt step using MATLAB. The image matrix was then averaged, and a single scalar value of average TEY was generated. This was compared to both a predetermined value for "solid" material and the measured signal input for demanded current. The dimensionless TEY threshold for solid material was set at 0.24 based on observations made from the initial experiments in this study. If

the average TEY of the image was below this threshold for four consecutive layers, MATLAB output a signal to increment the beam current by 0.5 mA. Four layers were chosen because, based on the previous experiments, it was not expected that the porosity would be eliminated within a single layer. With this incremented signal, LabVIEW then outputs a 0-10V signal to the high voltage power supply control demanded beam current input via a NI9264 voltage output proportional to the increment. The original demanded beam current signal was returned to the high voltage current feedback port on the PLC to prevent the Arcam control system from overriding our incremented current.

To demonstrate this, a copper sample with a 15 mm x 15 mm cross-section was fabricated to a height of 5 mm using stable parameters for high-density copper identified in the previous sections with the standard Arcam automatic control functions enabled. This step was taken to provide a stable base upon which to test the control algorithm. At the height of Z = 5 mm, we manually decreased the beam current from 8mA to 3 mA, resulting in a parameter space known to produce severe porosity in copper. This parameter set was used for an additional 1 mm, after which the TEY control algorithm described was implemented.

4.3 Results

Based on the following analyses of the TEE data collected during melting, it is prudent to highlight some current limitations in the interpretation of the results. The signals acquired by the TEE detector reported in the present study originate from multiple sources, including BSE, SE, and Auger electrons, as well as charge transfer induced by shielding gasses/plasma, thermionic emission and ejected powder particles. During the melt step of EB-PBF, the primary electron beam at an energy and current (I_{PE}) interacts with the powder bed, the melt pool and the

surrounding solid material. The bulk of the electrons are absorbed by the build volume, conducting a sample current, and generating the heat required for melting. Some electrons will be elastically ejected (BSE) and, a portion of which undergo inelastic collisions and lose energy. Some electrons within the interaction volume will be energized and emerge as true secondary electrons. Total electron emissions (TEE) refers to the collective mixture of these sources [34]. While the predominant source is most certainly backscattered electrons, this distinction may prove to be an important one in future studies. Backscattered electrons typically have a wider angular distribution compared to true secondary electrons, are more energetic and, therefore, easier to detect, amongst other sources of noise in the AM environment [26, 34]. Secondary electrons are also slower and less energetic, and will, therefore, lag behind backscattered electrons. In commercial EB welding systems, the detector is often biased to prevent secondary electron detection. In our study, no attempt was made to parse out the various components of this TEE signal.

Ultimately when an electron, regardless of its source, contacts the detector, a detector current is conducted. Due to the large observed variations in beam current (I_{PE}) at multiple time scales, the TEE signal is normalized to the instantaneous measured beam current. In equation 6, this ratio of the TEE to the primary beam current (I_{PE}) is referred to as total electron yield (TEY) [26].

$$TEY = \frac{TEE}{I_{PE}} \quad \text{Equation 6}$$

4.3.1 TEY melt imaging to μ CT Comparison

Initially, we loosely followed the qualitative comparison of in-melt images to laser microscopy and laser confocal microscopy reported recently by Arnold et al. for Ti6Al4V [11].

However, in our study, the comparison was made instead between the top surface/last layer of the TEY image and a μ CT image of the same layer for a direct comparison of structure and TEE signal intensity. We then extended the demonstration throughout all of the layers of the samples.

Figure 6 shows results from the MAPE approach for comparing normalized line profiles of the TEY and μ CT data sets for a single layer from the sample with a 12 mA beam current and speed function of 40. MAPE is a common measure of prediction accuracy in regression analysis [29,35,36]. In this analysis, the μ CT data were used as the reference set. Forty-eight line profiles equally spaced in Y and parallel to the sample X-direction were measured across each μ CT (Figure 6A) and TEY (Figure 6B) image. For clarity, the lines along which two of these profiles were taken are shown at Y = 7 mm and Y = 8 mm as green and blue dotted lines respectively.

Figure 6C shows a plot of the MAPE values for each of the 48 lines. The MAPE values associated with the lines at Y = 7 mm and Y = 8 mm are highlighted and circled as the green and blue points, respectively. The selected line profiles at Y = 7 mm and Y = 8 mm are shown in Figure 6D and 5E, respectively, to visualize examples of this analysis. The profile at Y = 7 mm shows no significant loss of spatial intensity and correlates well with areas containing no pores in μ CT data and no dark regions in the TEY. Areas of porosity observed in μ CT at Y = 8 mm show multiple negative peaks indicating an intensity loss for both line-normalized μ CT and TEY data sets. These spatially match the signal loss observed within the respective images. Closely packed porosity observed in μ CT, like those seen at the top and bottom of the samples, overlap in the TEY images leading a slightly weaker correlation in these regions.

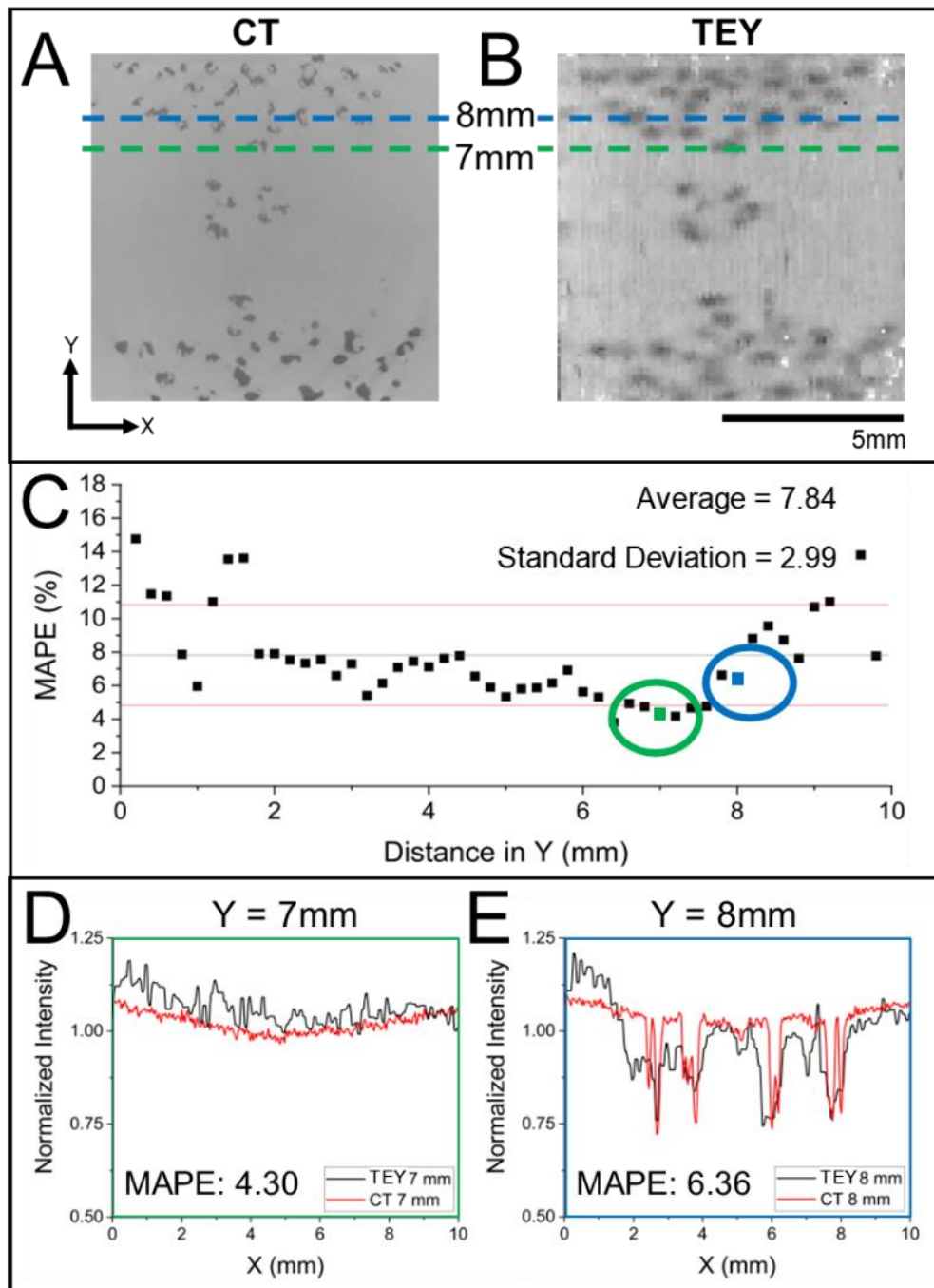


Figure 6: μ CT (A) scan and TEY signal image (B) of the top layer of a sample built with 12mA and SF 40. A plot of μ CT & TEY MAPE (%) comparison results for 48 equidistant profile lines (C), A plot showing the normalized line intensities for μ CT and TEY data, with MAPE results, shown in the X-direction for $Y=7$ & 8 mm lines,(D & E) respectively.

Figure 7 shows the top layer of four of the twelve pure copper samples melted with varying EB-PBF parameters and compares total electron yield (TEY) captured in real time during melting (top row) and computed tomography (μ CT) after fabrication (middle row). The SSIM images (bottom row) are a measure of image feature correlations and are included to compare localized spatial intensity differences between the TEY and μ CT data in an attempt to quantify the correlation between porosity observed in the μ CT data with signal loss in the TEY data. Melt parameter information for each melted layer is shown above their respective TEY images. These parameters were selected based on the published processing space for pure copper and were intended to produce a range of known sample conditions for electron detection and correlation [32,37]. The values shown below the SSIM maps in Figure 7 are the global numeric average of the calculation between TEY and μ CT images, which ranges from 0 to 1. The first two columns of data in Fig 6A are samples melted with lower energies of 8 mA, SF 30, and 12 mA, SF 40 where the porosity was clearly observed as dark regions in \square CT data. The corresponding TEY images appear to show a very similar structure, where dark regions correspond to a decrease in TEY intensity. Their respective SSIM structure correlations show a good fit spatially of 0.80 and 0.77, respectively. The two dense samples at 12 mA, SF 30, and 16 mA, SF 30 exhibited notably less structure and had better correlations at 0.94 and 0.87, respectively.

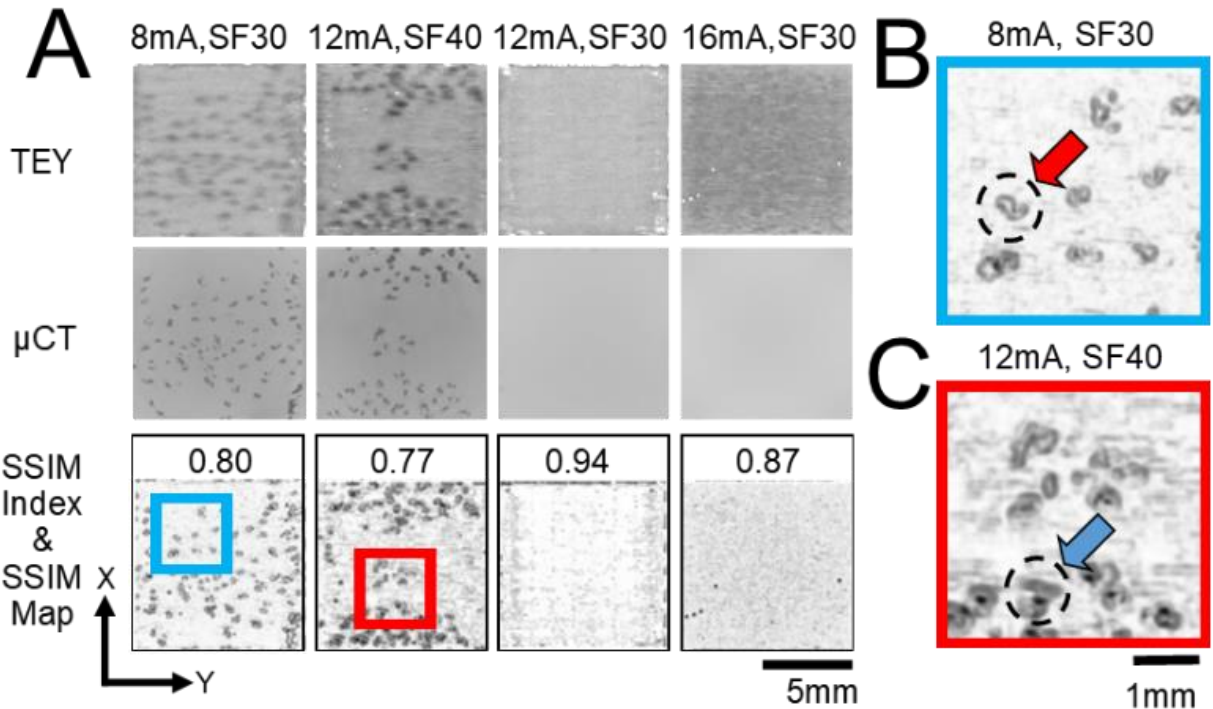


Figure 7: A) TEY, μ CT and SSIM index maps for four build conditions from 8-16 mA & 30-40 SF and a closeup of an SSIM index map for B) 8 mA, SF30 (blue box) and C) 12 mA, SF40 (red box) where the arrows in each figure point to features of interest.

Notable features in the SSIM maps were halo effects surrounding bright regions where indistinct or otherwise blurry TEY intensity indicated structure present around the sharper μ CT porosity. The SSIM images in Figure 7B and Figure 7C show magnified regions of samples melted at 8 mA, SF 30, and 12 mA, SF 40, respectively. The arrows in 6B show examples of the observed halo region. The bright region indicated a good positional match of the data, but the dark halo suggests that the TEY overestimated the defect size. Halos with a dark region were occasionally observed in the center (arrow in Figure 7C), indicating a poor spatial fit but, upon closer inspection, these were almost always accompanied by a thin bright ring between the dark center and the dark halo. In the case of Figure 7C, the effect was due to the μ CT identifying

a sharp, but complex pore geometry where the low-resolution TEY data was not capable of reproducing the complex shape and resulted in a poor local correlation.

The SSIM analysis was then expanded to include all layers within each sample. Note that we only examined 162 of the 200 layers because the material was lost to kerf during the removal of the samples from the build substrate. Images were therefore registered to the top surfaces of the μ CT data. Figure 8 shows the global (layerwise) SSIM value as a function of layer height for the four samples previously discussed in Figure 7. SSIM maps for 12 mA, SF 30, and 12 mA, SF 40 samples are also shown at 1 mm, 4 mm, 6 mm, and 8 mm layer heights to provide insight into how the signal structure is changing during the build process with different heat input parameters.

The lower density samples at 8 mA, SF 30, and 12 mA, SF 40 conditions have SSIM correlations, which range from 0.72 to 0.84 with a range of +/- 2.5-3%, respectively. Most of the error associated with the overall correlation calculation represent mismatches consistent with ‘halo’ features shown in Figure 7. The higher density samples have a correlation value exceeding 0.8 for all layers, due mainly to a lack of feature structure (porosity) and mostly represent image intensity comparisons. Both sets of image maps in Figure 8 are consistent in structure and intensity for each melt condition, respectively. However, some mismatch of features is especially noted in the edges of the 12 mA, SF 30 samples, and most likely are missed correlations due to complex topography associated with the edges of the sample produced during beam turning. In this case, the TEY is able to detect these features that the μ CT cannot. These data indicate that signal loss detected with the TEY compares well with observed features in the μ CT data throughout multiple layers and for multiple melt conditions of these simple prismatic geometries.

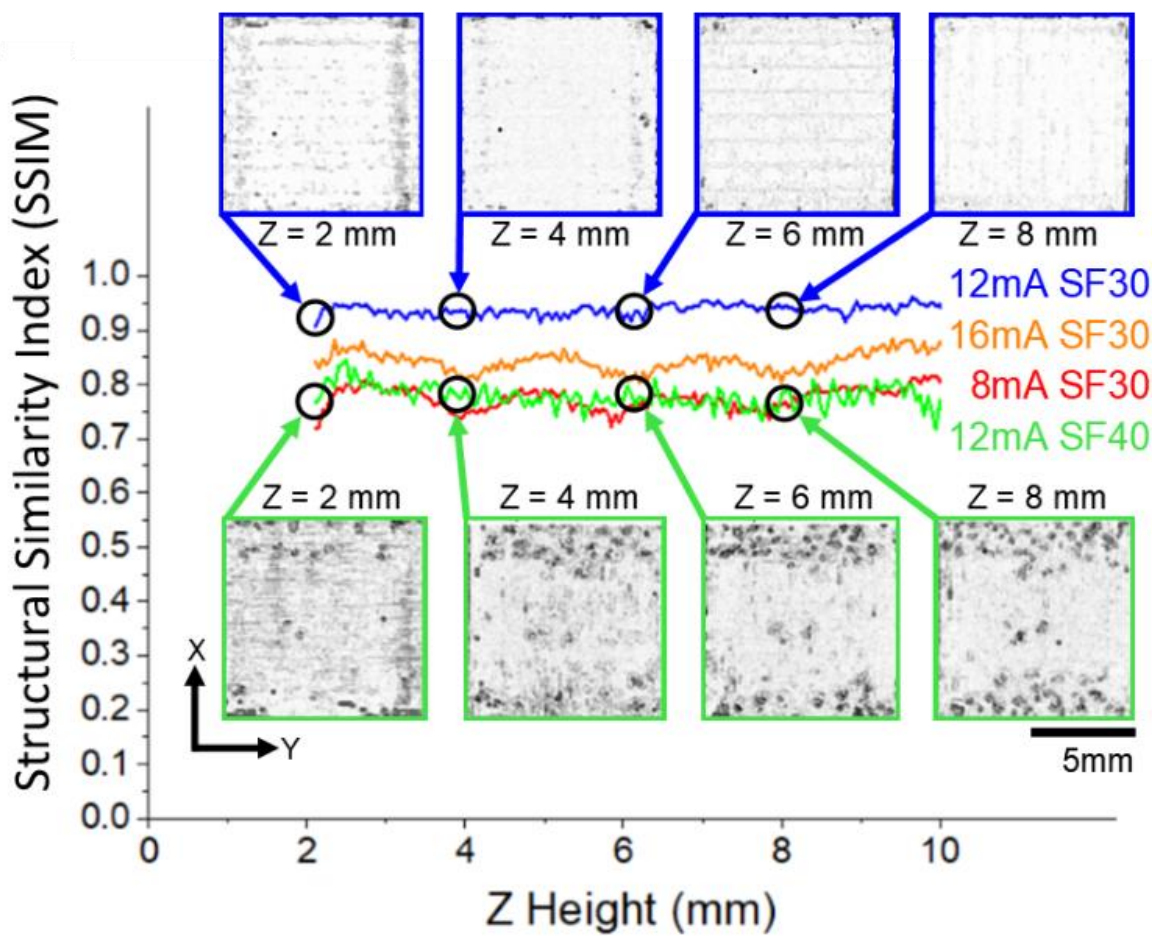


Figure 8: SSIM data for 8 mA, 12 mA, and 16 mA samples for all layers melted up to the 10 mm build Z height (mm). Individual SSIM map images are from 12 mA, SF 40 (green) and 12 mA, SF30 (blue) conditions at 2, 4, 6, and 8 mm build or z heights, respectively.

Since the SSIM and MAPE correlations both measure image structure similarities between μ CT and TEY data, spatially, they both correlate similar features in a different manner. The halo effect observed in the SSIM analysis is also seen in the MAPE analysis wherein the negative peaks in the TEY profiles are broader than the μ CT indicating good TEY signal loss correlations with structure location but, the details such as shape or complexity do not often match due to the different measurement technique and associated resolution.

Figure 9 is a more traditional metallurgical comparison using standard techniques such as μ CT and optical microscopy to compare with TEY signal loss. The physical samples were sectioned in half along the YZ plane and polished, and the μ CT and TEY data (previously discussed in **Figure 7** and **Figure 8**) are resliced in the same YZ plane, as measured with micrometers. Therefore, all of the data are representative of the selected cross-sectional plane for each sample. These 3D stacked and sliced images were registered to the top of the optical sample and reveal a variety of porosity morphologies from the bottom to top surfaces of the samples. In Figure 8A) and 8C), were the samples with the lowest energy density (8 mA, SF 30 & 12 mA, SF 40) and clearly demonstrated interconnected porosity from the bottom to the top surfaces in μ CT, TEY and optical images. This type of porosity morphology has been reported by Lodes et al. during the fabrication of copper samples by EBM at low energy melt conditions [30] and in Ti6Al4V by Schwerdtfeger et al. [37]. Recent reports concluded that the channeling is most likely due to a combination of low beam energy and molten pool surface tension coalescence initiating from a pore site early in the build process, which grew over the course of a build [10, 38]. As the energy density increases, illustrated in the 12 mA, SF30 and 16mA, SF30 samples respectively. The samples, as expected, are near full density at the higher energy input conditions and are consistent with published data on EB-PBF of copper [25,30-32]. It should be noted, as observed in the 12 mA samples that the speed function plays a significant role in melting, where slight changes in the speed function (SF30 to SF40) can cause significant changes in defect content, such as the porosity shown in the 12 mA, SF 40 data below.

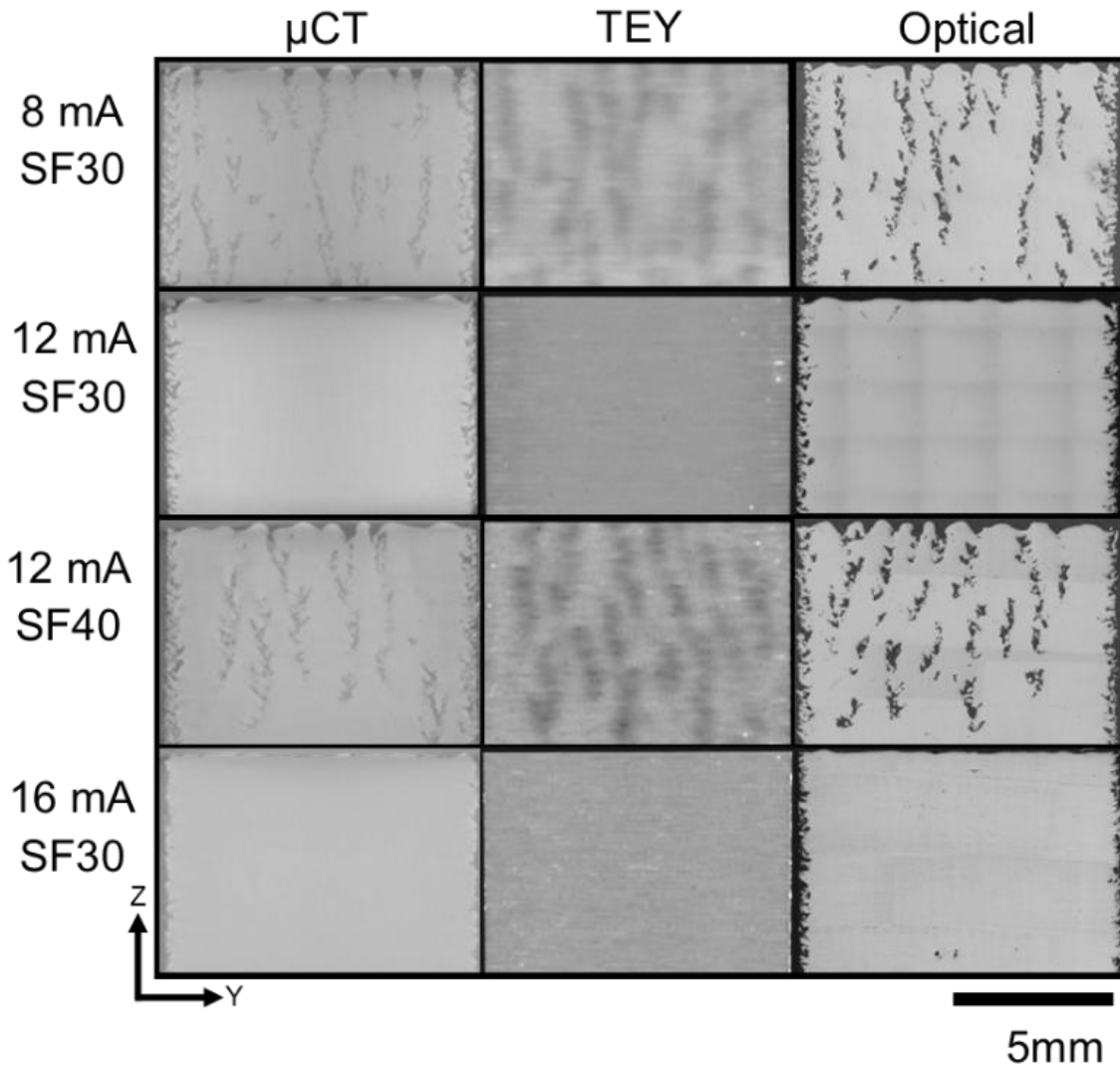


Figure 9: TEY, μ CT and Optical microscopy Y-Z plane cross-section images for selected samples. Build direction is vertical and parallel with the Z axis.

Figure 10 (A-D) are shown to visualize further and compare the TEY signal loss with μ CT. Figure 10A demonstrates the sharp μ CT porosity data stacked into a 3D representation of the sample melted at 12 mA and SF 40. At the same time, Figure 10B shows the TEY data of the same sample stacked for comparison. Columnar porosity is pervasive throughout the sample and is observable in both imaging modalities. As a comparison, the dense sample (16 mA, SF 30) is

shown in Figure 10C and Figure 10D for stacked μ CT and TEY data, respectively. The latter composite images both show comparatively less porosity located in the sample and indicate the cross-sectional slice shown in Figure 10D is representative of the near-full density sample.

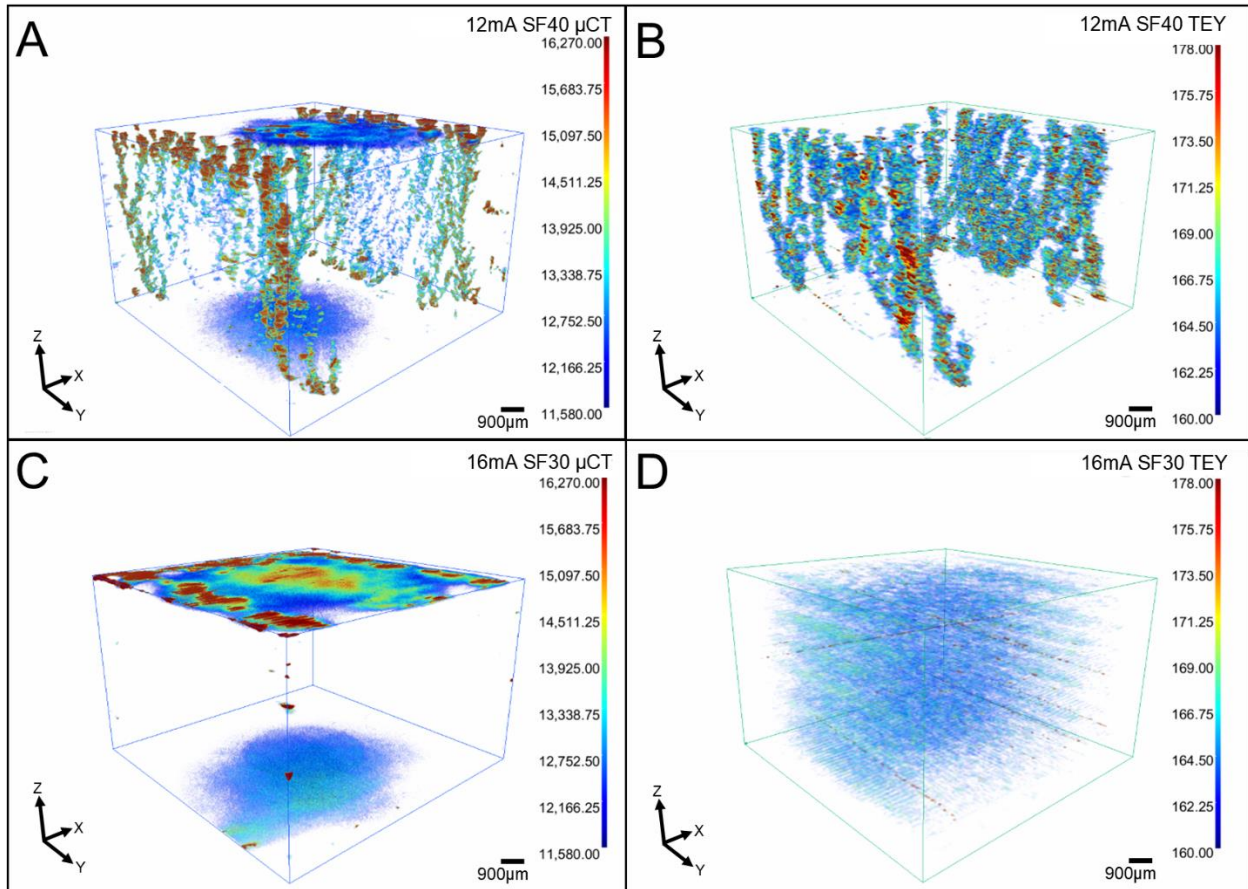


Figure 10: Stacked 3D maps of 10 mm x 10 mm x 10 mm cubes with solid background intensity removed to demonstrate porosity A) μ CT scans: 12 mA, SF 40 B) TEY: 12 mA, SF 40 C) μ CT scans: 16 mA, SF 30 D) TEY: 16 mA, SF 30

4.3.2 Spatiotemporal Process Maps

A common complication that arises in developing a feasible processing space for a given material using the EB-PBF process is that the constituents of the incident energy input, beam

current, and beam speed are not explicitly known to the user [27]. This is because the commercial feedforward, open-loop control system varies energy input within a layer and throughout the part fabrication process to account for predicted changes in local and global thermal conditions associated with part geometry. The beam current is adjusted throughout the height and usually stabilizes within a few layers [40]. While modulation of beam current may be the more desirable approach from a materials standpoint, beam speed is the most responsive parameter to adjust within a layer at the required rates in this particular EB-PBF system. The Arcam “speed function” adjusts the beam speed to account for changes in the beam current. The turning points function increases the beam speed at component edges to mitigate over melting, and the thickness function increases beam speed for downward-facing surfaces to account for the change in thermal conductivity between the solid part and the overhang. Nested within each of these functions are a myriad of driving parameters that dictate the magnitude and rate of these adjustments. When properly tuned by the user, these Arcam specific functions aim to maintain a relatively constant melt pool geometry and hence constant solidification conditions.

4.3.3 Beam Speed Mapping

An integral component of the TEY imaging methodology presented in this work is that beam position was tracked as a function of time regardless of the trajectory of beam travel. Average beam speed among any grouping of data can, therefore, be calculated and related to the TEY data in the same 3D space. This facilitates correlations between the performance of machine-specific automatic control functions and observed defects. Figure 11 shows a compilation of images from the four samples in Figure 7, but at an arbitrarily selected Z height of 5 mm. The top row shows the TEY images at 5 mm Z height (mm). The beam speed maps for

this layer are shown in the next row, and these show how the turning points function increases the beam speed at the part edges. Volumetric energy density maps (J/mm^3) are shown in the third row of Figure 11.

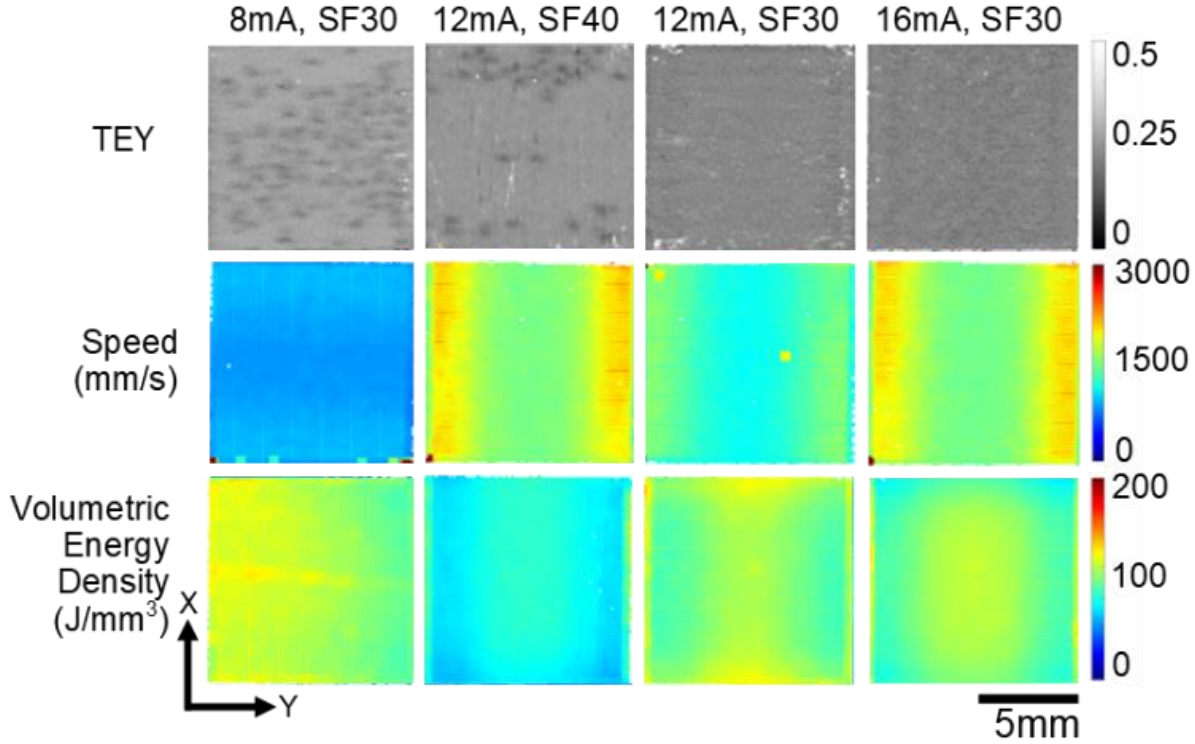


Figure 11: TEY (top row), beam speed (middle row), and volumetric energy density (bottom row) maps for the pure copper samples fabricated with parameters listed above each column and sampled at the height of Z height of 5 mm.

Since the turning points function is nested below the speed function in the system architecture, lower speed function settings result in slower beam speeds, and a higher speed function results in higher beam speeds for a given set of parameters. This is generally observable in the comparison between the samples melted with 12 mA and speed functions of 30 and 40, respectively. Here, the difference in density inferred from the TEY images between samples 12 mA, SF 40, and 12 mA, SF 30 shown in Figure 11 illustrates the sensitivity to higher-level speed

function and turning points function parameters at the same beam current. Note that the standard Arcam ‘turning points’ functions for Ti6Al4V were used for this study and were not modified. Occasionally, as discussed in the methodology section, a portion of the preheat current may be captured in the speed maps. This can be seen as yellow dots in the 12 mA, SF 30 sample. These artifacts are the result of triggering the melt scan acquisition with the change in the slope of the grid voltage signal. Such artifacts can be removed in post-processing because the data are time-stamped. They have been retained in this figure to both acknowledge and highlight this potential limitation.

Higher beam current also resulted in higher beam speeds associated with the turning points function, as seen by comparing the samples with the same speed function of SF 30, and beam currents of 12 mA and 16 mA consistent with the contribution of the speed function. This is why, for instance, the measured beam speed in regions is observed to be higher than the programmed beam speed (1000 mm/s). It is being upregulated by the speed function and turning points function to reduce the local energy density and account for both the thermal history as well as predicted changes in local thermal boundary conditions. Additionally, since data are registered with respect to time, key parameters such as sample melt order and beam trajectory are inherently encapsulated in these results. Overlaying the measured beam speed, hatch and layer thickness allowed us to visualize the localized volumetric energy density which was mapped over each sample area and throughout all of the layers. This illustrates the reduction of energy input associated with increased beam velocity within the turning points regions.

4.3.4 Thickness Function Mapping

In this portion of the experiments, we aimed to apply the TEY imaging and beam velocity mapping capabilities to a geometry with complex thermal boundary conditions, in this case, overhangs. Figure 12A shows the beam speed map for a cross-section in the XZ plane for the nine samples that were produced with the varying Arcam specific control parameters nested within the thickness function: the thickness factor, T_f , and “speed factor” S_f . Note that S_f is unitless, and T_f has units of millimeters. These data demonstrate the increase in beam speed in the down-facing region and the relative influence of each parameter. The plot in Figure 12B shows the same data extracted from a line profile along the Z direction in the center of each specimen. The layer height in the plot indicates the distance in Z from the first overhang. At the height of $z = 14$ mm, the T_{max} value (5 mm above the overhang at $z = 14$ mm) is reached, and all nine parameter sets return to the base parameters which are not influenced by the thickness function parameters beyond this height.

These data corroborate the previous work by Smith et al. [33] and are consistent with the arithmetic predictions. The images shown in Figure 12C and Figure 12D are TEY maps of samples with a thickness factor of 1.0 and a speed factor of 10 and 30, respectively. Note that, like the turning points function, the thickness function is influenced by other parameters (e.g., beam current) not necessarily embodied in Equation 5. TEY maps were extracted from the XY plane at Z distances of -1.0 mm (i.e., 1 mm below the first downward-facing layer) 1.0 mm and 3.0 mm above the first downward-facing layer.

The sample with a speed factor of 10 (Figure 12C) initially showed a higher TEY intensity at a distance of 1.0 mm above the overhang. However, this resulted in swelling and an uneven surface. On the other hand, the sample with a speed factor of 30 (Figure 12D) exhibited

a low TEY intensity at a distance of 1.0 mm above the overhang. This resulted in a flatter, but a porous downward-facing surface that propagated through the sample. These observations are further supported by the optical cross-sections of the same samples shown in Figure 12E. Previous work by King et al. had demonstrated how increasing the beam speed for the overhanging regions in Laser Powder Bed Fusion (LPBF) of steel both reduces the localized energy density and distortion [41]. The beam speed is reduced after several layers are built up, and a thermally conductive pathway is established through the material.

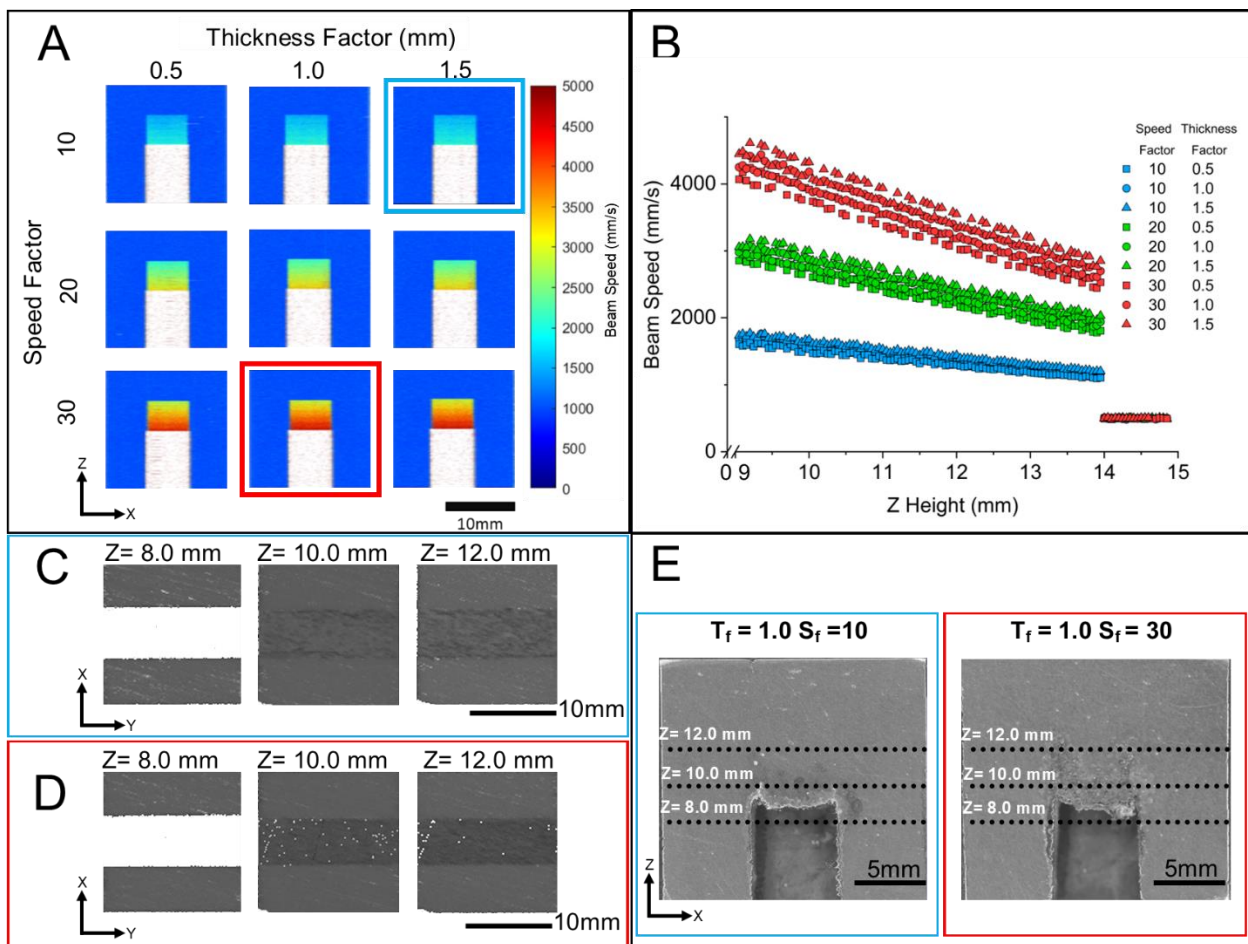


Figure 12: Beam speed map section in the center of the XZ plane for the overhang experiment showing the change in beam speed in the overhang region (A). A plot of the same data extracted from a line profile in the center of each sample oriental along the Z axis (B). TEY images at 1mm below (left), and 1 mm and 3 mm above the downward-facing surface for a thickness factor of 1.0 and speed factor of 10 mm (C) and 30 mm (D). Tiled optical microscope images of the cross-section at each corresponding height and condition, respectively.

4.3.5 Process Parameter Mapping

In the following section, we have plotted selected data from the preceding experiments (12 prismatic specimens and 9 overhang geometries) in volumetric energy density space. Plotting the TEY, beam current, and beam speed observations, from our own experiments, reveals clarifying trends regarding the functionality of the EB-PBF automatic parameters and their relationship to observed defects in the samples. **Figure 13** shows the reported processing space for EB-PBF of copper [37]. It should be emphasized that although the volumetric energy density is a commonly reported value in the literature, it produces a relatively subjective value that does not consider a great many factors, such as spot size, powder packing, powder size distribution, oxygen content, and absorptivity and thermal conductivity of the powder bed or material. While we have access to some of these data, they are often not reported in the literature. We have, therefore, mapped our data in the same space for the purposes of comparison. Indeed, all of the sample values reported previously are derived from prismatic (constant cross-section) geometries and, with the exception of the data reported by Ledford et al. and Frigola et al., the automatic control functions were explicitly disabled. As reported, these data suggest a narrow processing window for EB-PBF of pure copper [138], but also infer that the optimal energy density (or processing space) can be distilled to a singular value. While the reported data are validated by their repeatability across multiple studies alone, they are valid only for a narrow set of boundary conditions and do not consider the extreme variability in thermal boundary conditions associated with complex geometries, overhangs, and component borders.

Included in Figure 13A are the high-fidelity beam power and velocity measurements for the samples included in the present study. A threshold of 99.5% relative density is used to delineate porous from dense samples in this plot. These data indeed show the variation in local

energy density required to account for changes in the boundary conditions. Included in these plots are data collected throughout all 200 layers of the build for each of the four samples.

Following this, Figure 13B plots the arithmetic mean of the beam current against the arithmetic mean of beam velocity for each layer of each prismatic specimen reported in our study. Here we can observe a notable linear relationship between the samples with the same speed function. That is, these data explicitly demonstrate the functionality of the system control. As others have suggested [42,43], the speed function represents an index of idealized melt pool sizes along the lines of constant power/velocity ratios. Figure 13C shows the same volumetric energy density space for the samples in the present study and embeds within each data point the linear distance (parallel to the hatch direction) of that measurement from the center of the sample. This has a tendency to illustrate that the edges of the samples lie in regions of lower energy density regions (higher speed) driven by the turning points function. Figure 13D incorporates the TEY data, which we have established as a proxy for observed porosity in CT scans (within the bounds and context of this study). For samples with 12 mA and 16 mA beam current, the long excursions into low volumetric energy density represent the effect of the turning points function, but also show the increase in density between sample 12 mA, SF 40 and 12 mA, SF 30. These results show the variability required within the processing space to maintain constant solidification conditions, based on the previous SSIM observations, a TEY value of ~0.24 represents a reasonable threshold delineating dense from porous samples.

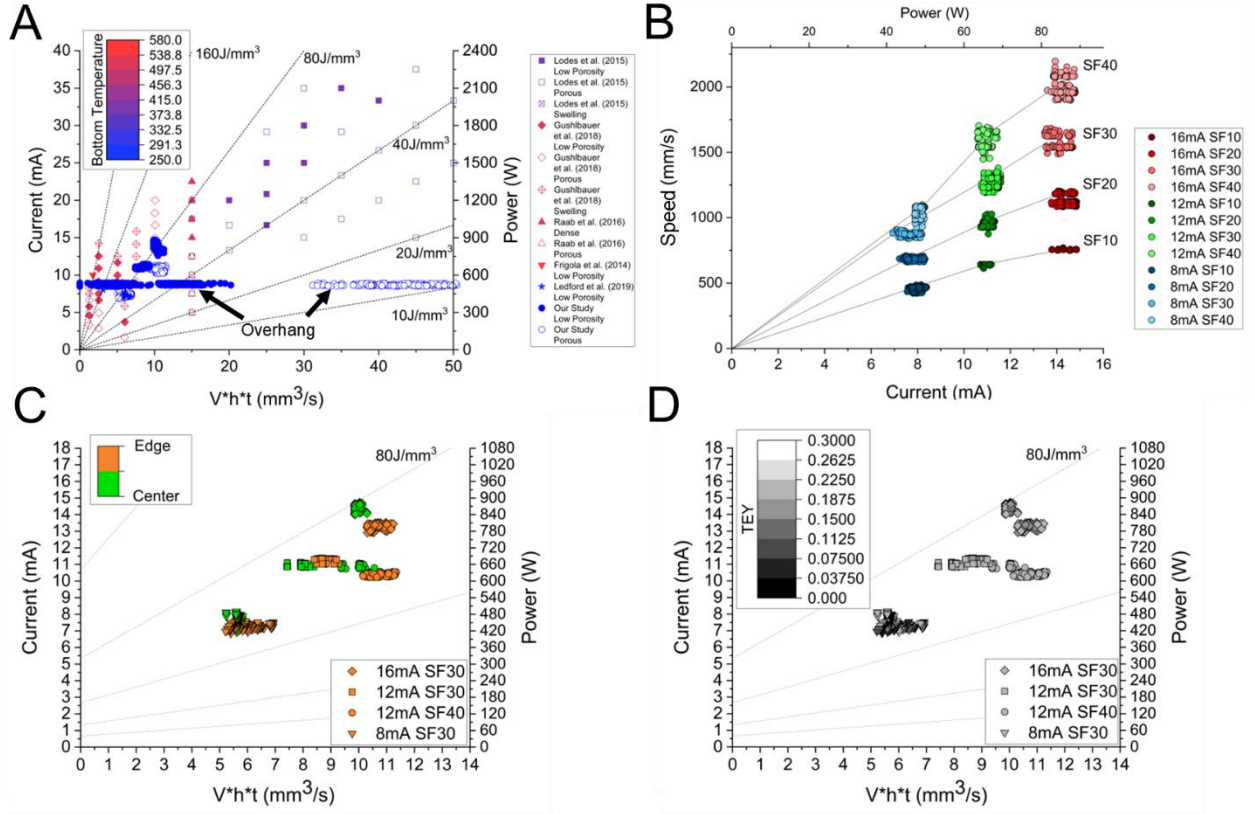


Figure 13: Process space maps for EB-PBF of pure copper, including this study (A). The average beam current and velocity for each layer from the 12 prismatic samples (B). The relative position of the beam within samples. The volumetric energy density space, which includes TEY data (D).

4.3.6 PLC Data mapping and TEY Correlation

This highlights another unique aspect of the approach outlined in the methodology presented in this paper. The ability to acquire time-based beam positional data inherently enabled us to map any in-situ monitored data, as well as other time-stamped system PLC log file data as a function of the 3D position as shown in Figure 14. To illustrate the utility of these tools in a real-world application, they have been applied to the EB-PBF of a high purity [25] copper S-Band CCTWT. This complex geometry features bulky sections, thin-walled sections, and large spans

of unsupported downward-facing surfaces. Figure 14 shows 3D cross-sections in the YZ plane of various recorded and calculated process parameters overlaid as 3D spatiotemporal maps onto the part geometry. The TEY maps shown in Figure 14A indicate good density throughout the process, or rather a lack of detectable porosity; however, this is reduced somewhat overall in the downward-facing overhang regions. This is indicated by a darker TEY intensity. The increase in beam speed in the unsupported downward-facing regions is also evident in Figure 14B. Figure 14C shows the filament current feedback voltage as a function of time. The filament current is adjusted by the system to account for the change in filament cross-section over time. Figure 14D shows the column pressure. Notably, a high-pressure event recorded at approximately Z=23 mm corresponds to a series of beam arc-trip events that occurred at this time. This resulted in a lack of fusion that is identifiable as a dark band in the TEY data maps at the same location. Figure 14E maps the build temperature as measured by a thermocouple at the bottom of the substrate. A notable increase by about 8-10°C is evident at the height of Z = 12 mm. The TEY data were also compared with a map of the beam location at any point in time (Figure 14F).

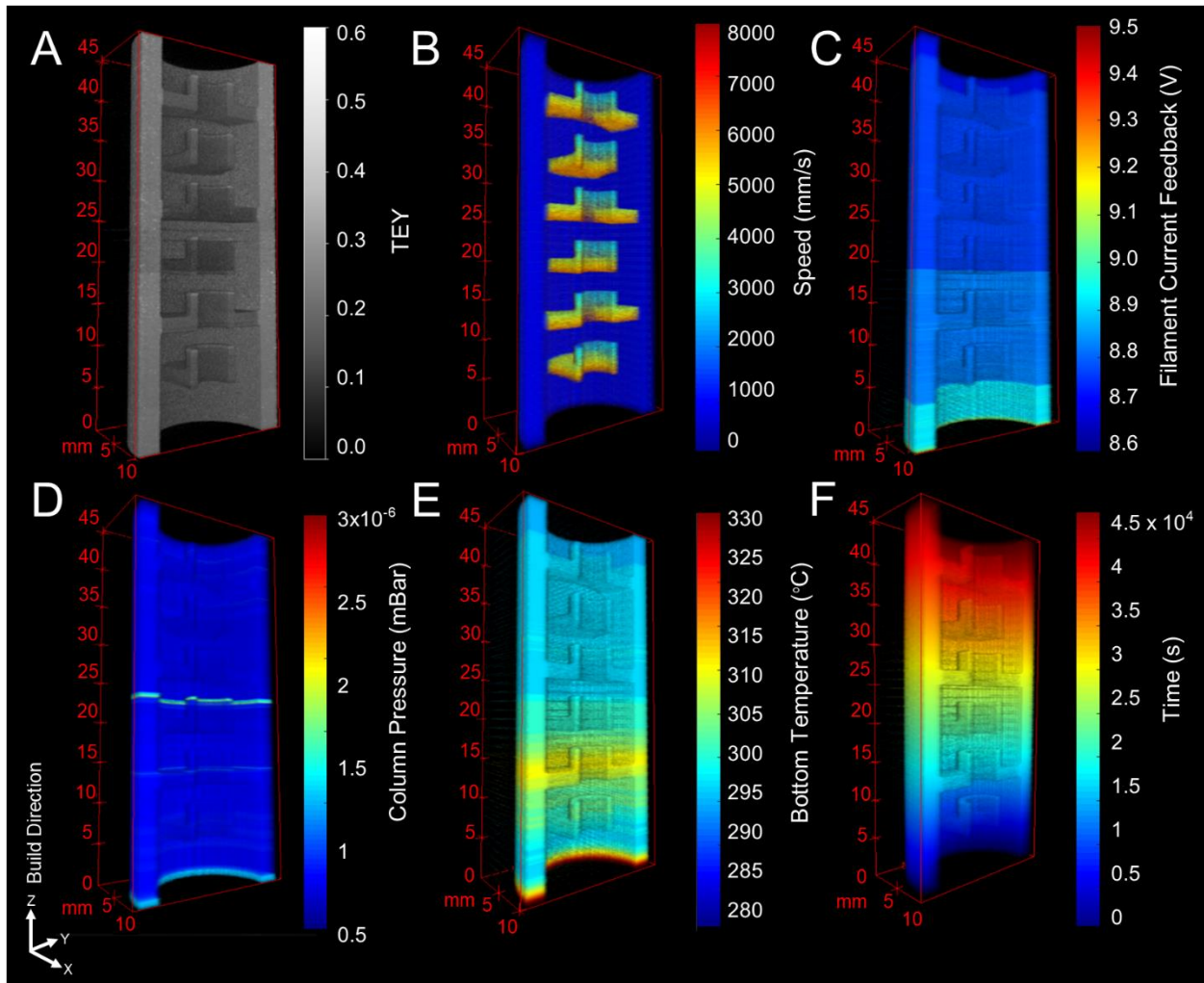


Figure 14: 3D data maps for CCTWT device fabricated from pure copper A) TEY data B) beam speed C) electron gun filament current feedback D) column pressure E) bottom thermocouple temperature F) beam position as a function of build time

Figure 15A shows the beam position as a function of time for the first layer of the process build for which the CCTWT device shown in Figure 14 was one of four devices on the build substrate (dark blue, Figure 15A). On the local scale, this provides information, including the beam trajectory and part melt order. It was demonstrated recently by Yoder et al. [44], the order in which parts are melted can have a profound influence on the thermal history experienced by

AM components and hence solidification conditions and microstructure. This capability is significant because these data are not always apparent to the machine users or explicitly controllable. This is further resolved in Figure 15B, which shows the melting direction and the orientation of the line offsets (hatch spacing) in greater detail. The noise in the center of the device is indicative of the beam jumping from one side to the other (e.g. white arrow in Figure 15B). Figure 15C shows the melt order for the beam during the contours step, which multiplexes the beam into several spots. This so-called “spot melting” strategy is able to maintain multiple liquid melt pools. The corresponding TEY data are encapsulated in Figure 14A. These figures further demonstrate that the TEY data and their corresponding spatiotemporal maps can be collected for arbitrary geometries and complex toolpaths.

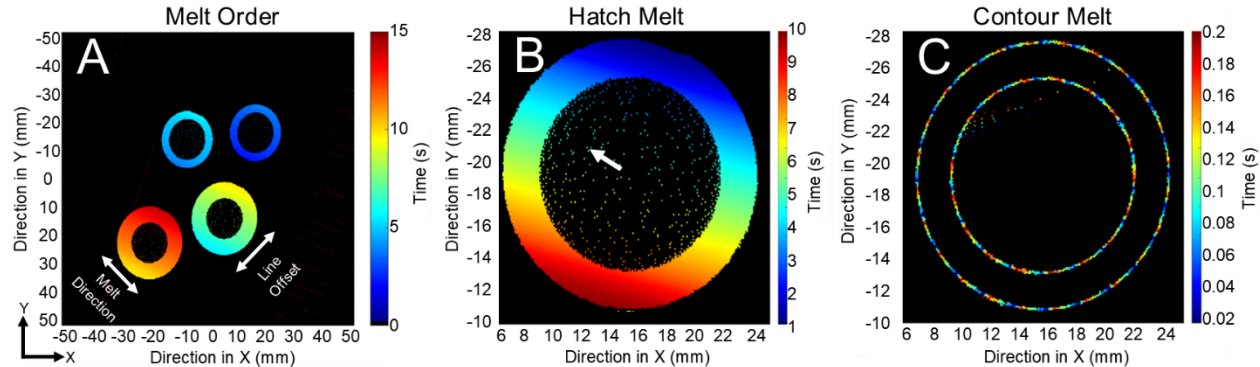


Figure 15: Shows beam position as a function of time for the first layer of a copper build. The melt order and hatch direction are evident in (A). At shorter time scales, the hatch melt order is further resolved (B) for one of the samples. Imaging with complex tool paths that involve beam multiplexing (spot melting), as is commonly done for part contours and arbitrary part geometries is possible (C).

4.3.7 Control Experiment Results

A control experiment was performed as described in section 2.2.5 to test whether the TEY signal intensity, which we have correlated to sample porosity observed in μ CT, could be utilized to provide a feedback signal to adjust parameters and correct for porous regions during melting automatically. In this proof of concept, the beam current was adjusted on a layerwise basis to regulate overall energy input. Figure 16A shows a tiled optical cross-section of the sample produced by the control experiment where the initial 5 mm of the sample had little porosity and was fabricated using a published high-density processing space [32, 37]. This is indicated as the region (i) in the figure. Note the sample has been removed from the build substrate by sawing, as previously described. Beam current was then manually reduced to a known poor density processing space with a melt current of 3mA and a beam speed of 600 mm/s. The reduction in beam current was accompanied by high levels of porosity in the sample (region ii). The loss of TEY signal is demonstrated in Figure 16A at the 5 mm height due to the drop in melt current. This was continued for 1 mm of build height to establish a porous base. At the height of 6 mm the TEY control algorithm was implemented (region iii). As observed in Figure 16, the TEY signal increased as the experimental control system ramped current over the next 4 mm of build height until the signal stabilized, producing high-density layers again with 8 mA current. The TEY value of each layer is also plotted as a function of build height in Figure 16B, on the same plot, the control algorithm's adjustments in beam current are also shown.

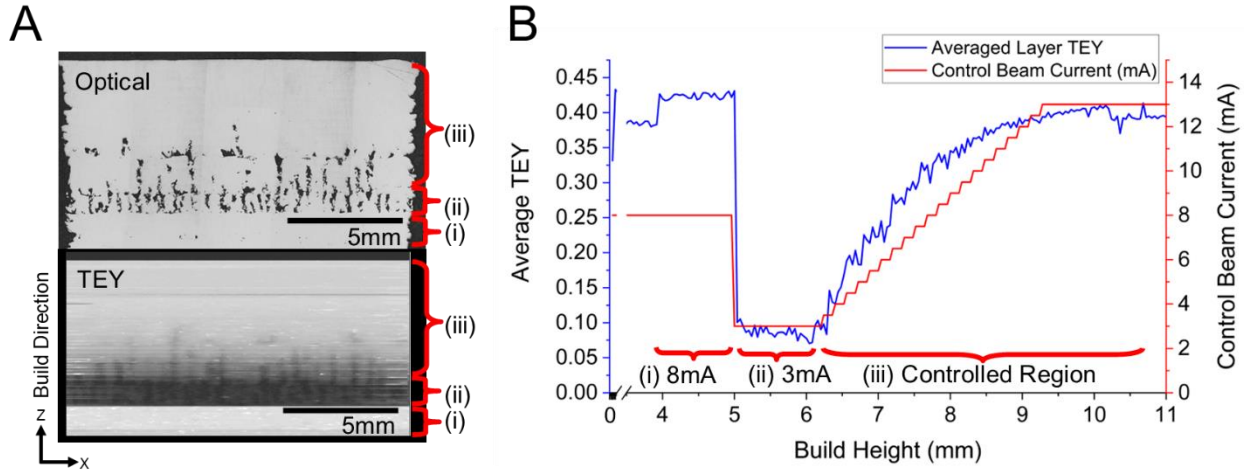


Figure 16: Control experiment showing TEY and optical cross-section of experimental result (A) and average layer TEY intensity and control beam current vs. build height (B).

4.4 Discussion and Conclusions:

In this work, we have presented a methodology that allows users of EB-PBF systems to monitor total electron emissions in real-time and at multiple length scales throughout the entire part fabrication process. Using a two multi-sensor TEE detector capable of both topographic and compositional operating modes, we have shown that loss of signal events monitored in the TEY data can be quantitatively correlated to observed defects in μ CT data. We have also demonstrated that the mapping of process-specific data related to beam current, beam velocity, or time-stamped PLC outputs in within the 3D space of the component are also inherently embedded in this approach and can be correlated with observed defects inferred from real-time TEY data.

4.4.1 Material Considerations

While many studies have focused on Ti6Al4V, because of its relative maturity in the AM industry. Pure copper was selected as the vehicle for these experiments for several reasons. First, there has been a growing interest in the processing of pure copper. As we (and others) have shown in recent publications, the EBM process is well suited for fabricating copper components [25,30-32,37,45-51]. Next, copper is a commercially available and supported development material for the Arcam EBM system, and there is a growing set of collective data demonstrating that the EBM processing space for copper is both narrow (compared to lower thermal conductivity materials like Ti6Al4V) and extremely sensitive to external boundary conditions (i.e., changes in thermal conductivity associated with variations in oxygen content and powder size distribution) [30-32,37]. The difference between the thermal properties of the solid part and the surrounding powder bed presents processing challenges and illustrates an extreme example of the capability and the functionality of the Arcam A2 automatic control parameters. As recent publications on electron monitoring in AM, and decades of electron microscopy would suggest, the methodology described here should be valid regardless of the metal or alloy processed.

Fundamentally, EB-PBF is ideally suited for low volume processing of extremely complex components for critical applications and materials. However, the presence of defects at different temporal and spatial scales that have rendered AM production and qualification an intractable challenge. Non-destructive evaluation (NDE) methods are typically used to identify these defects post-fabrication. However, AM inevitably enables geometries and materials that are challenging to evaluate with existing NDE techniques [55, 56]. X-ray μ CT is becoming an invaluable NDE technique for qualifying AM components due to its 3D spatial representation of the fabricated part. However, x-ray μ CT presents issues when dealing with higher density

materials due to limited x-ray penetration, which limits the size of parts that can be reliably scanned and increased scan times [57]. In these cases, smaller representative components may be scanned but may not be fully representative of the actual component with its complex geometry and differing thermal history. A review on the use of x-ray μ CT for AM components by De Chiffre et al. point to the limitations associated with part size, setup and scan times, and scan costs, which hamper adaption as a qualification method [58]. This challenge was directly experienced in the execution of this study. In this study, the Zeiss CT used at maximum power (160kV, 10W) was able to image the 10 mm x 10 mm cubes used in the comparison of the TEY data to μ CT (section 2.2.1), but not the 18mm cross-sections used in the overhang geometries (section 2.2.4). For this reason, only qualitative optical micrographs of the overhang geometries were available for analysis. Note that this is not necessarily fundamental. A more powerful scanner (e.g., 240kV or neutron tomography [66]) could, perhaps, produce better results. Nevertheless, one could conceptualize a part sufficiently large or sufficiently dense (e.g., tungsten) to prevent the practical implementation of x-ray μ CT. Based on our results, the 10 mm x 10 mm cross-section for a copper sample appears to be approaching the limit for the x-ray μ CT system used. To illustrate this limitation, Figure 17 shows both 3D x-ray μ CT and TEY reconstructions of a 10 mm x 10 mm x 10 mm copper cube produced with EB-PBF base parameters identical to those previously described in section 2.2, with a SF value of 20 and a beam current of 12mA. Regardless, as observed in Figure 17, the x-ray μ CT was unable to penetrate the entire sample for reasons that are not entirely clear (making SSIM and MAPE analyses impossible for this sample). The TEY data, on the other hand, is free of such aberrations, albeit with a lower resolution.

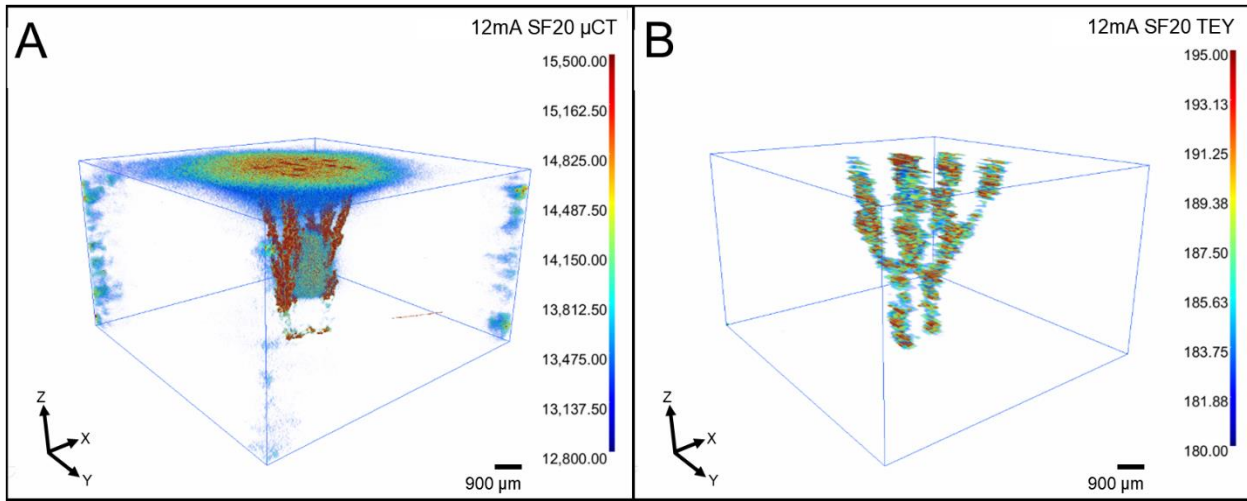


Figure 17: 3D x-ray μ CT (A) and TEY (B) reconstructions of a 10 mm x 10 mm x 10 mm copper cube. In this example, the x-ray μ CT could not penetrate the sample, but the TEY is able to resolve the internal features.

The copper used in our study has a density on par with nickel and stainless steel alloys, we can, therefore, speculate that similar challenges and opportunities exist and that the methodology presented should be applicable to these materials as well. Further studies will be required to validate this hypothesis. Furthermore, as higher density materials such as molybdenum [59,60], tungsten [61-63], or niobium [64] become more prevalent in AM, it will be necessary to develop new in-situ inspection techniques that can accelerate component inspection, qualification, and certification. In a recent publication, Wong et al. demonstrated electron imaging of solid samples in an EB-PBF system that included materials such as 316 stainless steel, Ti6Al4V, tungsten, and silicon [65].

4.4.2 Interpretation of TEY Data

The interpretation of electron images generated from a constant, low current, scan of the powder bed/part surface with a rectilinear scan strategy has been previously demonstrated [9-11,13-17] and is analogous to scanning electron microscopy (SEM) of a metallic surface. In one instance, the post-layer scan strategy was used on a non-commercial EB PBF platform after each layer of a Ti6Al4V run to map the process space for that material [11]. The same is not true for electron signals collected in near real-time during the melt step. Our data suggest that TEE data acquired from a turbulent liquid melt pool does indeed vary based on the angle of incidence, based on the local liquid topography, but also that this is in constant flux until solidification, which may occur several scan lines later. The interpretation of these data may be significantly more convoluted than has been suggested in previous works. High-speed imaging of the EB-PBF melt pool (at ~30 kHz) shown in Figure 18A-C and the associated illustration in Figure 16D demonstrate the localized dynamic, tumultuous conditions that encapsulate a number of simultaneous interfacial events including, kinetic charge transfer, melting at the liquid front, powder coalescence, powder/liquid ejection, plasma vapor jetting, and liquid convection and turbulence within the melt pool. Figure 18A shows the melt pool as the beam is starting a new raster melt line. This image illustrates a melt pool as the beam has just turned, and the speed is relatively fast with lower heat input compared with the steady-state line energy. Figure 18B shows a high-speed image at $t = 13$ milliseconds and represents a steady-state melt condition in the center of the melt line. This image demonstrates the violent and complex interactions occurring as the liquid is ejecting from the pool, plasma is observed, and the melt pool has obvious protrusions and depressions as it melts under these specific local conditions. The image in Figure 18C was captured near the end of the melt track before the beam turns to form the next

raster line during fabrication. While not as turbulent as the previous image, obvious liquid is being ejected, and the pool has undulating features as it interacts with the beam.

These high-speed image observations are well established in reported EB process simulations [38,52-54]. It is, therefore, necessary to highlight the following distinction; while our data suggest that a localized reduction in the TEY signal intensity may be associated with observed defects in optical and μ CT images of the same samples, it is also clear that we are not directly ‘imaging’ these defects. For clarity, we refer to suspected defects observed in TEY data as ‘loss of signal’ as opposed to ‘porosity. Each measurement, therefore, encapsulates both backscattered electrons, and possibly secondary electrons, which are slower and less energetic and may lag behind the measurement. Nevertheless, our data show a high, mathematical correlation with the μ CT data suggesting that the relative contribution of secondary electrons is small. Based on preliminary Monte Carlo simulations of the electron trajectories (Casino v2) for the processing conditions in this study, (e.g., 100mm thick copper plate, 60keV Accelerating Voltage, 10000 electrons, 300 μ m beam radius) the backscattered electrons collected during melt originate from a maximum escape depth of a few microns (6-9 μ m). The escape depth results vary with the model used, parameters, and model assumptions. These values are rough estimates, at best. However, the key point is that the escape depth is significantly smaller than the layer thickness (50 μ m) used in this study and the powder size (48 μ m -114 μ m). Note also that the powder bed confiscates the base assumption of the Casino simulations. This suggests that it is unlikely that the imaging technique can detect sub-surface porosity, and corroborates the calculations reported by Arnold et al. [12], that show the variations in electron signal intensity are related with sample topography. However, the melt pool is not static, nor does it necessarily follow the topography of the preceding melted layers. Depending on the processing conditions,

the melt pool may penetrate a depth several times the layer height into the solid layer previously deposited. This makes TEY imaging during the melt very different from low current raster scanning of a static solid shape or recently solidified layer. As Figure 18 demonstrates, the pool has a wide range of topologies from ripples to significant protrusions, depressions, and liquid ejections as it is influenced by physics such as vapor pressure, beam to powder bed/substrate inconsistencies and charge interactions as other sources of turbulence. These effects may cause depressions in the liquid surface tens to hundreds of microns below the surrounding surfaces and generate a protruding liquid bow wave. Also, the beam is not a point source and has a gaussian power distribution from the center to the edge, which is expected to influence the TEY signal generated. Therefore, the resulting TEY signal likely reflects the instantaneous topology of the melt pool, local substrate density, and the associated loss in signal as the pool either encounters or generates a feature such as a pore that would result in an electron signal loss at that point in time.

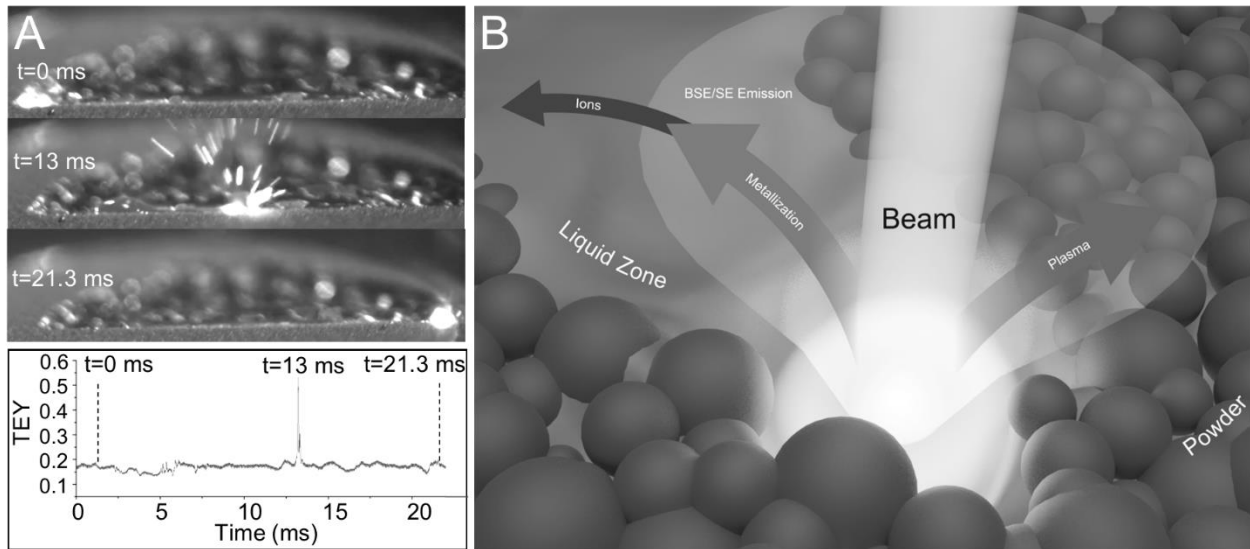


Figure 18: Top surface layer high-speed images recorded at A) $t=0$, $t=13$ sec, $t=21$ sec, and TEY signal generated during high-speed imaging from 0-21 sec and B) Illustration of the EB interaction with powder bed and melt pool

The blurriness in the TEY data arises from several probable sources. First, the binning strategy used to generate the images is itself limited by the beam tool path, which is optimized for melting/productivity as opposed to image resolution. It is important to highlight that while melting, the resolution of TEY images is limited by both the hatch spacing during melting and the sampling frequency. The latter could simply be addressed with improved data acquisition hardware. The quantitative SSIM analysis that we have presented suggests that the location of the defects observed in TEY images correlate well with μ CT data but overestimates defect size. Interestingly it does this in consistent and predictable ways suggesting that resolution may not be the best descriptor of the observed phenomena. The beam diameter, which is often larger than the observed defect ($355 \mu\text{m} \pm 50 \mu\text{m}$, measured using knife-edge method at the beam currents

used in this study), and the Gaussian profile of the beam intensity contribute to the elongation of the TEY signal. As the beam approaches a defect on the scale of a few microns, the TEE sensor will experience a loss of signal intensity across its entire diameter.

Furthermore, as the beam encounters a defect, the beam profile causes the incident energy to increase from the edge to the center and then to decrease again. The net effect produces a ‘smeared’ or lower resolution feature as compared with CT scans. However, this does not imply that the approach is unsuitable for applying TEY signal loss for porosity detection. The challenge instead lies in identifying the most accurate analysis techniques required for the optimized correlation.

4.4.3 Significance and Interpretation of Spatiotemporal Process Maps

The EB-PBF system used in this study applies a predetermined, open-loop control strategy. A hierarchy of functions adjusts and maintains localized energy inputs and global temperatures based upon calculated changes in thermal boundary conditions brought about by variations in part geometry. These functions include, but are not limited to, the speed function (SF), thickness function, and turning points function discussed in this manuscript. These functions are, in turn, driven by a myriad of additional parameters, a few of which have been covered herein as well. The individual contributions and the cumulative effect of these parameters are not always readily transparent to users of EB-PBF technology. Changes in the local energy density implemented by the EB-PBF control, coupled with stochastic variations in the thermophysical properties of the powder bed and deviations in thermal boundary conditions associated with part geometry have presented significant challenges for process planning, material development, microstructure control and AM component qualification [42, 56, 67].

Even minute changes in any one of these conditions can produce a range of microstructures and defects due to changes in the melt pool size [22, 68], geometry [69], and solidification rate, which are difficult to predict and detect in real-time. [70, 71, 19-23].

The methodology that we have presented utilizes real-time beam positional tracking and beam current monitoring concurrently with the electron signals. In this paper, we have elucidated subtle but essential interconnected relationships between the beam speed data in Figures 10-13 and the TEY data, which has been correlated (within the bounds and assumptions of this study) to observed porosity in μ CT data. With the methodology we have described, EB-PBF researchers will be able to visualize localized changes in energy input, as a function of beam speed, position and time throughout the fabrication of a component, and to compare these data with electron signals. We have also demonstrated that any of the collected real-time data streams can be plotted concurrently with time-stamped data from the system logs or external instrumentation to generate 4D spatiotemporal maps (Figure 14) of the component for both visualization and correlation analysis.

For the EB-PBF system used in this study, the most responsive control parameter is beam speed. The primary control functions adjust speed to compensate for changes in current or calculated thermal boundary conditions. Figure 11 illustrates how the turning points function increases beam speed at the sample edges based on the assigned speed function (SF) and input current to reduce the local energy input. However, the turning points function is an open-loop control parameter, and the precise thermal boundary conditions at the part/powder bed interface are not known. The concurrent electron signals and images provide insight into whether the turning points function is performing properly or needs to be adjusted. The data from the overhang experiments shown in Figure 12 illustrates the change in beam speed in the downward-

facing region of a component associated with changes in the thickness function parameters of thickness factor (T_f) and speed factor (S_f). Again the effect of an incremental change in a given parameter is not easily deciphered, in part because the functions are not explicitly known to users, but also because the various functions are nested and interconnected. A change in one parameter of a function may shift the value or change the magnitude of the effect of another. Collectively, this makes it very difficult to quickly and precisely target melt parameters under a variety of geometries and conditions. As Figure 11C and 11D show, the TEY data provide near real-time feedback on the influence that parameter changes have on part properties. Traditionally, this would require a significant number of experiments and analyses such as x-ray μ CT or metallurgical sample sectioning, preparation, and microscopy. (similar to that shown Figure 12E).

The ability to extract spatiotemporal process data coupled with electron signals also allows us to explore process parameter space mapping differently and with a new set of tools. Because of the complexity of the parameters and their interactions, material development studies using EB-PBF are often conducted with the automatic control functions disabled. Geometries are often oriented parallel or perpendicular to the beam trajectory to hold scan line length constant. This is indeed the case for the processing space for pure copper extracted from the literature [30-32, 37,45] shown in Figure 13A. While these data are inherently valuable, they suggest an overly simplified view of the optimal processing space. Still, without the appropriate tools to fully explore the influence of various parameters and geometric conditions, it is difficult to provide any conclusive data beyond this. However, when the selected data (for clarity) from our study are overlaid onto Figure 13A, they show a wide range of energy density values are present within a build. This is a direct result of the open-loop control system attempting to

maintain a constant melt pool size for changing conditions associated with overhangs and other geometrical features (subject to the input parameters used). The ability to analyze parameter data spatially and correlate it (TEY, speed, current, etc.) to defects such as porosity provides a new tool for better understanding the EB-PBF process and the effects on the solid articles fabricated.

4.4.4 Proof of Concept for EB-PBF Process Control

The real-time nature of the data acquisition methodology we have presented, which inherently couples spatiotemporal process data with real-time TEY data, suggests a potential future pathway for real-time process control. Such a study is well outside the scope of this manuscript. Nevertheless, we have presented a rudimentary control algorithm, and have demonstrated a simple experiment as a proof of concept. It is, therefore, neither optimized nor comprehensive. Although beam speed is a more responsive parameter, most users do not have direct, real-time access to modify it. For this reason, the beam current was selected as the control parameter for the demonstration. Because the response time for beam current is relatively slow (compared to beam speed), the control strategy is implemented between layers and is based on the average TEY value for a given layer. The control loop shown in Figure 3 illustrates how the high voltage power supply controller's demanded beam current is modified based on whether the average TEY signal is above or below a predefined threshold. The original signal was returned to the high voltage current feedback port on the PLC to prevent the Arcam control system from compensating for our implemented control. As a result, the porosity that was intentionally induced in the test specimen was entirely eliminated within just a few millimeters (Figure 16). This configuration is far from ideal but does serve to illustrate the potential for interpreting and utilizing the TEY signals to accomplish a mathematically determined process adjustment. With

the tools we have presented, one could conceive of many possible approaches to process control and new materials development. Although not attempted directly here, with the appropriate algorithm, one could speculate rapidly screening through a plurality of process parameters to home in on the feasible processing space for a new material automatically. The value proposition of this approach will hinge upon both the interpretation of the massive quantity of data generated per component (>0.5TB for the CCTWT build shown in Figure 14), as well as the ability to correlate anomalous features smaller than the beam to identify defect formation and implement preventative control actions in real-time.

4.4.5 Other Observed Limitations of the Methodology and Alternative Solutions

A fundamental feature of our methodology that enables monitoring across multiple layers, and for arbitrary geometries that distinguishes it from previous work is the near real-time monitoring of multiple data streams to normalize and interpret beam position and power. It is essential, therefore, to discuss to current limitations of this approach. We have monitored and inferred the beam power from the HV feedback signal rather than direct measurement (e.g., ISO 14744-2). In our preliminary experiments, the TEE signal was normalized against the grid voltage feedback (since the flow of current from the electron gun to the powder bed surface is regulated using a control electrode). However, the grid voltage feedback signal proved to fluctuate significantly. Drift in the grid voltage was observed over time, presumably to compensate for filament condition, but we also observed a $\sim \pm 2\text{-}3\%$ sinusoidal fluctuation. The magnitude of the fluctuation also appeared to be proportional to the beam current. For these reasons, the use of the grid voltage feedback monitoring to normalize TEE was abandoned in this study in favor of the HV feedback signal. Figure 19 shows both the grid voltage feedback signal

and the HV feedback signal for the same prismatic components used in this study, at varying beam currents and over multiple layers. Note that the grid voltage feedback is inversely proportional to the beam current. The ISO 14744-2 direct measurement method would be preferable from the standpoint of precision. However, it would require significant modification to the OEM system hardware.

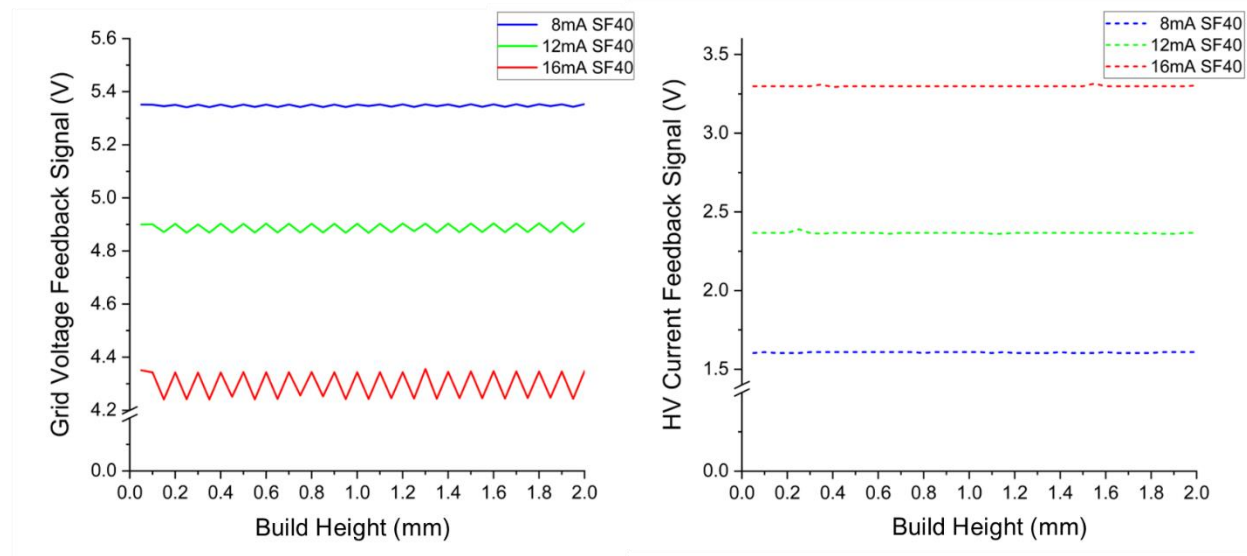


Figure 19: Grid voltage feedback signal (left) and HV current feedback signal (right) for multiple layers of samples produced in this study at 8 mA, 12 mA, and 16 mA beam currents.

Interpretation is further complicated by the fact that, in our study, beam positions are monitored by the PLC feedback positions, and not by an external decoupled source. Ideally, positions would be monitored with external field measurements. Because we are monitoring the deflection coil feedback signal, we can validate that the beam was indeed moved to the programmed position subject to the accuracy of the system calibration. The system is, however, open loop, so the detector is not capable of identifying changes in position induced by external

magnetic fields. This is a common issue encountered in EB systems, where local changes in the magnetic field (e.g., moving carts, elevators, cycling of nearby high voltage transformers) [1, 72], can cause the beam to shift from its calibrated position. In an extreme example, to perturb our methodology during a run, a small permanent magnet (9.52 mm diameter x 9.52 mm cylindrical neodymium rare earth magnet, N42) was placed on the side of the electron beam column near one of the deflection coil poles. As shown in Figure 20, this had the effect of shifting the beam several mm. While the TEY data clearly show that loss of signal in this region, because positions are monitored internally, it does not register the geometric change in the generated images. For the same reasons, the methodology, as we have described it, is not suitable for in-situ geometric measurements of the AM components. However, although not demonstrated here, one could imagine a myriad of post-layer TEE imaging strategies to rapidly sample and assess geometric accuracy or powder bed conditions (e.g., streaks, pits, waviness, etc.). The TEE signal intensity is also influenced by the movement of components within the chamber, for instance opening the viewport will result in a slight shift in overall TEY due to the change in the system charge state.

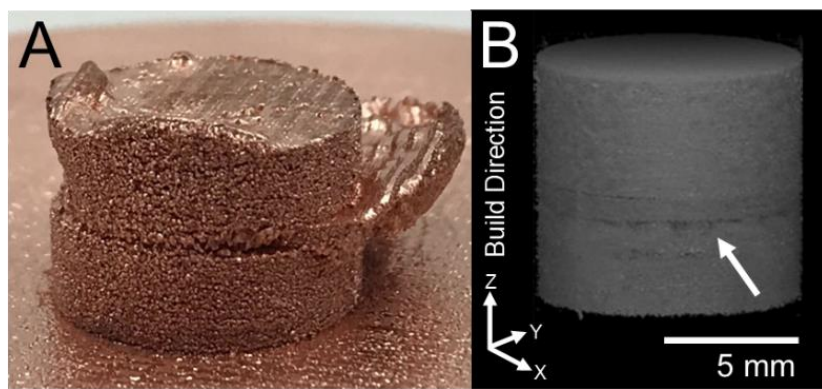


Figure 20: Photograph of the pure copper build, which experienced a beam shift induced by an external magnetic field (A), and TEY data map showing the loss of signal associated with the beam shift in the same nominal layer location (B).

4.5 Summary and Conclusions

The methodology and results presented in this study provide the details for other researchers to fabricate and utilize an electron detector capable of real-time spatiotemporal monitoring, mapping, and control of the electron beam powder bed process, without the need for post melt scanning or any intrusion into the melt process throughout a build, regardless of part geometry. It also demonstrates a methodology to connect process data from a wide variety of sources to access build quality of fabricated articles. By joining TEY data collected from melting, beam position, externally measured data (temperature, filament current, etc.), in situ imaging (high-speed camera), PLC data, and traditional post melt characterization (μ CT, optical images) a new way of approaching EB-PBF AM is available to researchers.

A summary of observations made over the course of this research are:

1. The methodology for a split plate electron sensor and circuitry is presented. The sensor is capable of supporting electron image generation during EB-PBF AM in topographical and compositional modes.
2. The electron signal may be acquired at any time that the electron beam is interacting with the powder bed. In this manuscript, we demonstrate signal acquisition during the melting step and throughout multiple layers.
3. Electron image generation through multiple layers was facilitated by normalizing the TEE signal against the incident beam current (approximated from the HV power supply beam current feedback signal to generate the TEY (total electron yield) signal.

4. Electron signals from the melting step of prismatic specimens were collected in real-time.

Regions of reduced TEY signal intensity were mathematically correlated to porosity in the same EB-PBF specimens observed by optical microscopy and x-ray μ CT using MAPE and SSIM techniques. This was done for every layer, throughout the z-height of each specimen. SSIM images indicate a strong correlation between the X-Y position of observed porosity in x-ray μ CT and TEY images. TEY images acquired during melting are blurry compared to x-ray μ CT. This is hypothesized to be related to the beam path during melting, the binning strategy and the Gaussian intensity profile of the beam, all of which are quantifiable.

5. The beam position in X and Y was also tracked in real-time by monitoring the PLC input

ports for the system X and Y deflection cards at 100kHz sampling frequency. This facilitates two key advancements. First that the in-situ electron imaging can be conducted, regardless of component geometry or beam trajectory. This is demonstrated for a complex component (CCTWT) and for spot melting of part contours. Second, the collection of the beam positional data allows the calculation of key process variables such as beam speed, beam/melt track trajectory, and sample melt order. The methodology also provides insight into beam speed changes implemented by EB-PBF control functions such as the speed function, the turning points function, or the thickness function. This was demonstrated for a prismatic geometry, an overhang geometry, and a representative complex demonstration component (CCTWT device).

6. Combining the beam speed and beam current data streams facilitates 4D spatiotemporal maps of part geometries showing the measured/calculated local variations in energy input resulting from the system control functions and parameters. These maps are overlayed with the TEY data to provide real-time feedback on the effect of variations in local energy inputs on porosity. It was then demonstrated that these data could be mapped against any available time-stamped data streams, such as the system log file data or external sensor data (e.g., thermocouple), to visualize correlations between and these data streams, TEY and process parameters/energy inputs.

7. The concurrent collection data streams related to local energy input (position, beam speed, and beam current) and TEY data, which has been mathematically correlated to process defects (porosity), opens the possibility for real-time control strategies. As a proof of concept, in this manuscript, we present a rudimentary control system to eliminate porosity by increasing beam current between layers, which opens the door for new control strategies in AM.

4.6 References

1. Reimer, L. (2013). Scanning electron microscopy: physics of image formation and microanalysis (Vol. 45). Springer.
2. Petrov, P., Georgiev, C., & Petrov, G. (1998). Experimental investigation of weld pool formation in electron beam welding. *Vacuum*, 51(3), 339-343.
3. Ardenne, T. V., & Panzer, S. (1983). Electron backscattering for process control in electron beam welding. *Elektric*, 37(3), 137-139.
4. Hiramoto, S., Ohmine, M., & Sakamoto, M. (1991). Development of an automatic beam focus system for electron beam welding. *Welding international*, 5(10), 763-768.
5. Fritz, D. (1997). Seam tracking and positioning for electron beam welding. *Welding in the World/Le Soudage dans le Monde*, 6(39), 331-344.
6. Petrov, P., Petrov, G., Petrova, J., & Georgiev, C. (2006). Control of the weld pool formation during electron beam welding dissimilar materials. In 7th international conference on advanced manufacturing operations, Sozopol.
7. Dossett, J., & Totten, G. E. (2013). Electron Beam Surface Hardening. ASM international.
8. Taminger, K. M., Domack, C. S., Zalameda, J. N., Taminger, B. L., Hafley, R. A., & Burke, E. R. (2016, May). In-process thermal imaging of the electron beam freeform fabrication process. In Thermosense: Thermal Infrared Applications XXXVIII (Vol. 9861, p. 986102). International Society for Optics and Photonics.
9. Pobel, C. R., Arnold, C., Osmanlic, F., Fu, Z., & Körner, C. (2019). Immediate development of processing windows for selective electron beam melting using layerwise monitoring via backscattered electron detection. *Materials Letters*, 249, 70-72.

10. Arnold, C., Pobel, C., Osmanlic, F., & Körner, C. (2018). Layerwise monitoring of electron beam melting via backscatter electron detection. *Rapid Prototyping Journal*, 24(8), 1401-1406.
11. Arnold, C., Osmanlic, F., Pobel, C., Wormser, M., & Körner, C. (2018). Enhanced process control during selective electron beam melting through advanced machine technology. "E+E", vol. 53, 3-4, 2018
12. Arnold, C., Böhm, J., & Körner, C. (2019). In-operando Monitoring by Analysis of Backscattered Electrons during Electron Beam Melting. *Advanced Engineering Materials*.
13. Wong, H., Neary, D., Shahzad, S., Jones, E., Fox, P., & Sutcliffe, C. (2019). Pilot investigation of feedback electronic image generation in electron beam melting and its potential for in-process monitoring. *Journal of Materials Processing Technology*, 266, 502-517.
14. Wong, H., Neary, D., Jones, E., Fox, P., & Sutcliffe, C. (2019). Pilot capability evaluation of a feedback electronic imaging system prototype for in-process monitoring in electron beam additive manufacturing. *The International Journal of Advanced Manufacturing Technology*, 100(1-4), 707-720.
15. Wong, H., Neary, D., Jones, E., Fox, P., & Sutcliffe, C. (2019). Benchmarking spatial resolution in electronic imaging for potential in-situ Electron Beam Melting monitoring. *Additive Manufacturing*, 29, 100829.
16. Wong, H., Neary, D., Jones, E., Fox, P., & Sutcliffe, C. (2019). Pilot feedback electronic imaging at elevated temperatures and its potential for in-process electron beam melting monitoring. *Additive Manufacturing*, 27, 185-198.

17. Wong, H., Garrard, R., Black, K., Fox, P., & Sutcliffe, C. (2019). Material characterisation using electronic imaging for Electron Beam Melting process monitoring. *Manufacturing Letters*.
18. Wang, J., Yin, B., Xu, G., Liu, J., Wang, Y., & Han, L. (2019, August). Research on image monitoring method of electron beam selection melting. In IOP Conference Series: Materials Science and Engineering (Vol. 592, No. 1, p. 012153). IOP Publishing
19. Dehoff, R. R., Kirka, M. M., Sames, W. J., Bilheux, H., Tremsin, A. S., Lowe, L. E., & Babu, S. S. (2015). Site specific control of crystallographic grain orientation through electron beam additive manufacturing. *Materials Science and Technology*, 31(8), 931-938.
20. Raghavan, N., Simunovic, S., Dehoff, R., Plotkowski, A., Turner, J., Kirka, M., & Babu, S. (2017). Localized melt-scan strategy for site specific control of grain size and primary dendrite arm spacing in electron beam additive manufacturing. *Acta Materialia*, 140, 375-387.
21. Raghavan, N., Dehoff, R., Pannala, S., Simunovic, S., Kirka, M., Turner, J., ... & Babu, S. S. (2016). Numerical modeling of heat-transfer and the influence of process parameters on tailoring the grain morphology of IN718 in electron beam additive manufacturing. *Acta Materialia*, 112, 303-314.
22. Dehoff, R. R., Kirka, M. M., List, F. A., Unocic, K. A., & Sames, W. J. (2015). Crystallographic texture engineering through novel melt strategies via electron beam melting: Inconel 718. *Materials Science and Technology*, 31(8), 939-944.
23. Plotkowski, A., Kirka, M. M., & Babu, S. S. (2017). Verification and validation of a rapid heat transfer calculation methodology for transient melt pool solidification

- conditions in powder bed metal additive manufacturing. *Additive Manufacturing*, 18, 256-268.
24. White, E., Rinko, E., Prost, T., Horn, T., Ledford, C., Rock, C., & Anderson, I. (2019). Processing of Alnico Magnets by Additive Manufacturing. *Applied Sciences*, 9(22), 4843.
25. Ledford, C., Rock, C., Carriere, P., Frigola, P., Gamzina, D., & Horn, T. (2019). Characteristics and Processing of Hydrogen-Treated Copper Powders for EB-PBF Additive Manufacturing. *Applied Sciences*, 9(19), 3993.
26. Cohen, A J, and K F Koral. "Backscattering and Secondary-Electron Emission from Metal Targets of Various Thicknesses," n.d., 36.
27. Narra, S. P., Cunningham, R., Beuth, J., & Rollett, A. D., Location specific solidification microstructure control in electron beam melting of Ti-6Al-4V. *Additive Manufacturing* (2018), 19, 160-166.
28. Wang, Z., Bovik, A. C., Sheikh, H. R., & Simoncelli, E. P. (2004). Image Quality Assessment: From Error Visibility to Structural Similarity. *IEEE Transactions on Image Processing*, 13(4), 600–612.
29. Swamidass, P. M. (Ed.). (2000). Encyclopedia of production and manufacturing management. mean absolute percentage error (mape). Springer Science & Business Media.
30. Lodes, M. A., Guschlbauer, R., & Körner, C. (2015). Process development for the manufacturing of 99.94% pure copper via selective electron beam melting. *Materials Letters*, 143, 298-301.

31. Raab, S. J., Guschlbauer, R., Lodes, M. A., & Körner, C. (2016). Thermal and electrical conductivity of 99.9% pure copper processed via selective Electron beam melting. *Advanced Engineering Materials*, 18(9), 1661-1666.
32. Guschlbauer, R., Momeni, S., Osmanlic, F., & Körner, C. (2018). Process development of 99.95% pure copper processed via selective electron beam melting and its mechanical and physical properties. *Materials Characterization*, 143, 163-170.
33. Smith, C. J., Derguti, F., Nava, E. H., Thomas, M., Tammas-Williams, S., Gulizia, S., ... & Todd, I. (2016). Dimensional accuracy of Electron Beam Melting (EBM) additive manufacture with regard to weight optimized truss structures. *Journal of Materials Processing Technology*, 229, 128-138.
34. Patino, M. I., Raitses Y., Koel B. E. and Wirz R.E. “Analysis of secondary electron emission for conducting materials using 4-grid LEED/AES optics” *Journal of Physics D: Applied Physics*, Volume 48, Number 19
35. Arnaud de M., Golden B., Le Grand B., and Rossi F.. “Mean Absolute Percentage Error for Regression Models.” *Neurocomputing, Advances in artificial neural networks, machine learning and computational intelligence*, 192 (June 5, 2016): 38–48
36. Ummul K., Fahmi H., Al Hakim S., and Robbi Rahim. “Forecasting Error Calculation with Mean Absolute Deviation and Mean Absolute Percentage Error.” *Journal of Physics: Conference Series* 930 (December 2017): 012002
37. T. Horn and D. Gamzina, Additive Manufacturing of Copper and Copper Alloys, ASM Handbook Volume 24, Additive Manufacturing Processes, ASM International, to be published 2020.

38. Schwerdtfeger, J., Singer, R. F., & Körner, C. (2012). In situ flaw detection by IR-imaging during electron beam melting. *Rapid Prototyping Journal*.
39. Bauereiß, A., T. Scharowsky, and C. Körner. "Defect Generation and Propagation Mechanism during Additive Manufacturing by Selective Beam Melting." *Journal of Materials Processing Technology* 214, no. 11 (November 1, 2014): 2522–28
40. Mahale, T. R. (2009). Electron beam melting of advanced materials and structures. North Carolina State University.
41. W. E. King, A. T. Anderson,, R. M. Ferencz, N. E. Hodge, C. Kamath, S. A. Khairallah, and A. M. Rubenchik, Laser powder bed fusion additive manufacturing of metals; physics, computational, and materials challenges *Applied Physics Reviews* 2, 041304 (2015).
42. Kirka, M.M., Lee, Y., Greeley, D.A. , Okello A., Goin, A.J. Pierce, M.T. , Dehoff, R.R., Strategy for Texture Management in Metals Additive Manufacturing, *JOM* (2017) 69: 523
43. Narra, Sneha, Ross Cunningham, Daniel Christiansen, Jack Beuth and Anthony D. Rollett, Toward Enabling Spatial Control of Ti-6Al-4V Solidification Microstructure in the Electron Beam Melting Process, *Solid Freeform Fabrication* (2015)
44. Yoder, S., P. Nandwana, V. Paquit, M. Kirka, A. Scopel, R. R. Dehoff, and S. S. Babu. Approach to Qualification Using E-PBF in-Situ Process Monitoring in Ti-6Al-4V. *Additive Manufacturing* 28 (August 1, 2019): 98–106.
45. Frigola, P., Harrysson, O., Horn, T., West, H., Aman, R., Rigsbee, J., & Rodriguez, E. (2014). Fabricating copper components. *Advanced Materials & Processes*, 20.

46. Lomakin, K., Guschlbauer, R., Osmanlic, F., Fu, Z., Sippel, M., Helmreich, K., ... & Gold, G. (2019, October). 3D printed copper waveguides by selective electron beam melting process for E-band. In 2019 49th European Microwave Conference (EuMC) (pp. 774-777). IEEE.
47. Gamzina, D., Luhmann, N. C., Ledford, C., Horn, T., Karakaut, I., Lin, L., & Frigola, P. (2017, April). Additive vacuum electronics: Electron beam melting of copper. In 2017 Eighteenth International Vacuum Electronics Conference (IVEC) (pp. 1-2). IEEE.
48. Horn, T., Karakurt, I., Ledford, C., Gonzalez, M., Gamzina, D., Luhmann, N. C., & Lin, L. (2018, April). Additively manufactured WR-10 copper waveguide. In 2018 IEEE International Vacuum Electronics Conference (IVEC) (pp. 409-410). IEEE.
49. Ives, R. L., Marsden, D., Horn, T., Ledford, C., & Rock, C. (2018). Klystron Fabrication Using Additive Manufacturing In 2018 IEEE International Vacuum Electronics Conference (IVEC) (pp. 409-410). IEEE.
50. Frigola, P., Agustsson, R., Faillace, L., Rimmer, R., Clemens, W., Henry, J., ... & Knowlson, K. (2010, October). Development of a CW NCRF Photoinjector using solid freeform fabrication (SFF). In Conf. Proc. (Vol. 100523, No. IPAC-2010-THPEA057, p. THPEA057)
51. Ramirez, D. A., Murr, L. E., Martinez, E., Hernandez, D. H., Martinez, J. L., Machado, B. I., ... & Wicker, R. B. (2011). Novel precipitate–microstructural architecture developed in the fabrication of solid copper components by additive manufacturing using electron beam melting. *Acta Materialia*, 59(10), 4088-4099.
52. Körner, C., Attar, E., & Heinl, P. (2011). Mesoscopic simulation of selective beam melting processes. *Journal of Materials Processing Technology*, 211(6), 978-987.

53. Ammer, R., Markl, M., Ljungblad, U., Körner, C., & Rüde, U. (2014). Simulating fast electron beam melting with a parallel thermal free surface lattice Boltzmann method. *Computers & Mathematics with Applications*, 67(2), 318-330.
54. Markl, M., & Körner, C. (2018). Powder layer deposition algorithm for additive manufacturing simulations. *Powder technology*, 330, 125-136.
55. Slotwinski, J. A. (2014, February). Additive manufacturing: Overview and NDE challenges. In *AIP Conference Proceedings* (Vol. 1581, No. 1, pp. 1173-1177). American Institute of Physics.
56. Babu, S. S., Raghavan, N., Raplee, J., Foster, S. J., Frederick, C., Haines, M., ... & Dehoff, R. R. (2018). Additive manufacturing of nickel superalloys: opportunities for innovation and challenges related to qualification. *Metallurgical and Materials Transactions A*, 49(9), 3764-3780.
57. Thompson, Adam & Maskery, Ian & Leach, Richard. (2016). X-ray computed tomography for additive manufacturing: A review. *Measurement Science and Technology*. 27. 072001. 10.1088/0957-0233/27/7/072001.
58. De Chiffre L, Carmignato S, Kruth J-P, Schmitt R and Weckenmann A 2014 Industrial applications of computed tomography *CIRP Ann. Manuf. Techn.* 63 655-77
59. Faïdel, D., Jonas, D., Natour, G., & Behr, W. (2015). Investigation of the selective laser melting process with molybdenum powder. *Additive Manufacturing*, 8, 88-94.
60. Wang, D., Yu, C., Ma, J., Liu, W., & Shen, Z. (2017). Densification and crack suppression in selective laser melting of pure molybdenum. *Materials & Design*, 129, 44-52.

61. Ivezković, A., Omidvari, N., Vrancken, B., Lietaert, K., Thijs, L., Vanmeensel, K., ... & Kruth, J. P. (2018). Selective laser melting of tungsten and tungsten alloys. International Journal of Refractory Metals and Hard Materials, 72, 27-32.
62. Müller, A. V., Schlick, G., Neu, R., Anstätt, C., Klimkait, T., Lee, J., ... & Seidel, C. (2019). Additive manufacturing of pure tungsten by means of selective laser beam melting with substrate preheating temperatures up to 1000° C. Nuclear Materials and Energy, 19, 184-188.
63. Tan, C., Zhou, K., Ma, W., Attard, B., Zhang, P., & Kuang, T. (2018). Selective laser melting of high-performance pure tungsten: parameter design, densification behavior and mechanical properties. Science and Technology of advanced MaTerialS, 19(1), 370-380.
64. Terrazas, C. A., Mireles, J., Gaytan, S. M., Morton, P. A., Hinojos, A., Frigola, P., & Wicker, R. B. (2016). Fabrication and characterization of high-purity niobium using electron beam melting additive manufacturing technology. The International Journal of Advanced Manufacturing Technology, 84(5-8), 1115-1126
65. Wong, H., Garrard, R., Black, K., Fox, P., & Sutcliffe, C. (2020). Material characterisation using electronic imaging for Electron Beam Melting process monitoring. Manufacturing Letters, 23, 44-48. doi:10.1016/j.mfglet.2019.12.005
66. Brooks, A.J., Ge, J., Kirka, M.M. et al. Porosity detection in electron beam-melted Ti-6Al-4V using high-resolution neutron imaging and grating-based interferometry. Prog Addit Manuf 2, 125–132 (2017). <https://doi.org/10.1007/s40964-017-0025-z>
67. Lunetto, V., Galati, M., Settineri, L., & Iuliano, L. (2020). Unit process energy consumption analysis and models for Electron Beam Melting (EBM): Effects of process and part designs. Additive Manufacturing, 33, 101115. doi:10.1016/j.addma.2020.101115

68. Nandwana, P., & Lee, Y. (2020). Influence of Scan Strategy on Porosity and Microstructure of Ti-6Al-4V Fabricated by Electron Beam Powder Bed Fusion. *Materials Today Communications*, 100962.
69. Lee, Y.S., Kirka, M.M., Ferguson, J. and Paquit, V.C., 2020. Correlations of Cracking with Scan Strategy and Build Geometry in Electron Beam Powder Bed Additive Manufacturing. *Additive Manufacturing*, p.101031.
70. Raplee, J., Plotkowski, A., Kirka, M. M., Dinwiddie, R., Okello, A., Dehoff, R. R., & Babu, S. S. (2017). Thermographic microstructure monitoring in electron beam additive manufacturing. *Scientific reports*, 7, 43554.
71. Fezi, K., Plotkowski, A., & Krane, M. J. (2016). A metric for the quantification of macrosegregation during alloy solidification. *Metallurgical and Materials Transactions A*, 47(6), 2940-2951.
72. Laptenok, V. D., Druzhinina, A. A., Murygin, A. V., & Seregin, Y. N. (2016, April). Method to eliminate the impact of magnetic fields on the position of the electron beam during EBW. In *IOP Conference Series: Materials Science and Engineering* (Vol. 122, No. 1, p. 012021). IOP Publishing.

Funding

This research was partially funded by the Navy Sea Systems Command Contract Number N0025316P0261. This research was also partially funded by DARPA INVEST, program N66001-16-1-4044, and the Center for Additive Manufacturing and Logistics, North Carolina State University.

Acknowledgments

This work was performed in part at the Analytical Instrumentation Facility (AIF) at North Carolina State University, which is supported by the State of North Carolina and the National Science Foundation (award number ECCS-1542015). The AIF is a member of the North Carolina Research Triangle Nanotechnology Network (RTNN), a site in the National Nanotechnology Coordinated Infrastructure (NNCI). High speed videos were acquired with the assistance of Dr. Mark Pankow and the Ballistic Loading and Structural Testing Lab (BLAST), Department of Mechanical and Aerospace Engineering, NC State University.

CHAPTER 5: Future Work: Layer by Layer Hydrogen Treatment of Copper Powder during EB-PBF Additive Manufacturing

5.1 Introduction

Utilizing the results from the hydrogen heat treatment of the precursor powder, the idea that we could implement a similar treatment on a layer by layer basis during the fabrication process was conceived. By repurposing the controlled vacuum capability of the Arcam system, we can create a reducing atmosphere of our choosing during the melting process. This would allow for the use of a lower quality copper powder feedstock containing higher oxygen content than desirable in the final product. This higher oxygen content would exist as surface oxide on the particles due to handling and sieving which ultimately help with spreadability. By establishing an initial pressure of $3.75e^{-5}$ Torr in the vacuum chamber, a reducing gas is introduced using pressure controlled valves. Using pure hydrogen gas, a system pressure of roughly $7.5e^{-3}$ Torr would provide roughly 10 times the required hydrogen molecules for the reduction of a single powder layer assuming an oxygen content of 75 ppm wt. The oxygen in the powder is assumed to only exist in the particle as a surface oxide as the solid solubility of oxygen in copper is less than 2 ppm wt. Equation 1 shows the reduction reaction of Cu₂O with hydrogen gas to form metallic copper and H₂O.



This reduction would begin to occur as the powder is spread across the heated surface of the build. Reduction will continue to occur during the preheating step where quickly rastering the unfocused electron beam will raise the surface temperature of the powder bed to between 550-

600°C. Currently the preheating step takes ~30 seconds for a 40 um layer thickness. At these temperatures, the diffusion rate of hydrogen in solid copper is roughly 5000 $\mu\text{m}^2/\text{s}$ which corresponds to a diffusion time of 30 milliseconds to the center of a 35 μm diameter particle. Literature shows that the rate of reduction of Cu₂O significantly increases with increasing temperature [1]. At temperatures exceeding 300°C, reduction of Cu₂O should begin immediately and fully reduce in a short time span. H₂O created during the reduction reaction would then be evacuated from the system as more hydrogen gas is added for continued reduction.

5.2 Methodology

In order to determine the feasibility of reducing the surface oxides from a single layer of powder, the onset and total reduction time at the suggested preheat temperature range of 550-600°C and hydrogen partial pressure needs further investigation. Utilizing a controlled environment stage capable of sustaining a low hydrogen partial pressure, high temperature x-ray diffraction (XRD) will be used to determine the onset and total reduction time Cu₂O powders with a d₅₀ of 35 μm . The powders will be heated to the desired temperature under a pure nitrogen environment to ensure no further oxidation or reduction occurs. A mix of 3% hydrogen balanced nitrogen gas will be introduced once the temperature has stabilized to initiate the reduction process. In order to determine when the copper oxide has been reduced, a single Cu₂O peak (111) will be continuously scanned every 5 seconds. From this data, a reduction rate of the peak intensity as function of time can be experimentally determined.

For EB-PBF implementation, a slight modification to the controlled vacuum system will be necessary. In order to ensure that the hydrogen atoms from the controlled vacuum are

concentrated to the surface of the current build layer, the gas will be routed through a perforated ring constructed from stainless steel tubing and suspended slightly above the build surface. The controlled vacuum valve will be relocated from the rear of the Arcam system to one of three additional feedthroughs located on top of the vacuum chamber which allows for direct line of sight to the build surface. Initial testing to determine if reduction is occurring under normal EBM processing conditions will consist of preheating small pressed discs of pure copper powder with oxygen contents around 500 ppm wt. Oxygen and hydrogen content of the sintered powder will be measured using inert gas fusion analysis as described earlier.

5.3 Results and Discussion

Initial results from the 600°C hold high temperature x-ray study are shown in Figure 1.

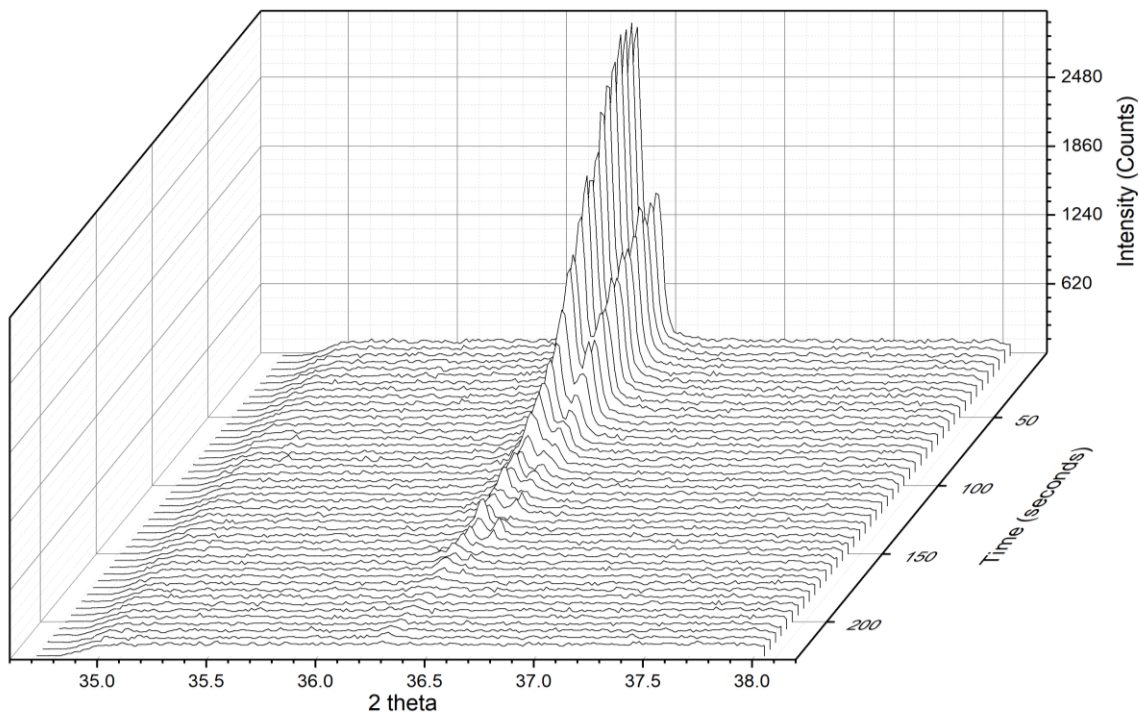


Figure 1: 2Θ as a function of time of the Cu_2O (111) peak at a holding temperature of 600°C in a reducing atmosphere

The Cu₂O (111) peak starts diminishing very quickly within the first 100 seconds and appears to disappear after only 180 seconds. With this being pure Cu₂O powder instead of pure copper powder with an oxide shell, the rapid decrease in the peak intensity shows that the reduction is happening extremely quickly on the surface of the particles as hydrogen diffuses inward. This shows promise as these are time scales and temperature regimes that mimic what a typical preheat could look like for copper during the EB-PBF process.

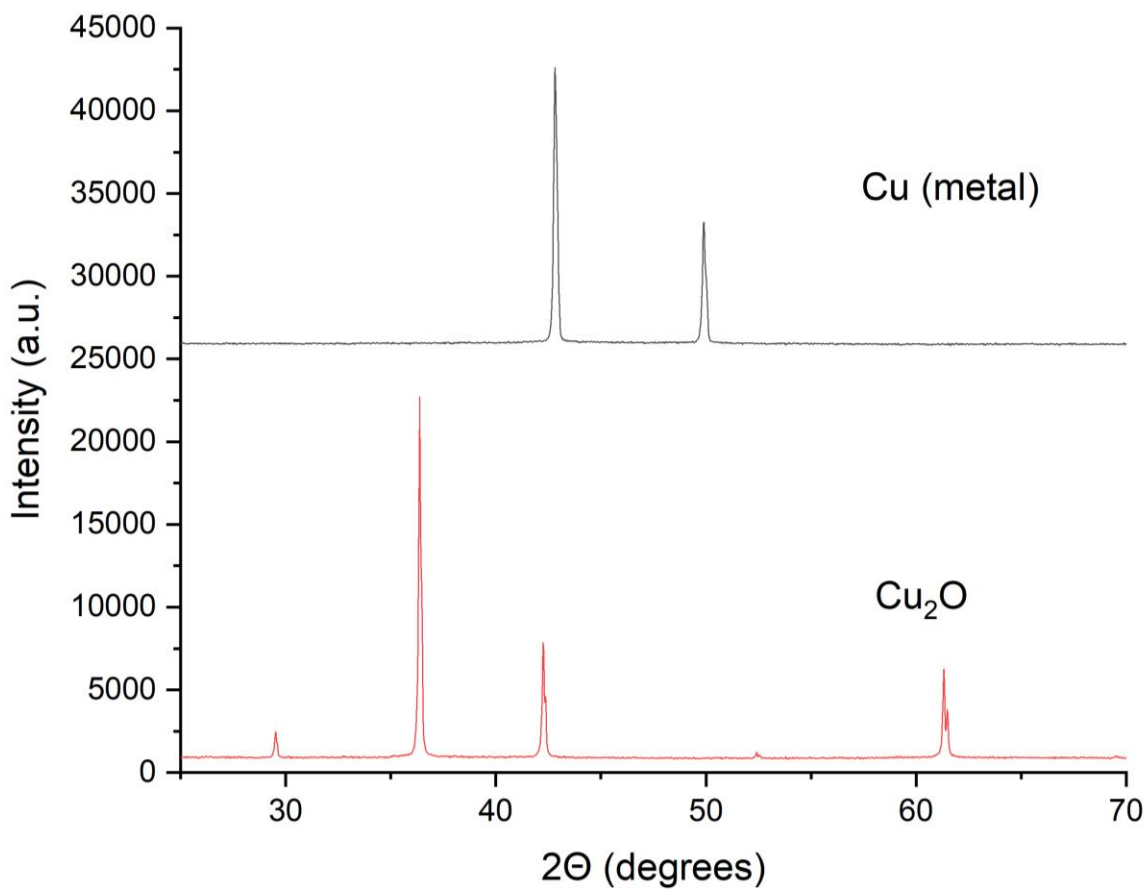


Figure 2: XRD of the precursor Cu₂O powder (bottom) and the resulting pure copper powder (top) after the hydrogen heat treatment

Figure 2 shows that the precursor Cu₂O powder has fully been reduced to pure copper after the hydrogen heat treatment. More precise oxygen content measurements were not obtainable due to the low quantity of powder treated. Therefore, a small amount of oxygen could still be left in the powder.

With favorable results from the high temperature XRD tests, steps were taken to replicate the process in the EB-PBF system. Figure 3 shows the stainless steel perforated ring used to introduce a 5% hydrogen balanced argon gas into the system byway of the controlled vacuum system.

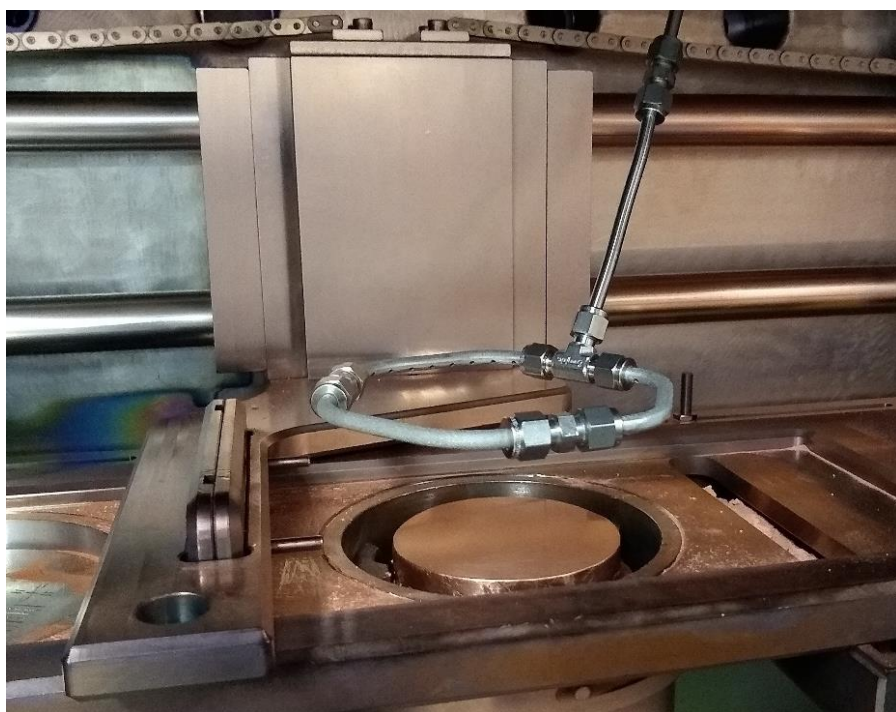


Figure 3: Stainless steel perforated ring used to introduce gas into the EB-PBF system

The ring sits about 50 mm above the build surface to account for the rake movement from side to side. Initial tests consisted of preheating small pressed discs of pure copper powder with approximately 500 ppm wt. oxygen, mostly present as surface oxide. These tests showed little to

no effect on the oxygen content of the powder indicating no reduction was occurring as intended. It is believed to be caused by two issues, the first being that the ring itself is too far away from the powder surface therefore the hydrogen can not interact with the powder before being removed by the vacuum pumps. Secondly, the gas used was only 5% hydrogen due to safety concerns with the pumps and seals and therefore the intended amount of hydrogen was not being introduced into the system.

5.4 Conclusions

High temperature XRD results show promise for the rapid reduction of copper oxide at the time scales and temperatures during the fabrication process. Initial testing however showed that further refinement of the setup is necessary to replicate the same conditions found in the high temperature XRD environment. By bringing the gas outlets closer and increasing the hydrogen concentration, it should be possible to increase the local concentration above the build surface and start the reduction process.

5.5 References

- [1] J. Y. Kim, J. A. Rodriguez, J. C. Hanson, A. I. Frenkel, and P. L. Lee, “Reduction of CuO and Cu₂O with H₂: H Embedding and Kinetic Effects in the Formation of Suboxides,” *J. Am. Chem. Soc.*, vol. 125, no. 35, pp. 10684–10692, Sep. 2003.

CHAPTER 6: Conclusions

The work presented here begins to help overcome some of the limitations in implementing additive manufacturing in not only the production of RF components but any component that would benefit from the enhanced properties of pure copper. With finer surface finishes and lower oxygen contents in the fabricated parts, engineers could begin to leverage the added benefits of additive manufacturing and apply them to new and challenging applications requiring pure copper components.

By achieving low oxygen content in these copper components, they are capable of withstanding hydrogen brazing cycles which would allow them to be used in conjunction with traditional components and practices. With the significant reduction in the as fabricated surface roughness, post finishing may not be necessary if comparable or greater improvements in the RF performance can come from greater flexibility in part geometry. With that said, a combination of post processing and design enhancements could lead to significant RF property improvements.

With the ability to use the hydrogen heat treatment on high oxygen content precursor powder, multiple types of feedstock material could be utilized without the need for specialized handling and screening to ensure low oxygen content. By implementing a layer by layer hydrogen reduction approach, the need to preprocess the powder could be eliminated altogether.

Never before have we had such insight into the fabrication of a part that we do with the layer by layer nature of additive manufacturing. By implementing in-situ monitoring solutions, we can start to assure the quality of these low production parts during the fabrication process. Also by detecting possible defects during fabrication in real time, these could be ultimately be used in a closed loop control system. Further working to assure the final fabricated part is to the highest standard.

APPENDIX

Chapter 4

Parameter	Value	Units
Density	5376.0	kg/m ³
Specific Heat	390	J/kg*K
Thermal Conductivity	50	w/m*K
Heat Transfer Coefficient	0.1	w/m ²
Emissivity	0.5	
Preheat Temperature	543	K
Plate Thickness	1	mm
Heat Input	480	watts
Beam Speed	0.6	m/s
Beam Radius	100	μm